Strategies to Enhance the Charge Dynamics of Bismuth Vanadate
For Photocatalytic Water Oxidation

by

Umesh Prasad

A Dissertation Presented in Partial Fulfillment
of the Requirements for the Degree
Doctor of Philosophy

Approved September 2021 by the
Graduate Supervisory Committee:

Arunachala Mada Kannan, Chair
Bruno Azeredo
Candace Chan
Sergio Garcia Segura

ARIZONA STATE UNIVERSITY

December 2021

ABSTRACT

Hydrogen is considered one of the most potential fuels due to its highest gravimetric energy density with no pollutant emission during the energy cycle. Among several techniques for hydrogen generation, the promising photoelectrochemical water oxidation is considered a long-term solar pathway by splitting water. The system contains a photoanode and a cathode immersed in an aqueous electrolyte where charge separation takes place in the bulk of the semiconducting material on light absorption, leading to water oxidation/reduction at the surface of the photoelectrodes/cathode.

It is imperative to develop materials that demonstrate high light absorption in the wide spectrum along with photoelectrochemical stability. N-type Monoclinic scheelite bismuth vanadate ($BiVO_4$) is selected due to its incredible light absorption capabilities, direct bandgap ($E_g \sim 2.4$-2.5 eV) and relatively better photoelectrochemical stability. However, $BiVO_4$ encounters huge electron-hole recombination due to smaller diffusion lengths and positive conduction bands that cause slow charge dynamics and sluggish water oxidation kinetics.

In order to improve the illustrated drawbacks, four strategies were discussed. Chapter 1 describe the fundamental understanding of photoelectrochemical cell and $BiVO_4$. Chapter 2 illustrates details of the experimental procedure and state-of-the-art material characterization. Chapter 3 provide the impact of alkali metal placement in the crystal structure of $BiVO_4$ systematically that exhibited ~20 times more performance than intrinsic $BiVO_4$, almost complete bulk charge separation and enhancement in the diffusion length. Detailed characterization determined that the alkali metal getting placed

in the interstitial void of $BiVO_4$ lattice and multiple interbands formation enhanced the charge dynamics.

Chapter 4 contains stoichiometric doping of Y^{3+} or Er^{3+} or Yb^{3+} at the Bi^{3+} site, leading to an extended absorption region, whereas non-stoichiometric W^{6+} doping at the V^{5+} site minimizes defects and increased charge carriers. To further enhance the performance, type-II heterojunction with WO_3 along *p-n* junction with Fe:NiO enhance light absorption and charge dynamics close to the theoretical performance.

Chapter 5 provides a comprehensive study of a uniquely developed sulfur modified Bi_2O_3 interface layer to facilitate charge dynamics and carrier lifetime improvement by effectively passivating the $WO_3/BiVO_4$ heterojunction interface. Finally, chapter 6 summarized the major findings, conclusion and outlook in developing $BiVO_4$ as an efficient photoanode material.

This dissertation is dedicated to my father, Shivpujan Seth, mother, Malti Devi, who always taught me to work hard and be honest towards my dream. In addition, my sister, Urmila Devi and brother, Ramesh Prasad, provided immense support, encouragement and always motivated me to pursue my dreams.

ACKNOWLEDGMENTS

I am so grateful to my PhD advisor, Prof. A. M. Kannan, for giving me an opportunity to start my research career in the material science semiconductor field in his lab. His consistent support in the design of experiments and feedback on obtained results helped me in improving my experimental and interpretation skills. Furthermore, he was always patient with me and encouraged to work hard. I thoroughly enjoyed publishing multiple papers with him.

Also, I am so grateful to Dr Jyoti Prakash as he introduced me to the real world of research, where I learned how to create a story from obtained data. He trained me on the tool, research layout and concepts generation. His dedication to publishing papers motivated me to approach every experiment as a potential research paper material. He has treated me like his younger brother. His patience, loving nature and pleasant personality made a highly productive environment that I will always cherish.

I am so grateful to Dr James Young for giving me an opportunity to conduct part of my research at the National Renewable Energy Laboratory (NREL). He always found time in his busy schedule and patiently trained me on all photoelectrochemical cell tools in his lab. He motivated and taught me to interpret research data to understand the in-depth meaning and connect it to the bigger picture. My thinking ability and approach improved when I started working with him and became a much better researcher. I am also grateful and happy to work with Dr Justin Johnson at NREL. Under his guidance, I was able to conduct transient absorption experiments and data interpretation. In addition, he patiently revised my writeup and gave his valuable feedback that helped me to get an in-depth understanding of the subject.

I would also like to thank Dr Bruno Azeredo for being part of the weekly meeting and giving his perspective and interpretation, which helped me understand the concepts. I am so thankful to Dr Xihong Peng for helping me with the density functional theory (DFT) calculations and clarifying my queries. Furthermore, I want to thank my Graduate Advising Committee, Dr Candace Chan and Dr Sergio Garcia Segura, for being on the committee. Their valuable time and valuable comments helped me in completing the degree. Also, I would like to thank the academic advisors, Amy Riggs and Meghan Vaughn, for providing necessary information and helpful advice in completing the PhD degree.

I would like to thank my lab members Xuan Shi, Pavan Badami, Grigoria Athanasaki and Nitin Chauhan for their assistance with experimental processes. I would like to express my gratitude to my collaborators Steven Johnston, Deborah McGott, Elisa M Miller, Hengfei Gu, Eric Garfunkel, Santosh K Gupta, Jose Zuniga, Yuanbing Mao and Sandeep K. Sharma for collaborating with me for advance analytical capabilities and experimental facilities.

Also, I would like to thank my classmates and friends Mohan Radhesh Mallya, Weiheng Xu, Anamika Banerjee, Stanislau Niauzorau, Aliaksandr Sharstniou, Natalya Kublik and Amm Hasib for the support and insightful conversations.

Finally, I would like to acknowledge the Salt River Project, Tempe, Arizona State University, Indo-US 21st Century Knowledge Initiative Project. Also, I would like to acknowledge the National Renewable Energy Laboratory (NREL), operated by Alliance for Sustainable Energy, LLC, for the U.S. Department of Energy research support from the HydroGEN Advanced Water Splitting Materials Consortium and Solar Photochemistry Program of the U.S. Department of Energy, Office of Basic Energy Sciences, Division of Chemical Sciences, Biosciences and Geosciences for transient absorption experiments.

TABLE OF CONTENTS

Page

CHAPTER

LIST OF TABLES

Table Page

LIST OF FIGURES

Figure Page

Figure Page

Figure Page

Figure Page

LIST OF PUBLICATIONS

PUBLICATIONS

- Prasad, U.; Young, J. L.; Johnson, J. C.; McGott, D. L.; Gu, H.; Garfunkel, E.; Kannan, A. M. Enhancing Interfacial Charge Transfer in a $WO_3/BiVO_4$ photoanode Heterojunction through Gallium and Tungsten Co-Doping and a Sulfur Modified Bi_2O_3 interfacial Layer. *J. Mater. Chem. A* **2021**, *9*, 16137–16149.

- Prasad, U.; Prakash, J.; Shi, X.; K. Sharma, S.; Peng, X.; M. Kannan, A. Role of Alkali Metal in $BiVO_4$ Crystal Structure for Enhancing Charge Separation and Diffusion Length for Photoelectrochemical Water Splitting. *ACS Appl. Mater. Interfaces* **2020**, 12, 52808–55281.

- Prasad, U.; Prakash, J.; Kannan, A. M. Effects of Yttrium, Ytterbium with Tungsten Co-Doping on the Light Absorption and Charge Transport Properties of Bismuth Vanadate Photoanodes to Achieve Superior Photoelectrochemical Water Splitting. *Sustain. Energy Fuels* **2020**, *4*, 1496–1506.

- Prakash, J.; Prasad, U.; Shi, X.; Peng, X.; Azeredo, B.; Kannan, A. M. Photoelectrochemical Water Splitting Using Lithium Doped Bismuth Vanadate Photoanode with Near-Complete Bulk Charge Separation. *J. Power Sources* **2020**, *448*, 227418.

- Kanth, N.; Xu, W.; Prasad, U.; Ravichandran, D.; Kannan, A. M.; Song, K. Pmma-Tio2 Fibers for the Photocatalytic Degradation of Water Pollutants. *Nanomaterials* **2020**, *10*, 1–8.

- Prakash, J.; Prasad, U.; Alexander, R.; Bahadur, J.; Dasgupta, K.; Kannan, A. N. M. Photoelectrochemical Solar Water Splitting: The Role of the Carbon Nanomaterials in Bismuth Vanadate Composite Photoanodes toward Efficient Charge Separation and Transport. *Langmuir* **2019**, *35*, 14492–14504.
- Prasad, U.; Prakash, J.; K. Gupta, S.; Zuniga, J.; Mao, Y.; Azeredo, B.; Nadar Mada Kannan, A. Enhanced Photoelectrochemical Water Splitting with Er- and W-Codoped Bismuth Vanadate with WO_3 Heterojunction-Based Two-Dimensional Photoelectrode. *ACS Appl. Mater. Interfaces* **2019**, *11*, 19029–19039.
- Prasad, U.; Prakash, J.; Azeredo, B.; Kannan, A. Stoichiometric and Non-Stoichiometric Tungsten Doping Effect in Bismuth Vanadate Based Photoactive Material for Photoelectrochemical Water Splitting. *Electrochim. Acta* **2019**, *299*, 262–272.

BOOK CHAPTER

- Prasad, U. $BiVO_4$-Based Photoanodes for Photoelectrochemical Water Splitting. *ACS Symp. Ser.* **2020**, *1364*, 137–167.

PATENTS

- N. Kanth, W. Xu, U. Prasad, D. Ravichandran, A. M. Kannan, K. Song "Polymethyl methacrylate (PMMA)-TiO_2 composite fibers for photocatalytic degradation of water pollutants" *US Patent App.:* 63/184,419, **2021**
- U. Prasad, J. Prakash, A. M. Kannan, "Alkali metal doped bismuth vanadate photoanode for hydrogen production by photoelectrochemical water splitting" *US Patent App.* 16/869,887, **2020**

CHAPTER 1 INTRODUCTION

1.1 Background

The rise in the economy and population led to a rapid increase in the total energy demand globally. In the current scenario, most of the energy supplies (>80%) come from non-renewable energy sources[1,2]. However, the energy and environmental issues associated with non-renewable energy remain a significant challenge. Among the sustainable energy sources, solar energy is inexhaustible, with the highest potential and a ubiquitous energy resource[3,4]. It can generate up to 30 TW of power only by using 0.8% of the land surface on earth with 10% efficient solar cell[5]. The drawback of this energy is intermittency due to the day/night cycle, presence of clouds, and change in weather[1,5]. The proposed solution is to store solar energy for such intermittency, but it is exhaustible to store such vast energy. A possible system is grid-based energy storage in the form of a smart grid, however, at some point, the capacity of the grid system will be exceeded[6], and alternative large-scale energy storage solutions need to be implemented.

There is no doubt that the sun is a major source of renewable energy, but a certain issue is an intermittency. The sun energy mostly depends on the day/night cycle, cloud and geographical location. Also, solar energy is relatively hard to extract in the form of fuel compared to fossil fuels, making it economically challenging to capture. In order to deal with such intermittency and complicacy, electricity network operators might implement grid-based energy storage in the form of a smart grid. However, grid-based storage capacities may be exceeded, and more efficient large-scale energy storage solutions must be implemented. Another alternative possibility is to store solar energy in the form of chemical fuel. From Figure 1, many storage devices such as mechanical (compressed air, pump water uphill), fuels (coal, wood, gasoline, diesel, methanol, natural gases and hydrogen), capacitors (supercapacitors and ultracapacitors) and batteries (Li-ion, Ni-Cd and Pd-acid) provide an effective way of energy storage[7]. However, among the suggested storage devices, battery, capacitors and fuel provide the most effective way of storing the energy with 2-3 orders of magnitude higher energy density because the energy is stored in the form of the smallest possible configuration: chemical bonds. This suggests that storing energy in the form of chemical fuels is one of the best possible ways. As depicted from the table, chemical fuels such as methanol, methane, diesel, and gasoline need a source of carbon in their synthesis, which is concerned with the environmental concern as discussed earlier.

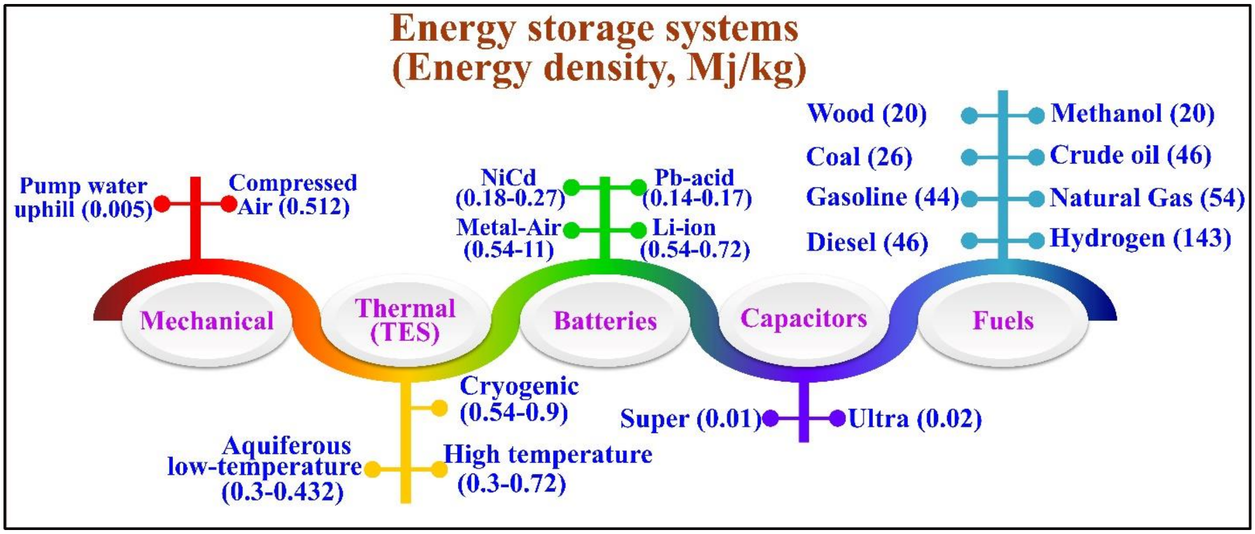

Figure 1 Various mechanical, thermal, batteries, capacitor and fuels energy storage systems.

A highly desirable approach is to store solar energy in the form of chemical fuels (hydrogen, methane, methanol, gasoline, and diesel), which has energy storage density (2-

3 order of magnitude) compared to mechanical systems and batteries[8]. Among the chemical fuels, hydrogen is without the source of carbon[9]. Converting solar energy into hydrogen is considered a highly desirable approach. Hydrogen production via water splitting is one of the most promising ways, and it is known as the "holy grail", convert solar energy directly into green storable chemical energy[10]. In contrast, there are many possible pathways for converting water and sunlight into hydrogen. Photoelectrochemical (PEC) water splitting is one of the most promising in complex routes because of the ease of collecting generated gasses at the convenient pressure-temperature operating window. The department of energy has projected PEC as a long-term goal for hydrogen generation through water splitting, as shown in Figure 2. The technology for indirect PEC water splitting using coupled photovoltaic (PV) and electrolyze systems is already commercially available, showing a solar-to-hydrogen (STH) efficiency of around 8%. However, direct PEC water splitting—this process will be discussed in the next section—offers three important advantages. First, a much lower overpotential is needed due to the 50-100 times lower operating current density of the direct PEC water splitting that relaxes the condition of the catalytic step in the process. Second, in order to achieve the potential needed for the electrolyzer (~1.9V), three (or more) PV cells are normally used in series. As a result, a larger area is needed to achieve the same current density, which is not the case for direct PEC water splitting. Finally, a direct PEC water splitting system requires fewer additional components (wires, frames, glass, etc.) than a combination of PV plus electrolysis since one can construct a monolithic device that may lead to a significantly lower balance-of-system cost for producing hydrogen. Coupled PV-electrolyzer is estimated to produce hydrogen at the cost exceeding US$ 8/kg, while a reasonable estimate of the direct PEC

water splitting shows a cost in the range of US$ 3-5/kg, compares very well with the US$ 2-4/kg target that is set by the US Department of Energy (DOE), and the EU‘s 5 €/kg H_2 target for future hydrogen production pathways.

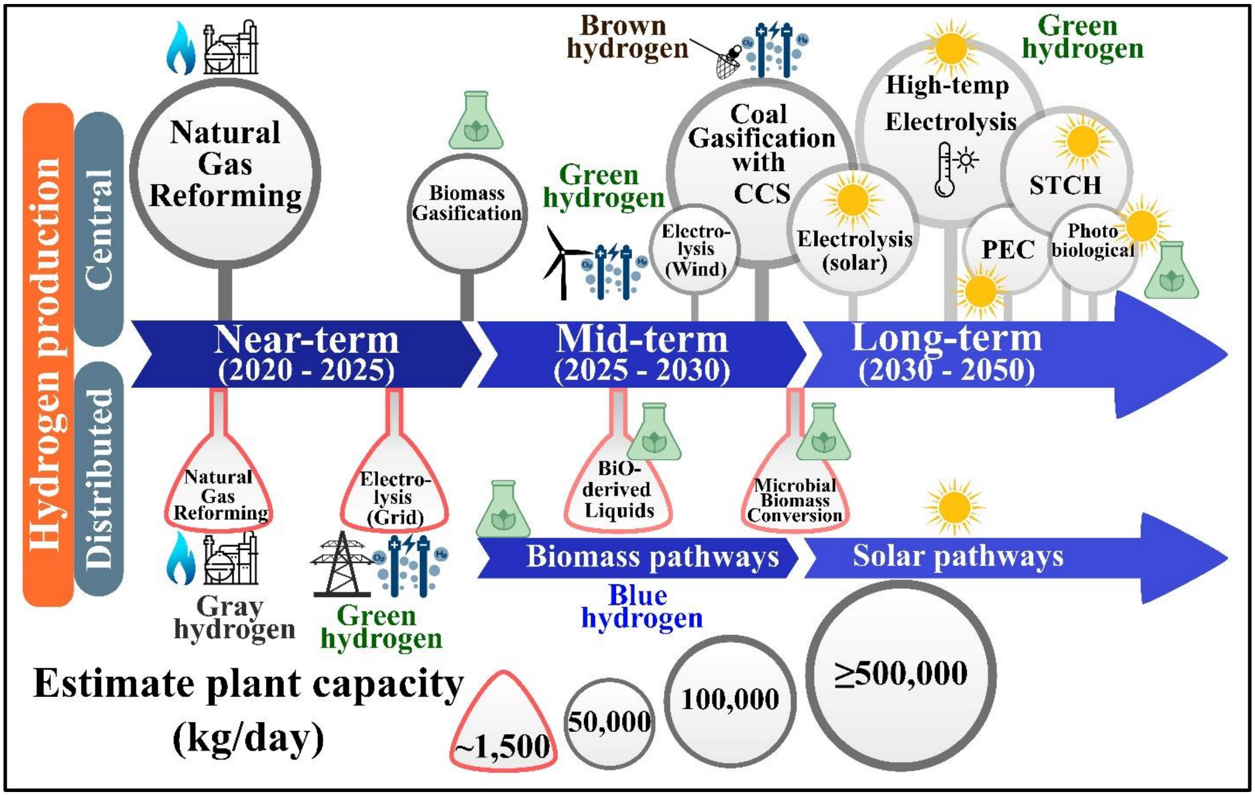

Figure 2 Time frame and production scale of hydrogen generation pathways with near, mid and long-term as per department of energy

1.2 The Photoelectrochemical Water Splitting

The photoelectrochemical (PEC) water splitting is the most promising long term approach for hydrogen generation, which involves capturing ambient sunlight and converting the electromagnetic energy directly into chemical energy in the form of chemical bonds[11,12].

PEC cell contains a semiconducting photoanode and photocathode immersed in an aqueous electrolyte, charge separation take place in the bulk of the semiconducting material on light absorption that leads to water oxidation/reduction at the surface of the photoelectrodes. The system is attractive and has multiple advantages as it can be carried out at room temperature, much lower overpotential required, no need for large-scale solar concentration, and the device can be constructed entirely by using inorganic materials. However, water oxidation is challenging despite being the most abundant electron donor because it involves four-electrons and four-protons processes that need significant overpotential due to high electrons and holes recombination and kinetic barriers[13,14].

1.3 Fundamentals of Photoelectrochemical Solar Water Splitting

The simplified diagram for the PEC water splitting is given in Figure 3a. The prime components of the PEC cell are semiconductor, which works as a photoanode, aqueous electrolyte, membrane and metal as a counter electrode. When light photons, with higher energies than bandgap (E_g) of the semiconductor, incident on the surface of photoanode, electron and hole pairs generate in the bulk of the semiconducting material (eq 1) and get separated due to the presence of electric field inside the semiconductor after applying small external bias through the power supply unit (PSU)[15,16]. The electrons excite from occupied VB to unoccupied CB band, are swept away towards the charge collector, and transported to the metal counter electrode for water reduction to form hydrogen gas (HER) (eq 2)[4]. On the other hand, photogenerated holes in the VB swept towards the photoanode surface/electrolyte interface for water oxidation to form oxygen gas (OER) (eq 3)[11]. The OER reaction is essential for achieving high water splitting as it generates protons (H^+) and electrons for the water-splitting process. The photoanode and counter electrode are separated by a thin membrane, which avoids mixing evolving hydrogen and oxygen gases at the respective electrodes.

$$\text{Semicondutor} + \text{photons}\left(\text{hv} \geq E_g\right) \rightarrow\ e^-{}_{CB} + h^+{}_{VB} \qquad (1)$$

$$\text{HER: } 2\text{H}^+ + 2e^-{}_{CB} \rightarrow H_2\ (gas) \qquad \Delta E =\ -0.41\ V \qquad (2)$$

$$OER\text{: } 2H_2O + 4\ h^+{}_{VB} \rightarrow O_2(gas) + 4H^+ \qquad \Delta E =\ +0.82\ V \qquad (3)$$

$Overall$:

$$2H_2O \rightarrow 2H_2(gas) + O_2(gas) \qquad \Delta E =\ 1.23\ V,\ \ \Delta G =\ +238\ kJ.mol^{-1} \qquad (4)$$

Thermodynamically, the eq 4 is an uphill reaction because of a higher positive change in Gibbs free energy (ΔG +238 kJ mol^{-1}). Furthermore, it can be observed from eqn 2 and 3 that the bottom of the CB edge must be located lower than the reduction potential (H^+/H_2) -0.41 eV and the top of the VB edge must be exceeded the oxidation potential (H_2O/O_2) 0.82 eV for efficient overall water splitting[17]. Therefore, the required bandgap energy (E_g) of a semiconducting material should be at least 1.23 eV to split water into H_2 and O_2. Additionally, kinetic overpotentials are required to drive the HER and OER reactions due to the energy losses. Thus, the required E_g of semiconducting material should be from 1.5 to 2.5 eV per electron-hole pair generation to account for these loses[14].

The CB edge of the semiconducting materials varies with pH in the linear relationship as per the Nernstian relation, as given in eq 5[18,19]. At room temperature and atmospheric pressure, the change in CB edge is 59 mV per pH unit.

$$E_{CB} = E_{CB}^{0}(pH = 0) - 0.059\,pH \tag{5}$$

The redox potential of water also changes as per the Nernstian equation with a change of 59 mV per pH, which makes no change in the overpotential of photogenerated electron-hole pairs for water redox potential at different pH[20,21].

The interface mechanism started on the relative positions of fermi levels when a semiconductor and redox electrolyte were brought into contact. Figure 3b shows a PEC cell before the equilibrium process where an n-type semiconductor is ohmically connected with the metal counter electrode and both electrodes are immersed in the electrolyte. After establishing contact between semiconductor and counter electrode, a net flow of charge starts flowing through the interfaces until the chemical potential of electrons reaches equilibrium with the semiconductor, redox electrolyte and metal counter electrode[22]. The chemical potential of electrons is determined by the fermi level of semiconductor (E_F), whereas the redox potential of electrolyte (E_{redox}) is determined by the redox couples present in the electrolyte[23]. When the Fermi level of an n-type semiconductor lies higher, the redox potential of electrolyte, electrons start flowing from semiconductor to electrolyte via a counter electrode, as shown in Figure 3c. This flow of electrons leads to forming a depletion layer or space charge layer (W_{SC}) towards the semiconductor at the semiconductor surface/electrolyte interface[24] (shown in Figure 3c). Another layer generated in the electrolyte is similar to the space charge layer but opposite in the Helmholtz layer (HL) sign. This layer is composed of absorbed ions from electrolytes, extend in the length of a few angstrom[22], as indicated in Figure 3c. The positive ions (holes) build a positive space charge layer, and an internal electric field causes the bend in the CB and VB edges of the semiconductor.

Similarly, in the case of a p-type semiconductor, where the Fermi level lies below the redox potential of electrolyte, holes start flowing into electrolyte via the counter electrode and remaining electrons in the semiconductor build a negative space charge layer, and the internal electric field causes the bends down in the CB and VB edges of the semiconductor. The band bending, V_B, acts like a potential barrier against electrons flow (n-type semiconductor) or holes transfer (p-type semiconductor), known as Schottky-Barrier. As the majority of charge carriers depleted due to Schottky Barriers, the space charge layer grows to angstroms to microns range. Thus, total band bending is the difference between fermi levels of semiconductor and redox potential of electrolyte[25].

However, Schottky Barriers generated due to the band bending can be flattened after applying an external bias (E_{ext}), known as flat-band (U_{fb}) potential, which defines the thermodynamic ability of a semiconductor to oxidize/reduce water under illumination. Correspondingly, It determines the fermi levels position, charge carrier density, position of VB and CB edges of semiconductor with respect to reference electrode before equilibrium[23]. On the other hand, the net flow of charge occurs at the metal electrode/electrolyte interface to equilibrate the fermi level of metal with electrolyte (E_{redox}) that led to minimizing W_{SC} due to the high concentration of free electrons in the metal[5]. Therefore, the barrier height determined by the energy difference between E_{redox} and the bottom of the CB edge at the equilibrium condition in the semiconductor defines the maximum possible energy of the photogenerated electron-hole pairs in the semiconductor[25].

Under light illumination, photons with higher energy than the bandgap of a semiconductor get absorbed, generating electron-hole pairs as schematically represented in Figure 3d. The photogenerated electron-hole pairs get physically separated by internal electric field[5], where electrons travel to the counter electrode via an external circuit to drive the reduction reaction and holes travel to the surface of the semiconductor and inject into the electrolyte to perform the oxidation reaction. As a result, a photovoltage (V_{ph}) generates between the semiconductor and metal counter electrode, equivalent to the difference between the semiconductor and the redox potential of electrolyte[23]. The photovoltage raised the fermi level of semiconductor E_F by V_{ph}[22]. The maximum possible Fermi level is equivalent to the U_{fb}, and split into two quasi-fermi levels, $E_{F,n}$ and $E_{F,p}$ on light illumination for electrons and holes respectively[5] represented in Figure 3d.

As illustrated in Figure 3e, the oxidation and reduction process required an external bias potential ϕ_{ox} and $\phi_{Red,}$ respectively. Even though the illumination intensity is enough to flatten the bands, the hydrogen reduction reaction is not possible as the Fermi level is below the hydrogen reduction potential[25]. The external bias (E_{ext}) raised the fermi level and provided overvoltage to the counter electrode[16], as shown in Figure 3e. If the external bias is more negative for n-type semiconductors from equilibrium value, the band bending decreases and electrons start moving from CB to electrolyte via external contact[21]. In addition, the external bias raises the band bending for effective electron-hole pairs separation[25]. However, with a more positive bias, the Schottky Barrier becomes bigger, limiting the flow of electrons. Therefore the junction behaves similarly to Schottky Diode, blocking the flow of current in one direction[18,23].

The most critical parameters in the PEC cell are the light absorption, charge carriers transfer through the semiconductor (bulk) and across the semiconductor surface/electrolyte interface and the stability of the material[26]. The photogeneration of electron-hole pairs and transport through the films are considered as a function of the bulk properties[27]. On the other hand, phenomena such as charge transfer to reactant surface and material stability are surface properties[27]. The oxidation and reduction reactions occur in the electrodes providing a net change in the electrolyte composition in such a manner that solar energy is directly stored in the form of chemical bonds[26]

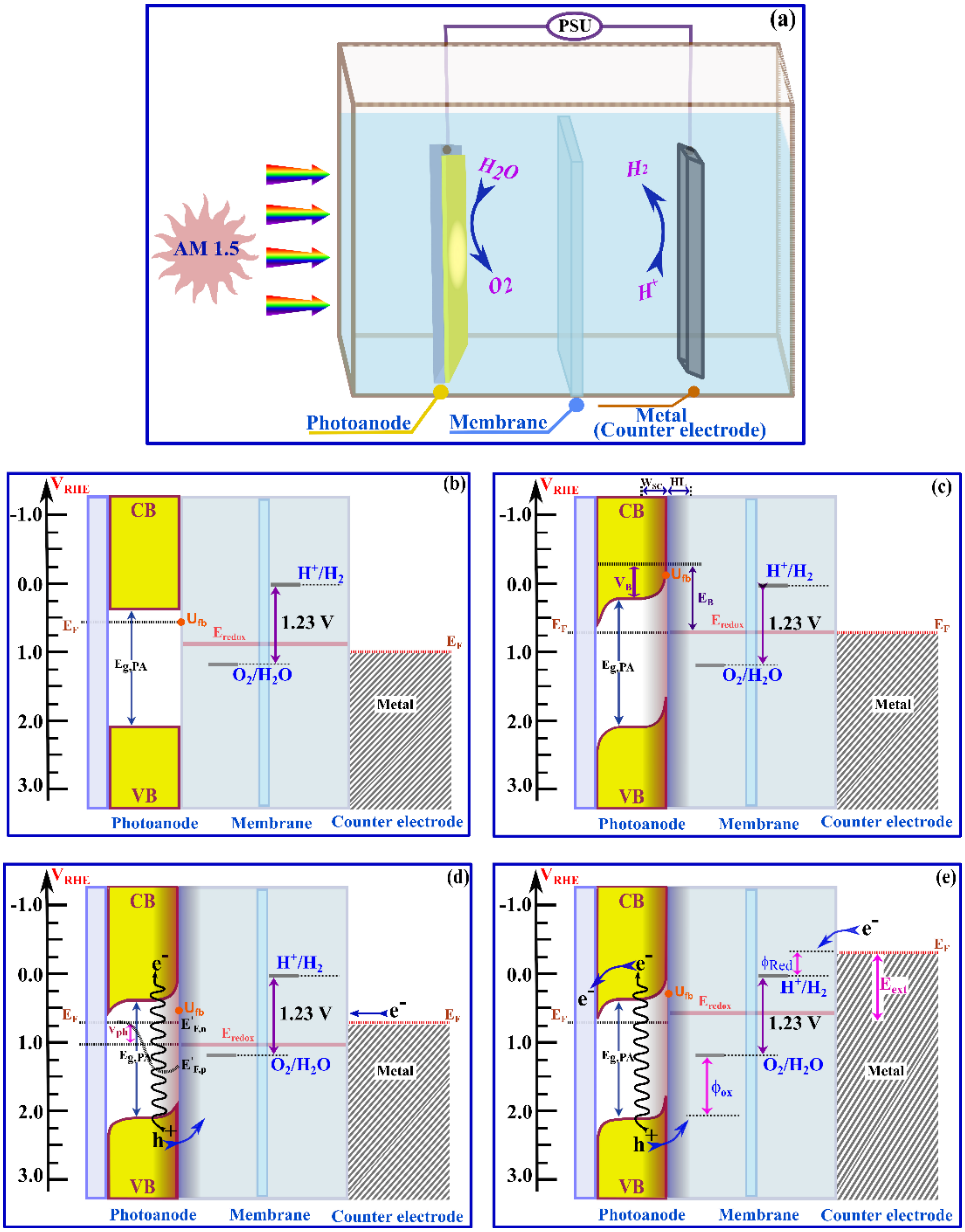

Figure 3 (a) Photoelectrochemical cell water splitting system containing photoanode, counter electrode and membrane as a separator. Energy level diagram at the solid and liquid interface when semiconductor and counter electrode placed in the electrolyte (b) no contact or before equilibrium, (c) in contact and after equilibrium, (d) after light illumination and (e) after applying external bias.

1.4 Materials for photoelectrochemical cell

It is imperative to develop materials that demonstrate high overall water splitting efficiencies. Semiconducting materials should meet requirements such as a sufficient photovoltage[28], an appropriate band alignment where the top of valence band (VB) edge must be positive enough to drive water oxidation[24], and the bottom of the conduction band (CB) must be more negative than the reduction potential of hydrogen for water reduction[24]. In addition, the material should have better light-harvesting capabilities in the visible range[29], efficient charge separation and transport from the bulk of the thin film to the surface and from the surface to electrolyte solution[30]. Additionally, the material should be thermodynamically favorable, have sufficient surface area to provide enough active sites, excellent corrosive resistance, and cost-effectiveness[31].

Many recent efforts have been made to develop efficient photoelectrodes materials such as TiO_2[32], WO_3[33], Fe_2O_3[34], ZnO[35], $BiVO_4$[36], Cu_2O[37], $CuWO_4$[38], $CaFe_2O_4$[39], $ZnFe_2O_4$[40], $CuBi_2O_4$[41], $CuNbO_4$[42], $CuFeO_2$[43], $CuInS_2$[44], TaON[45], Ta_3N_5[46], $BaTaO_2N$[47], $BaNbO_2N$[48], p-CdTe[49], n-CdTe[49], InP[50], GaAs[51], InGaN[52], p-GaP[53], n-GaP[53], SiC[54], p-Si[55], and n-Si[55]. Some potential materials and theoretical photocurrent and solar to hydrogen efficiencies with bandgap and wavelength onset were shown in Figure 4. However, it is still a challenge to find material that can be utilized for practical application. Potential photoanode material such as TiO_2 was explored extensively. However, TiO_2 suffers from a wide bandgap, making it challenging to use for water splitting application[32]. Apart from TiO_2, materials such as Fe_2O_3[34], Cu_2O[37], WO_3[33], and TaON[45] were explored to harvest more sunlight. Even after having an appropriate bandgap, achieving remarkable overall water splitting efficiency is still a challenge. Therefore, the work on finding efficient photoelectrode materials is in progress[31].

Figure 4 further illustrates that material with a smaller bandgap can absorb the sunlight in the wider spectrum range to achieve high solar-to-hydrogen (STH) efficiency and photocurrent density (PCD). Theoretical STH and solar photocurrent of a photoelectrode under simulated AM 1.5G illumination (100 mW.cm^{-2}). It is based on an idealized case where 100% of the photons in the solar spectrum with energies exceeding the bandgap are absorbed and converted, shows the band gap of the semiconductor determines that It is still a challenge to achieve remarkable overall water splitting efficiency. Therefore, the work on finding efficient photoelectrode materials is in progress[31].

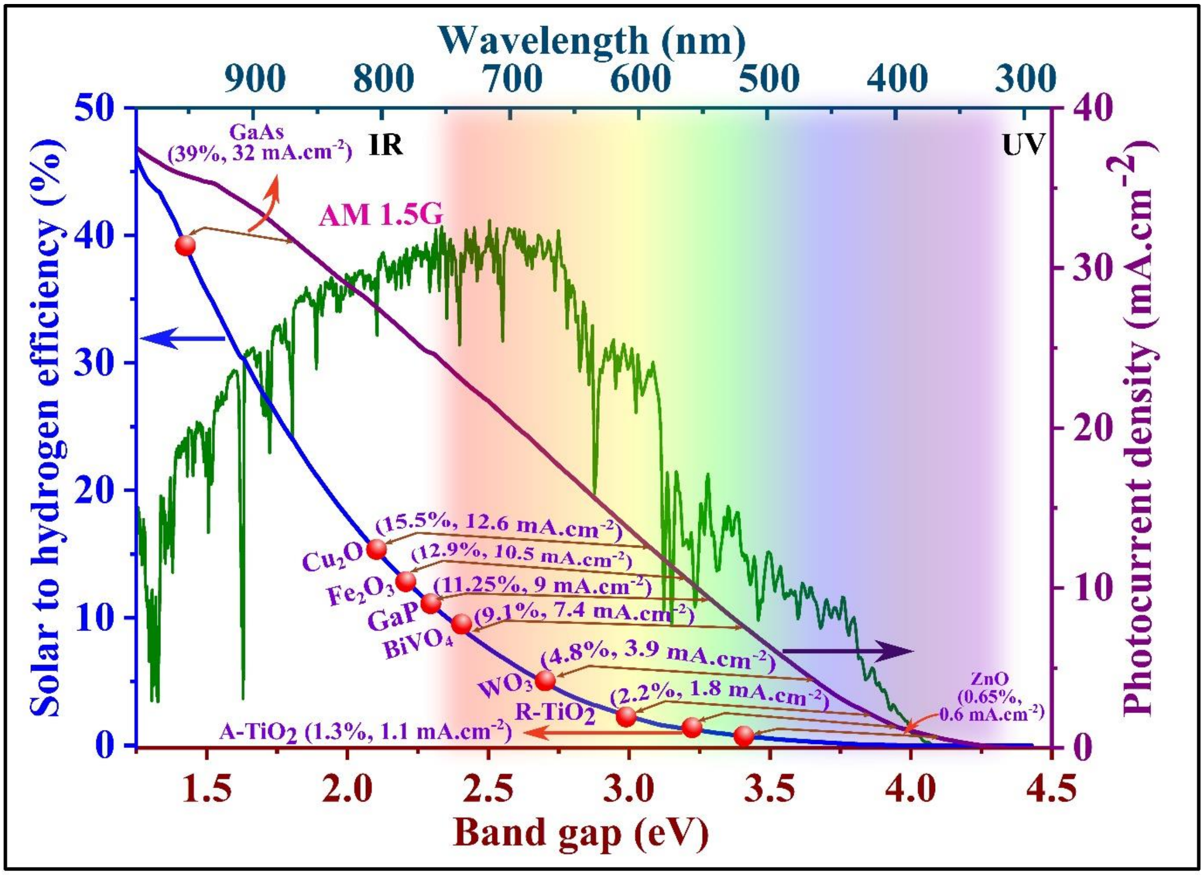

Figure 4 Solar energy-driven water splitting under simulated AM 1.5G illumination using a light absorber spectrum of AM 1.5G (i.e. 1 sun condition, power density of 100 mWcm^{-2}).

1.5 $BiVO_4$: a potential material oxide semiconductor

Monoclinic scheelite n-type bismuth vanadate ($BiVO_4$) has garnered tremendous scientific interest as a potential photocatalyst since the study of its property by Kudo *et al.*[56] in 1998. $BiVO_4$ has incredible capabilities such as absorb light in the broad solar spectrum $\lambda \geq 520$ due to lower bandgap energy (Eg ~ 2.4-2.5 eV)[57], defect-tolerant nature[58], and appropriate VB alignment[59]. Apart from that, $BiVO_4$ does not need a specific medium (acidic or basic) to obtain a high current[60]. However, being a suitable photoanode material, $BiVO_4$ possesses many drawbacks such as substantial electron-hole recombination due to self-trapping and small diffusion length[61], poor charge transport properties, sluggish water oxidation kinetics and the position of CB edge is below water reduction potential, which provides an unfavorable condition for the water splitting[62]. Several strategies have been implemented to improve the water oxidation kinetics of $BiVO_4$. Such as doping[61,63,64], forming heterostructure system[33], nanostructuring[65], coupling with carbonaceous materials to increase the charge carrier separation and transport[57]. Additionally, implementing an electron transfer layer and surface overlayer formation or hole transfer layer for effective charge tranfer[61,66].

1.6 Crystal and electronic structure of $BiVO_4$

This section discusses various crystal structures and the electronic structure of $BiVO_4$ related to photoelectrochemical properties.

The natural structure of $BiVO_4$ as a mineral is pucherite with the orthorhombic crystal structure (space group: *Pnca* with a= 5.332, b = 5.06 and c = 12.02 Å)[67]. However, $BiVO_4$ does not form a pucherite structure after synthesization in the laboratory[68]. Instead, it forms a scheelite or a zircon-type structure[69]. The scheelite structure have tetragonal crystal system (space group: $I4_1/a$ with a = b = 5.1470, c = 11.7216 Å)[70] or a monoclinic crystal system (space group: I2/b with a =5.1935, b = 5.0898, c = 11.6972 Å, and β= 90.3871°)[70] whereas zircon-type structure consists tetragonal crystal system (space group: $I4_1$/and with a = b = 7.303 and c = 6.584 Å)[1].

In the $BiVO_4$ scheelite structure, each Bi atom is coordinated by eight oxygen atoms from different VO_4 tetrahedral units and each V atom is coordinated by four oxygen atoms at the tetrahedral site[70], as shown in Figure 5a and b, where Bi and V centers are coordinated along the [001] direction. Each oxygen atom is coordinated by two Bi and one V centers, forming a three-dimensional structure by holding Bi and V centers together. However, monoclinic scheelite structure shows differences such as more distortion in the local environment of Bi and V ions, two different V–O bond lengths (1.69 and 1.76 Å) and four different Bi-O bond lengths (2.35, 2.37, 2.52 and 2.63 Å) that lead to loss of four-fold symmetry[70]. Whereas for tetragonal scheelite structure, all four V-O bond lengths are equal to (1.73 Å) and two different bond lengths, Bi-O (2.4 and 2.47 Å), exist[70]. The structure of scheelite tetragonal and monoclinic and tetragonal zircon-type are shown in Figures 5a and b. The observed significant distortion in the monoclinic scheelite structure enhances the local polarization that leads to better electrons and holes separation and superior photocatalytic activity compared to tetragonal scheelite structure[71]. The local environment of Bi and V centers for zircon type structure is shown in Figure 5c, where eight oxygen atoms coordinate Bi by six different VO_4 tetrahedral units because two VO_4 tetrahedral units provide two oxygen atoms to Bi atom. Each V atom is coordinated by four oxygen atoms[1,72].

The zircon type structure was synthesized at low temperature (precipitation at room temperature)[1]. On the other hand, zircon type structure to monoclinic scheelite structure was obtained at a high-temperature 400-550°C[1]. The tetragonal scheelite structure was obtained at an even higher temperature than monoclinic scheelite temperature. The transition between tetragonal and monoclinic scheelite happens reversibly at 255°C[1].

The photocatalytic activity of $BiVO_4$ highly depends on the crystal structure. For example, the scheelite $BiVO_4$ shows better photocatalytic activity over zircon type $BiVO_4$[73] because of higher photons absorption, with a lower bandgap for scheelite (2.4 eV) compared to that of the zircon-type (2.9 eV)[72]. Kudo *et al*[73] proposed the schematic band diagram for scheelite and zircon-type $BiVO_4$, as shown in Figures 5d and e. In the scheelite type $BiVO_4$, the charge transition occurs between Bi 6s or hybrid Bi 6s-O 2p orbitals to empty V 3d orbitals[1], but, in zircon type $BiVO_4$, charge transition occurs from O 2p and V 3d orbitals[72]. Thus, the reduction in the bandgap of scheelite type $BiVO_4$ is due to the appearance of Bi 6s above O 2p[1,72].

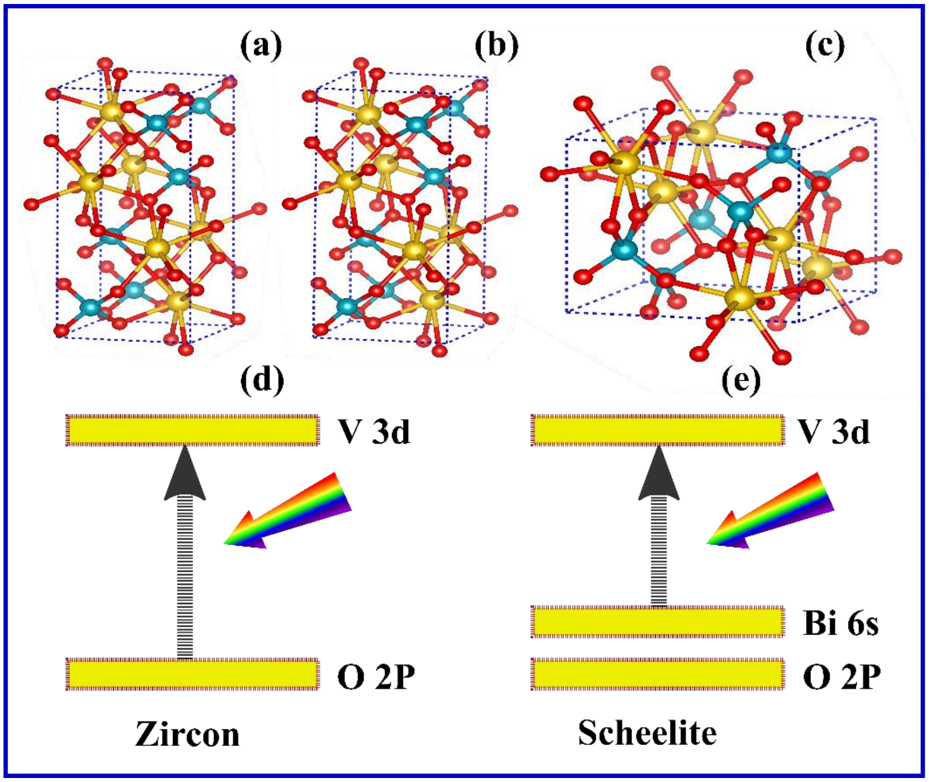

Figure 5 Crystal structure of scheelite, (a) tetragonal, and (b) monoclinic type $BiVO_4$. Crystal structure of (c)Tetragonal zircon type $BiVO_4$. (cyan: Bi, yellow: V and red: oxygen). (d) Band diagram of zircon, and (e)scheelite type $BiVO_4$.

1.7 Strategies to enhance the charge dynamics of $BiVO_4$

Monoclinic scheelite n-type bismuth vanadate ($BiVO_4$) has garnered tremendous scientific interest as a potential photocatalyst since the study of its property by Kudo *et al.*[56] in 1998. $BiVO_4$ has incredible capabilities such as absorb light in the broad solar spectrum $\lambda \geq 520$ due to lower bandgap energy (Eg ~ 2.4-2.5 eV)[57], defect-tolerant nature[58], and appropriate VB alignment[59]. Apart from that, $BiVO_4$ does not need a specific medium (acidic or basic) to obtain high current[60]. However, being a suitable photoanode material, $BiVO_4$ possesses many drawbacks such as substantial electron-hole recombination due to self-trapping and small diffusion length[61], poor charge transport properties, sluggish water oxidation kinetics, and the position of CB edge is below water reduction potential, which provides an unfavorable condition for the water splitting[62]. Therefore, several strategies have been implemented to improve the water oxidation kinetics of $BiVO_4$. Such as doping[61,63,64], forming heterostructure system[33], nanostructuring[65], coupling with carbonaceous materials to increase the charge carrier separation and transport[57]. Additionally, implementing an electron transfer layer and surface overlayer formation or hole transfer layer for effective charge tranfer[61,66].

Chapter 2 discussed the detail of experimental procedures that include thin film deposition/fabrication process, details of photoelectrochemical analysis and various state-of-the-art characterization details. Chapter 3 discuss the role of alkali metal (Li or Na or K) doping in the $BiVO_4$ lattice structure to improve the light absorption, electron-hole pairs bulk diffusion length, and surface charge transfer for photoelectrochemical water splitting was systematically investigated. Chapter 4 discusses a systematic investigation of doping/co-doping of Y^{3+}, Er^{3+}, Yb^{3+} in $BiVO_4$ and W^{6+} at Bi^{3+} and V^{5+} sites, respectively with respect to their light absorption, bulk and surface charge separation and transfer properties. The individual element doping with W was chosen in the current study because doping significantly enhances the charge transport property[81]. Individual elements Y, Er and Yb were chosen in the current study because of their extended light absorption, leading to high absorption efficiency[82,83]. Furthermore, type II heterojunction was formed with WO_3 and *p-n* junction with Fe:NiO for efficient charge separation and transport. The combined effect of hetero and *p-n* junction facilitated an inner built electric field in enhancing the surface reaction kinetics (transportation of electron-hole pairs), lowering the band bending conditions, and increasing the bulk charge separation.

Chapter 5 implemented a multifaceted approach for addressing the interfacial charge recombination in WO_3/$BiVO_4$ heterojunction where (i) $BiVO_4$ was co-doped and (ii) an interfacial layer was implemented to improve the effective charge separation and transfer. Initially, $BiVO_4$ was co-doped with Ga^{3+} and W^{6+} at the Bi^{3+} and V^{5+} sites, respectively, to enhance light absorption, the concentration of photogenerated charge carriers, and improve bulk charge separation. A uniquely prepared sulfur (S) modified Bi_2O_3 (S:Bi_2O_3) layer was implemented so that S diffused to adjacent underlayer (WO_3) and overlayer ((Ga,W):$BiVO_4$), which helped in increasing additional reactive sites for charge transport.

Finally, Chapter 6 summarizes all the research reported and recommends developing efficient $BiVO_4$ photoanodes for hydrogen generation water splitting.

CHAPTER 2 EXPERIMENTAL DETAIL AND CHARACTERIZATION PROCEDURES

2.1 Introduction

The design of experiments for all strategies was determined based on the conceptual modifications, required analysis and state-of-the-art characterizations to evaluate the compositional details, photoelectrochemical properties and charge dynamics behaviors. Figure 6 illustrates the various steps involved in completing a study. The initial stages contain the theoretical assessment to determine the appropriate modifications to enhance the charge dynamics of $BiVO_4$. These steps include research layout, process development and designing experiments to execute the concepts from theoretical assessments to device fabrication. In the subsequent step, synthesis of novel nanostructured materials and thin-film fabrication. Materials were synthesized using solve thermal process and hydrothermal method. Then, thin films were prepared using various methods such as ultrasonic spray coating, chemical vapor deposition (CVD), spin coating, electrodeposition technique, dip and drop-casting.

Further, the prepared thin films were analyzed to determine the compositional details and quantitative analysis on the molecular level using various advanced analysis techniques. Subsequently, the charged dynamic was evaluated using advanced optical characterization and state-of-the-art characterizations. Photoelectrochemical analyses were conducted to study photoanode surface and electrolyte interface. The study contains linear sweep voltammetry, stability, impedance spectroscopy, Mott-Schottky and stability measurements. In order to analysis data, the various software package was employed such as Origin Lab and JMP. Various scripting was written using MATLAB and Python. The complete processes were repeated and revised based on the result concluded from the data analysis. However, in most cases, various intermediate samples were fabricated to validate the concepts, including short annealing to evaluate the epitaxial crystal growth, composition evaluation, and charge dynamics properties evaluation. The process was repeated until reproducing the performance of samples. The troubleshooting and calibration of measurements are validated before every measurement. Also, multiple samples were prepared in order to determine the validity of the results.

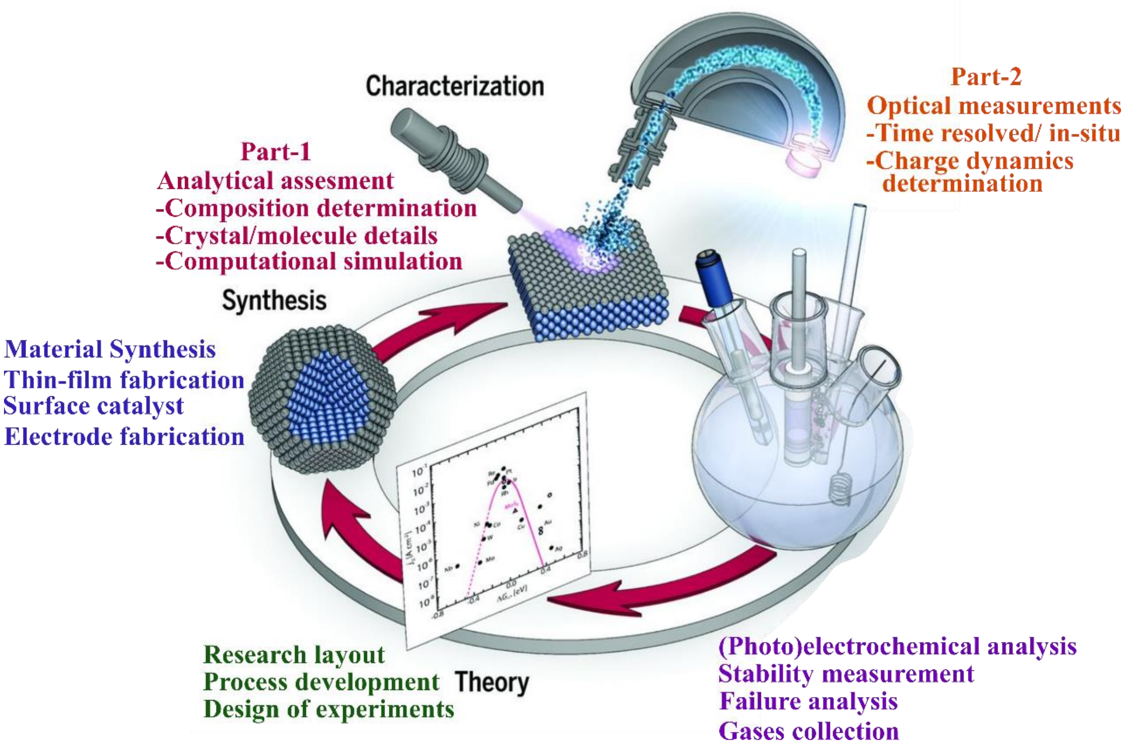

Figure 6 Experimental details and measurement procedure

2.2 Thin Film Fabrication

The precursor solution of $BiVO_4$ was prepared using 3mM $Bi(NO_3)_3{\cdot}5H_2O$ and 3 mM NH_4VO_3 in 2M HNO_3. The thin film deposition was carried out using various techniques such as spin coating, chemical vapor deposition, dip and drop-casting. Ultrasonic spray coating is one of the promising approaches for thin-film preparation, as shown in Figure 7. This system provides the flexibility of composition tunning, porosity control with an appropriate thermal cycle process, and an easy-to-build stack base structure. However, this system contains various complicated parts and is sensitive to the type and nature of the precursor. The pristine and alkali metal-doped $BiVO_4$ based thin film samples (Area: 1.0 × 1.0 cm^2) were prepared on fluorine-doped tin oxide (FTO) glass substrate (Aldrich Chemistry: 2.3 mm thick, ~7 Ω/sq surface resistivity). The liquid ink was sprayed with a 0.1 ml/min flowrate over FTO glass held at 70 °C. An optimum film thickness of ~ 520 nm was coated with two cycles of spraying followed by heat-treatment (Thermo Scientific Thermolyne: Model: F48028) at 500 °C in the air for 2 h (Figure 8a).

Figure 7 Ultrasonic spray coating machine for thin-film fabrication

Atmospheric pressure chemical vapor deposition (APCVD) was used for the thin film deposition using a tubular furnace, as is shown in Figure 8b.

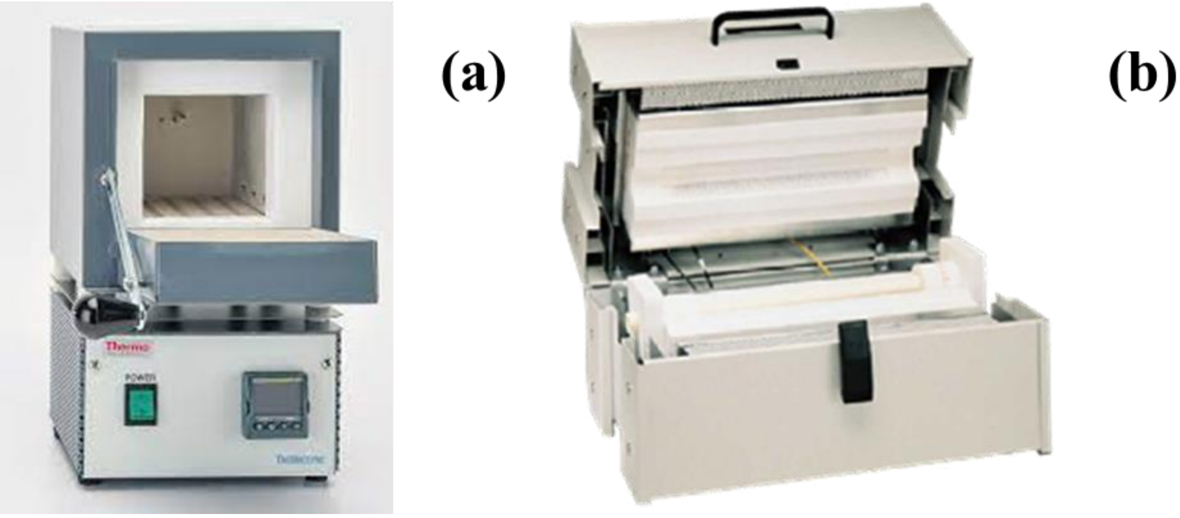

Figure 8 used (a) muffled furnace and (b) tubular furnace for the thin film fabrication.

The vapor was generated by heating an appropriate amount of powder/solid material in the tube furnace's upstream section at the specific temperature where it converted from solid to vapor. Argon was used as a carrier gas to carry the vapor downstream, where the substrate was placed in the hot zone of the tubular furnace. The prepared films are shown in Figure 9a. Figure 9b shows stack base structured films with all intermediate deposition steps.

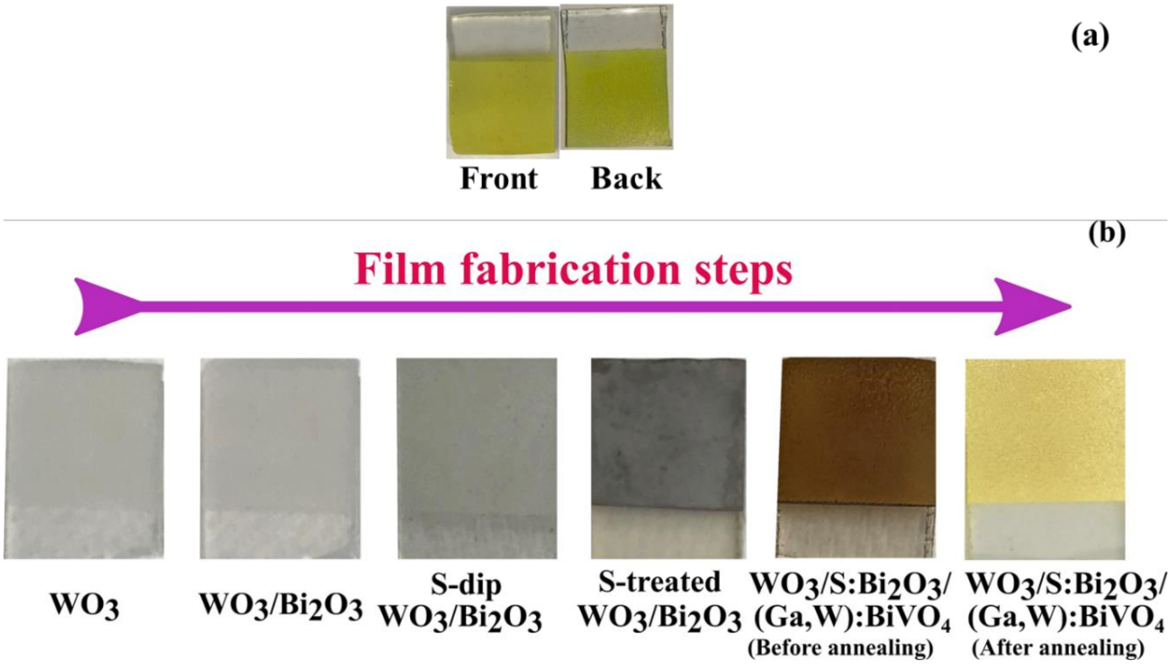

Figure 9 (a) prepared thin film front and back view, (b) various intermediate thin films of the stack-based film structure.

2.3 Electrode fabrication from thin films

Photoanodes were constructed from the prepared thin films by attaching a copper wire to the FTO, and silver paint was used to establish electrical contact. Epoxy (Loctite 9460) was applied to secure the connection and cover the copper wire, silver paint, and FTO edges. The active surface area was measured by scanning the electrode surface. An electrode fabrication from the thin film is shown in Figure 10.

Figure 10 Fabricated electrodes from the thin film

2.4 Photoelectrochemical measurement

The PEC performance of the photoanodes was evaluated in a standard three-electrode configuration using Pt wire (Premion 99.997%) and Ag/AgCl (3M NaCl filling solution) as a counter and reference electrodes, respectively. A solar simulator (Sun 3000, model#11000A, ABET Technologies, USA) was used as the light source. Simulated AM 1.5G illumination was established using a GaInP (bandgap: 1.8 eV) photovoltaic primary reference cell. Potentiostat/galvanostat (BioLogic SP-300) was used for photoelectrochemical (PEC) measurements in 0.1 M KPi solution in water (pH = 8.0). The setup for the photoelectrochemical measurement is shown in Figure 11.

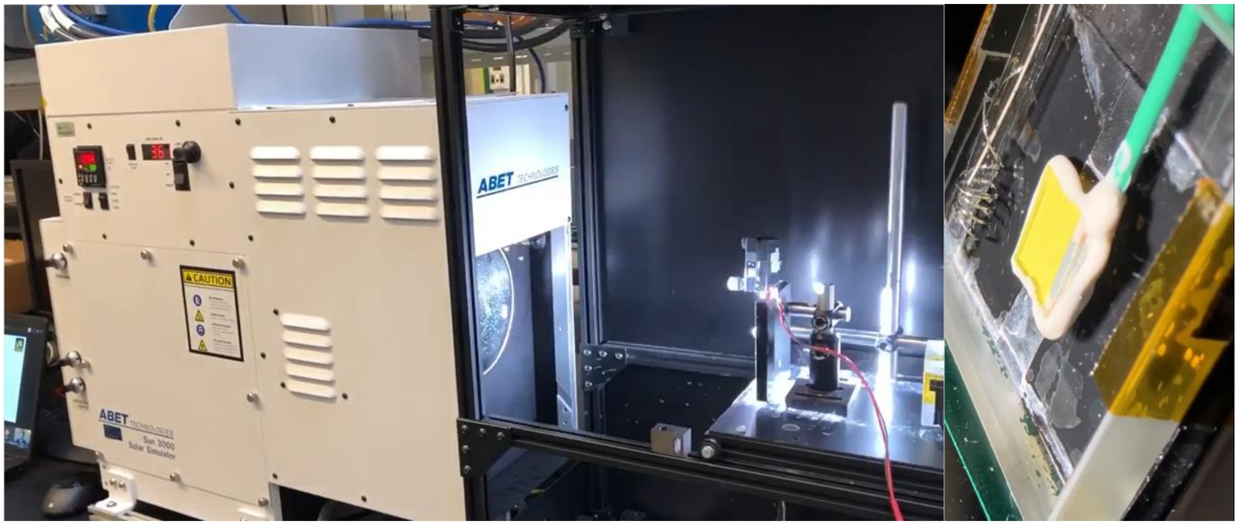

Figure 11 photoelectrochemical measurement station contains solar simulator, 3 electrode setup and potentiostat.

The electrolyte was degassed with N_2 gas for about 20 min before every measurement. Incident photon-to-current efficiency (IPCE) measurement was conducted using a 300 W Xe lamp (Newport, 66883), monochromator (Acton SpectraPro-150), mono-Si cell (Hamamatsu) and potentiostat (VersaSTAT 4 Ametek, Princeton Applied Research) with a lock-in amplifier (SR530 Stanford Research System). The setup is illustrated in Figure 12. A 495 nm long-pass filter (Newport) was added after the monochromator for wavelengths > 550 nm to filter second-order diffraction.

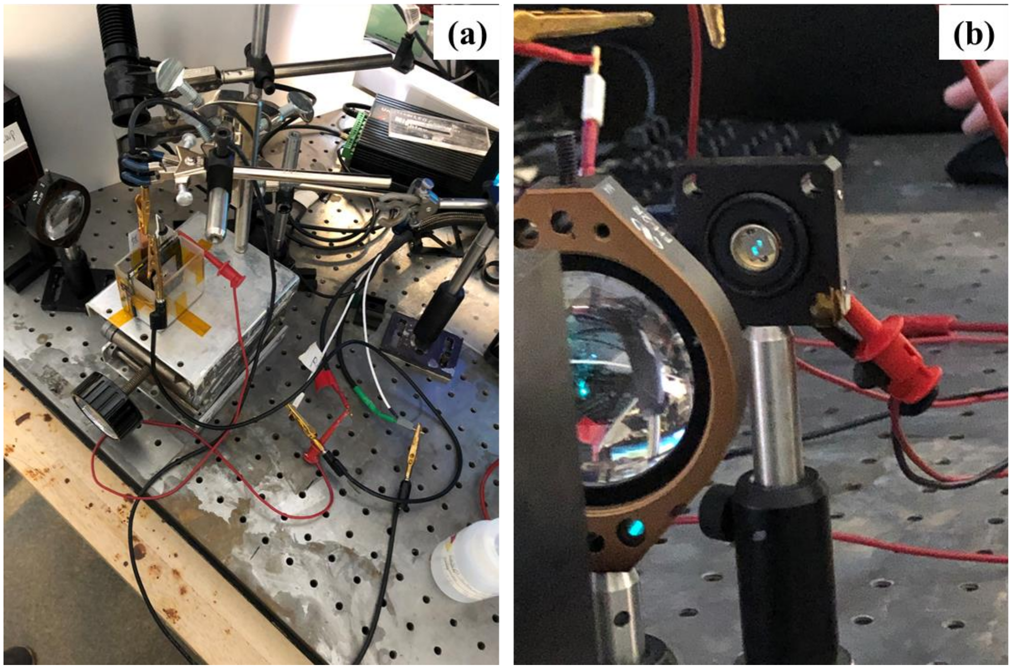

Figure 12 Incident photon-to-current conversion efficiency (IPCE) (a) complete setup and (b) beam size and focus.

The photocurrent was also measured with a hole scavenger (Na_2SO_3), where the electron-hole recombination is considered almost negligible.[84] Electrochemical impedance spectroscopy (EIS) measurements were performed at a frequency range of 100 kHz to 100 mHz under simulated AM 1.5G illumination. Mott-Schottky estimated flat band (onset) potential–Schottky at 1 kHz in the dark with AC amplitude of 20 mV at 1.23 V vs RHE in 0.1 M K_2HPO_4 electrolyte (pH 7.5) by the relationship given in equation (6).[33]

$$\frac{1}{C^2} = \frac{2}{(\varepsilon\varepsilon_0 A^2 e N_D)}\left(V_{app} - V_{FB} - \frac{K_B T}{e}\right) \qquad (6)$$

Where C is the capacitance in space charge region; ε is relative permeability which is taken as[85] for the calculation; ε_0 is vacuum permeability (8.8×10^{-12} F m^{-1}); A (cm^2) is the area of the photoanode thin film; e is the charge of an electron (1.602×10^{-19} C); N_D is the number of charge carrier per cm^{-3}, estimated from Mott-Schottky measurement plot; V_{app} (in RHE) is the applied potential; V_{FB} is the flat band potential measured from Mott-Schottky plot; K_B is Boltzmann constant ($1.38 \times 10\text{-}23$ J K^{-1}); T (K) is the temperature at which the measurement is performed (298 K).

The majority of the photoelectrochemical measurements were conducted by illuminating 1 sun from the back of the thin film (through the glass). Since $BiVO_4$ is mainly composed of electron-hole pairs that are generated within the film's thickness, they need to travel across the film's entire thickness to the $BiVO_4$/FTO interface. The rate-limiting step is a crucial step in the design of photoelectrodes. It can be used to evaluate the efficiency of the collector and the film thickness. Since electron-hole pairs in $BiVO_4$ are mostly generated within the penetration length of the light (∼100 nm), the electrons need to travel across the entire thickness of the film to the $BiVO_4$/FTO interface for collection when illumination is from the front. The optimized thickness photoanode is considered to be approximately 500 nm for $BiVO_4$ and 200 - 250 nm for Bi_2O_3 and WO_3.So back illumination will facilitate the electron to rapidly moved to the electron collector, as illustrated in Figure 13.

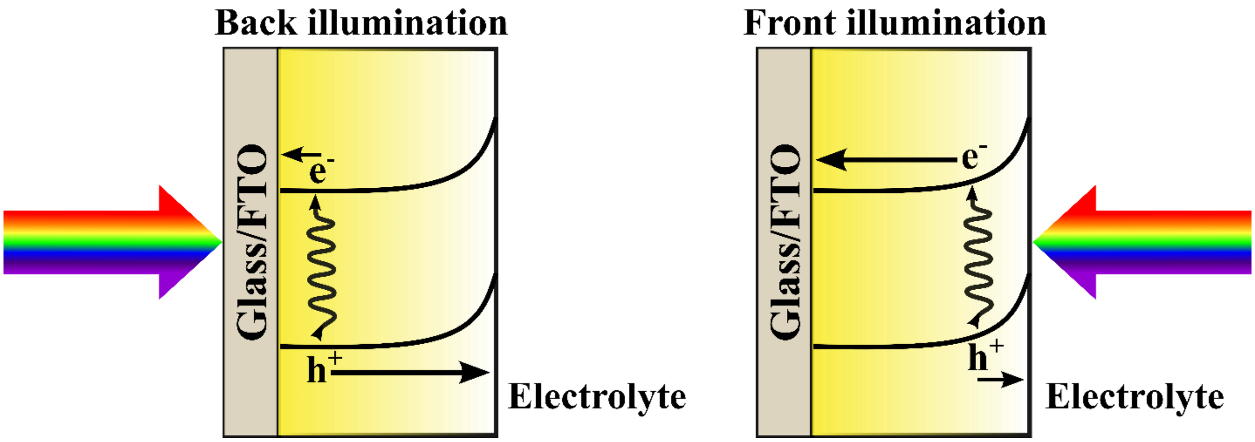

Figure 13 Significant of front and back light illumination on the electrode sample.

2.5 Process of hydrogen collection

The H_2 and O_2 gases generated in the PEC process were collected in a three-electrode setup by tracking the electrolyte volume from a filled tube.[86] The faradaic efficiency (η_{H_2}) was calculated using equation (7).

$$\eta_{H_2} = \frac{\frac{P_{H_2}V}{RT}}{(Columbs\ passed)\times(\frac{mol\ e^-}{96485C})\times(\frac{mol\ H_2}{2mol\ e^-})} \qquad (7)$$

Where P_{H_2}, V, R and T are pressure from H_2 evolution (hPa), volume (L), gas constant (0.08206 L atm $K^{-1}mol^{-1}$) and T temperature (K), respectively. P_{H_2} was calculated by subtracting the water vapor pressure ($P_{H_2O\ Vapor}$) and pressure from the suspended solution ($P_{suspended}$) from atmospheric pressure (P_{atm}) measured using a barometer, by equation (8).

$$P_{H_2} = P_{atm} - P_{H_2O\ Vapor} - P_{suspended} \qquad (8)$$

Where, $P_{suspended}$ is calculated by measuring the height (h_1) of the suspended solution above the solution level in the setup. The equation (9) is used for the calculation.

$$P_{suspended} = h_1 \times \frac{Hg\ Density}{Solution\ density} \times \frac{1\ atm}{760\ mm\ Hg} = h_1 \times 0.0736\ (torr^{-1}mm^{-1}) \quad (9)$$

The faradic efficiency measurement was validated using Pt electrodes as an anode and cathode for the electrolysis and obtained η_{H_2} 0.98±0.02. The measurement was conducted at 1.23 V_{RHE} in KPi electrolyte under simulated AM 1.5G illumination. A typical setup is shown in Figure 14.

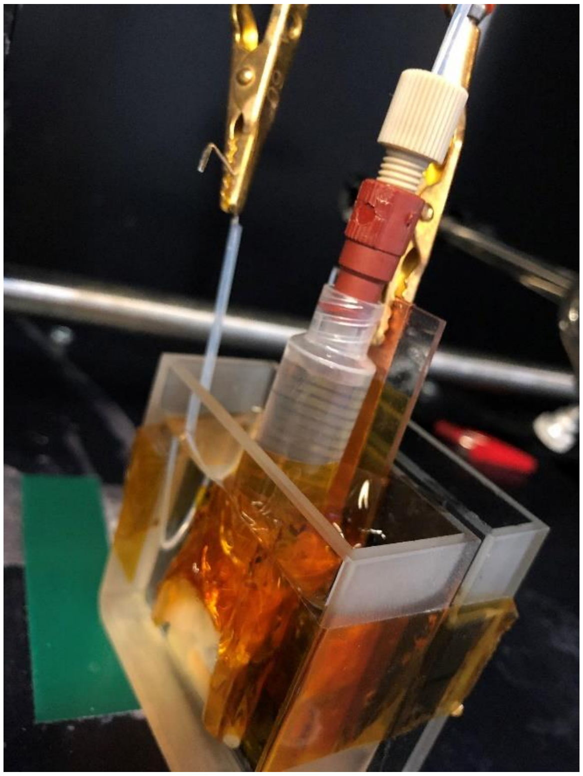

Figure 14 Hydrogen collection setup

2.6 Important equations and calculation processes

Photoelectrochemical measurements

The reference electrode potential was converted to reverse hydrogen electrode (RHE) by the relationship given in equation (10).

$$E_{RHE} = {E_{Ag/AgCl}}^{0} + E_{Ag/AgClSCE} + 0.059\,pH \qquad (10)$$

$$Where\ \ {E_{Ag/AgCl}}^{0} = 0.1976\,V\ vs.RHE, at\ 298\ K$$

Process of theoretical photocurrent (J$_{theoretical}$ calculation)

The light-harvesting efficiency (LHE) or absorption efficiency (ϕ_{abs}) relationship is show in (equation (11))

$$LHE = 1 - 10^{-A(\lambda)} \quad = \phi_{abs} \qquad (11)$$

Where A is absorbance with wavelength (λ)

The absorption efficiency was calculated by integrating absorption spectra from wavelength 300 to 550 nm for all samples.

Further, photon energy and photon flux were calculated from AM1.5G solar irradiance with wavelength by following relation (equation (12-14)).

$$E(\lambda) = h \times C/\lambda \qquad (12)$$

$$Where, E(\lambda){:}\,photon\ energy \quad h{:}\,Plank\ constant \quad C{:}\,speed\ of\ the\ light$$

$$Number\ of\ photons = h \times C/\lambda \qquad (13)$$

$$Photons\ flux\ (\phi\,(\lambda)) \ = P(\lambda)/E(\lambda) \qquad (14)$$

The theoretical photocurrent was calculated using the above-calculated data assuming 100% incident to photon conversion efficiency (IPCE) and by the following relationship.[33,61]

$$J_{theoretical} = \int_{\lambda_1}^{\lambda_2} e \times \phi(\lambda) \times LHE \times d\lambda \qquad (15)$$

Charge transport calculation: bulk and surface

Major losses in theoretical photocurrent are electron-hole recombination in bulk and at the surface, which are known as charge separation (η_{sep}) and charge transfer or charge injection efficiency (η_{trans}), by relationship equation (16 and 17).

$$J_{H_2O} = J_{theoretical} \times \phi_{sep} \times \phi_{trans} \qquad (16)$$

The transfer efficiency is almost 100% in the presence of hole scavengers, given by relationship equation (10).[61]

$$J_{Na_2SO_3} = J_{theoretical} \times \phi_{sep} \qquad (17)$$

Using equations (16 and 17), the η_{sep} and η_{trans} can be calculated

IPCE calculation

The IPCE was measured by the relationship given in equation (18)

$$IPCE = \frac{Number\ of\ electrons}{Number\ of\ photons} = \frac{J_{monochromator} \times h \times C}{P_{monochromator} \times \lambda} \qquad (18)$$

Integrated current calculation

Integrated current ($J_{integrated}$) was calculated using the relationship given in eq (19)

$$J_{Integrated} = \int_{\lambda_1}^{\lambda_2} e \times \phi(\lambda) \times IPCE \times LHE \times d\lambda \qquad (19)$$

2.7 State-of-the-art material characterization

It is imperative to evaluate the photocatalytic behavior of $BiVO_4$ thin film to understand overall water oxidation kinetics. Various electrochemical studies, material characterization, theoretical studies were performed to understand the semiconductor surface, bulk and surface/electrolyte interface characteristics of semiconductor and photogenerated charge carrier properties. A list of evaluation techniques is given in Table 1.

The PEC performance of the prepared photoanode was evaluated in a standard three-electrode configuration using Pt mesh and saturated calomel electrode (SCE) as a reference and photoanode as a working electrode, respectively. A solar simulator, equipped with AM 1.5G filter (calibrated for 1 sun (100 mW.cm^{-2})) as a light source along with a potentiostat/galvanostatic used for photoelectrochemical measurements in the electrolyte.

The light absorption behavior of the photoanode was examined by measuring incident photon-to-current efficiency (IPCE). It is the ratio of total photocurrent versus the rate of incident photons as a function of wavelength[87]. IPEC considers major efficiencies such as photon absorption/charge excitation, charge transport in bulk ($\eta_{separation}$) within the solid and interfacial charge transfer across the solid-liquid interface ($\eta_{transfer}$)[87]. Further, based on photon absorption, absorbed photon-to-current efficiency (APCE)[88] was measured to determine the absorbed photon to current conversion rate. The Mott-Schottky analysis determines the U_{fb}, W_{SC}, VB and CB edges[33]. Besides, the amount of band bending can be calculated as per the procedure explained[33].

The crystal structure, crystallinity, phase change and phase composition of the synthesized thin film were determined by X-ray diffraction (XRD) analysis. The main observed peaks in the scheelite monoclinic $BiVO_4$ at 18.6°, 18.9°, 28.58°, 28.82°, 28.94° and 30.5° correspond to (110), (011), (-130), (-121), (121) and (040) crystal planes[36]. Detecting the doping oriented peaks in XRD depends on the doping level, small substitutional doping (2-5%) does not make any change in the crystal structure of $BiVO_4$, but slight changes in the lattice parameters are possible[36,61] such as a small shift in the peaks were observed along with a change in the overall volume on Li doping in $BiVO_4$[88]. Raman analysis predicts the change in the atomic arrangement in the crystal lattice after modifying the pristine semiconductor, such as a shift in the peaks towards lower wavenumber predicts the increment in the overall crystal symmetry after doping and co-doping in the $BiVO_4$[33]. Also, change in bond length confirm the effect from modification such as doping can increase bond length[33].

Scanning electron microscopy (SEM) determines the surface morphologies of nanostructure along with the grain size and porosity of the thin film[61]. Energy-dispersive X-ray spectral (EDX) mapping analysis estimate the composition of the prepared thin film[57]. X-ray photoelectron spectroscopy (XPS) analysis examines elements' oxidation state and provides information if their surroundings are getting affected by doping[88]. Atomic force microscopy (AFM) provides insight into structural and optoelectronic properties. It can even illustrate (photo)current mapping that reveals nanoscale, (opto)electronic heterogeneity across the film[89]. Along with the conductivity measurement of the thin film, AMF can provide the charge transport mechanism through single current-voltage curves[89]. Transmission electron microscopy (TEM) provides details about microstructural characteristics, lattice fringe spacing and selected area electron diffraction (SAED)[90].

The electron probe microanalyzer (EPMA) was applied for composition analysis of the thin film when surface modified during post-synthesis, such as nitrogen treatment of $BiVO_4$ surface. In this case, the quantity of nitrogen incorporated in the lattice structure of $BiVO_4$ can be estimated through EPMA[91]. Inductively coupled plasma mass spectrometry (ICP-MS) also provides the composition of the thin film[88]. Both ICP-MS and EPMA provide the composition of the thin film based on different principles[88,91]. Photoluminescence (PL) emission spectra originate from the radiative recombination of electrons and holes that can help in understanding the recombination process and lifetime of photogenerated electrons and holes[61]. Ultraviolet-visible spectroscopy (UV-vis) and diffuse measurement provide information about the thin film behavior towards the light, such as absorbance, reflectance, transmittance. Other parameters, optical band gap, light-harvesting and absorbance efficiency (LHE)[33,36,57].

To estimate the diffusion length of electron-hole pairs and correlation with the defect density, the Depth dependent Doppler broadening spectroscopy measurements were conducted using a slow positron accelerator[36] with the Doppler broadening spectra at increasing positron implantation energies (E, keV) are recorded using a HPGe detector (energy resolution 2.0 keV at 1332 keV of ^{60}Co). The spectra have been analyzed through line shape, S (ratio of counts in the low momentum (central) region (511±0.760 keV) to the total area of the annihilation peak) and W (ratio in the high momentum (wing) region ($3.23\ \text{keV} \leq |\gamma\text{-}511\text{keV}| \leq 6.65\text{keV}$) to the total area of the photopeak) parameters.

To investigate the role of Na or K doping on the defect types and density in the $BiVO_4$ films, the *S*-*E* profiles have been fitted using VEPFIT[37]. According to VEPFIT, *S*-parameter at particular implantation energy (*E*, keV) in a sample having *n* number of layers is expressed as

$$S(\mathrm{E}) = f_s S_s + f_1 S_1 + f_2 S_2 + \ldots\ldots + f_n S_n$$

For the present study, two layers model has been considered for the pristine or doped films on the FTO substrate.

Time-resolved microwave conductivity (TRMC) provides the lifetime of photogenerated electrons and holes, which is a critical parameter to determine the photoactivity of semiconductor[92]. Free charge carriers generated by nanosecond laser pulses induce a change in the microwave power reflected from the sample. This change can be correlated to the photoinduced change in the conductivity of the sample, which provides the lifetime and diffusion length of photogenerated electrons and holes[92]. Transient diffuse reflectance spectroscopy (TDRS) analysis focuses on the effect of carrier dynamics during the photocatalytic reaction, especially the difference of the crystal phase[93]. Transient absorption spectra (TAS) provide details about the photogenerated electrons and holes dynamics at an applied bias. The decay time constant of photogenerated electrons and holes can be estimated with applied bias[94] to predict the complete dynamic of photogenerated electrons and holes. Time-resolved Terahertz Spectroscopy (TRTS) determines the electrons and holes properties[95], where semiconductors illuminated with the femtosecond laser pulse generate electrons and holes that absorb THz probe radiation and can be detected by a decrease in transmitted or reflected THz power. This decrease can provide details about photogenerated electrons and holes conductivity, which leads to finding out mobility and diffusion length.

Apart from photoelectrochemical and characterization, a theoretical study using the first-principles density functional theory (DFT) as implemented in the Vienna *ab initio* simulation package (VASP) provides a fundamental understanding of the electronic properties of $BiVO_4$[96]. The DFT analysis bestows deep insight by estimating optimum structure, formation energy, electronic band structure, absorbance and the site-projected density of states (PDOS) on the doping in the $BiVO_4$ structure[97].

The DFT calculations, which include structural optimizations and electronic properties, were carried out using the Vienna *Ab initio* Simulation Package with generalized gradient approximation. In specific, the Perdew-Burke-Ernzerhof exchange-correlation functional and the projector-augmented wave potentials were employed. The Bi_d, V_pv, Os_pv, K_sv, and Na_sv were used as a potential for all the calculations. The Bi (5d, 6s, 6p), V(2p, 3d, 4s), O(2s, 2p) and alkali metals (1s, 2s, 2p) electrons were treated as valence electrons. Plane wave functions with a kinetic energy cutoff of 600 eV were used to describe the wavefunction of electrons. The reciprocal space is meshed as 5 × 5 × 7 using the Monkhorst–Pack method for all unit cell structure relaxations. The electronic band structure is plotted along the high-symmetry lines along the directions L(-0.5, 0, 0.5)-M (-0.5, 0.5, 0.5) -A(-0.5, 0, 0)-Γ (0,0,0)-Z(0, -0.5, 0.5)-V(0, 0, 0.5). The energy convergence criterion for electronic iterations is set to be 10^{-5} eV. The DFT+U method was used to improve the description of the highly localized d-electron correlation in the transition metal

V with a Hubbard U value of 2.7 eV. The formation energies for Na placement into the $BiVO_4$ interstitial position was calculated using,

$$\mathrm{E}_{F,interstitial} = E_{Na:BiVO_4} - E_{BiVO_4} - E_{Na}$$

$E_{Na:BVO_4}, E_{BiVO_4}, and\ E_{Na}$ are the free energies for the Na doped $BiVO_4$, pristine $BiVO_4$ and single Na atom.

Table 1 Thin-film fabrication methods, material characterizations, theoretical analysis and various calculated parameters applied to determine the photocatalytic performance of $BiVO_4$.

Fabrication technique	**Photocatalytic evaluation**	**Characterization**	**Theoretical analysis**	**Parameters**	
Metal-organic	Photocurrent density with	XRD, Raman spectroscopy	Structure optimization	Light-harvesting	Bulk/surface capacitance

decomposition	hole scavengers			efficiency	
Sol-gel method, precipitation method	Transient current	SEM, EDX, TEM,	Static calculation	Absorption efficiency	Bulk/surface resistance
Spray pyrolysis, ultrasonic spray coating	Electrochemical Stability	XPS, AMF, photoluminescence	Density of State (DOS)	Separation efficiency	Charge transfer rate constant in the bulk and surface state
Dip coating and Drop cast method	Cyclic voltammetry	ICP-MS, EPMA	Bandgap calculation	Injection efficiency	Number of charge carrier density bulk and surface
Spin coating	Mott-Schottky	UV-Visible and diffuse reflectance	Electronic band structure	Total efficiency of photoanode	Electrochemical surface area (ECSA)
Sputter coating	Impedance measurement (EIS)	Time-resolved microwave conductivity	Dielectric calculation for absorbance	Total charge retention	Charge transfer kinetics
Hydrothermal	IPCE/APCE	TAS (transient absorption spectra)	Projected density of states	Band gap calculation	Rietveld refinement
Electrode deposition	Open circuit potential (ΔOCP)	Transient diffuse reflectance spectroscopy	Formation energy	ABPE	Width of space charge region (WSCL)
Chemical vapor deposition	Amount of H_2 and O_2 gas evolution	Time-resolved Terahertz Spectroscopy	Polaron hopping analysis	Amount of band bending	Density of state and Fermi level determination
Vacuum deposition methods	Surface state determination	Doppler broadening spectroscopy measurements	Adsorption energy calculation	Valence and conduction band edges	Electro-hole pairs diffusion length

CHAPTER 3 ALKALI METAL PLACEMENT IN THE CRYSTAL STRUCTURE OF BIVO$_4$

3.1 Introduction

Several attempts have been made to improve the performance of $BiVO_4$ through doping[36], junction formation[98] and nano-structuring[99] and adding electron transfer layer[66] and hole transfer layer[100]. Among these strategies, employing p-n homojunction is a useful technique for promoting band alignment, charge separation and transfer due to the built-in internal electric field at p-n junction[101,102,103]. Doping with transition metals (IIIA to VIIA group elements) has been proven to be one of the practical approaches for increasing OER reaction by enhancing diffusion length, charge carrier separation/transport, and light absorption by reducing band gap[104,92,105]. According to Wang et al.[106], the HER and OER reactions can be promoted by doping for enhancing active sites, lowering overpotential, and improving durability. Ritcher et al.[107] has determined that Na and K doped TiO_2 nanotubes can reduce the external bias and induce charge transfer by forming a strong ionic bond and modifying the electronic band structure. Whereas Grewe et al.[108] illustrated that Na and K doping in mesoporous Ta_2O_5 without any structure change led to superior water splitting performance. The elements such as S, H and N are incorporated into the $BiVO_4$ lattice, and their effect on diffusion length, absorption and charge transport have been studied extensively[109–111]. Marlene et al.[109] has studied sulfur incorporation in the oxygen site in $BiVO_4$ and evaluated the bandgap reduction and the increase in careers mobility and diffusion length. Jang et al.[110] subjected $BiVO_4$ surface to mild hydrogen treatment for improving carrier mobility and lifetime through hydrogen bonding with oxygen. Irani et al.[111] demonstrated significant enhancement in optical absorption and bandgap reduction by nitrogen doping at vanadium sites in $BiVO_4$. However, there has not been any systematic study on the alkali metal doping in the $BiVO_4$ structure.

In the present study, the role of alkali metal (Li or Na or K) doping in the $BiVO_4$ lattice structure improves light absorption, electron-hole pairs bulk diffusion length, and surface charge transfer for photoelectrochemical water splitting was systematically investigated. The doped $BiVO_4$ thin films prepared using ultrasonic spray coater exhibited planner surface morphology with interconnected nano porous grains. Depth-dependent Doppler broadening spectroscopy measurements were employed for analyzing the bulk diffusion length of charge pair and correlated with the defect density. The placement of alkali metal in the interstitial position of $BiVO_4$ crystal structure resulted in the reduction of the Bi and V voids due to shared interaction of doped alkali metal, Bi and V, with lattice oxygen atoms. The effect was highly significant in the Li and Na doped $BiVO_4$ film compared to that with K. The density functional theory confirmed the formation of multiple interbands with optical band gap reduction with Li and Na doping, resulting in the extended light absorption, enhanced charge separation in the bulk and surface transfer during PEC process. The Li:$BiVO_4$ and Na:$BiVO_4$ photoanode showed the highest photocurrent density of 2.35±0.15 and 1.82 ±0.1 $mA.cm^{-2}$ in 0.1 M K_2HPO_4 electrolyte under 1 sun illumination at 1.23 V_{RHE}.

3.2 Preparation of alkali metals doped $BiVO_4$ thin film

The pristine and alkali metal doped $BiVO_4$ based thin film samples (Area: 1.0×1.0 cm^2) were prepared on fluorine-doped tin oxide (FTO) glass substrate (Aldrich Chemistry: 2.3 mm thick, ~7 Ω/sq surface resistivity) using ultrasonic spray coating technique (Sono-Tek Corporation, USA)[33]. Precursor solution of $BiVO_4$ in 3mM $Bi(NO_3)_3{\cdot}5H_2O$ (Alfa-Aesar, CAS#10035060) and 3 mM NH_4VO_3 (Sigma-Aldrich, CA

S#7803556) in 2M HNO_3 (Sigma-Aldrich, CAS#7803556) was sprayed at a 0.1 ml/min flow rate over FTO glass at 70 °C. An optimum film thickness of ~ 520 nm was coated with two cycles of spraying followed by heat-treatment (Thermo Scientific Thermolyne: Model: F48028) at 500 °C in the air for 2 h (see Figure 15). Alkali metal (Li or Na or K) doping in the $BiVO_4$ (2 to 6 wt. %) was carried out by adding sodium hydroxide (Sigma-Aldrich, CAS#1310732) or potassium hydroxide (Sigma-Aldrich, CAS# 1310-58-3) in the $BiVO_4$ precursor solution.

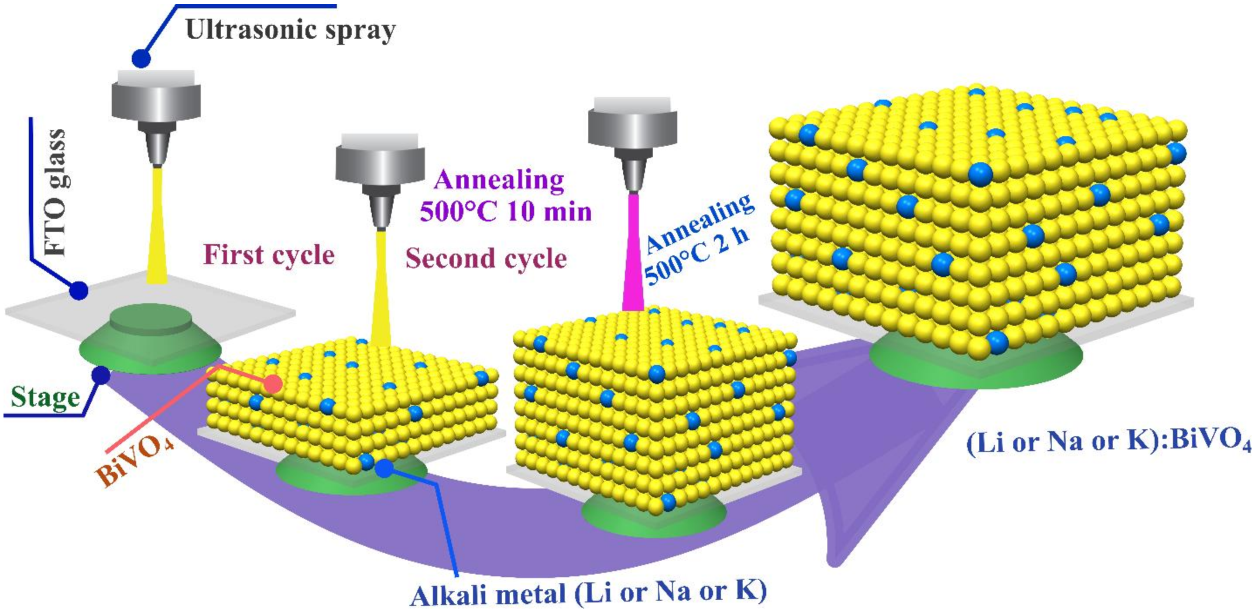

Figure 15 Schematic illustration of alkali metal-doped $BiVO_4$ film fabrication process.

3.3 Photoelectrochemical measurements

The enhanced water oxidation performance of alkali metals (Li, Na, K) doping in the $BiVO_4$ system is evaluated by measuring PEC performance. It was observed from Figure 16a that with individual Li, Na and K doping in $BiVO_4$, the photoanode Li:$BiVO_4$ showed

PCD (2.35±0.15 and 6.2±0.30 mA.cm^{-2} at 1.23 and 2.0 V vs RHE, respectively), which is 24 times pristine $BiVO_4$, Na:$BiVO_4$ shown PCD of 1.82±0.1 mA.cm^{-2} which is 17 times corresponding to the pristine $BiVO_4$ (0.11±0.01 mA.cm^{-2}) measured at 1.23 V vs RHE in 0.1 M K_2HPO_4 (pH: 8.0) under 1 sun illumination. Furthermore, K doped $BiVO_4$ demonstrated improved performance (0.85±0.04 mA.cm^{-2}) up to 8 times than pristine $BiVO_4$. Further, the nature of alkali metal-doped $BiVO_4$ photoanodes PEC performance was measured in hole scavengers (Na_2SO_3) for the sulfite oxidation, which makes the electrons and holes recombination almost negligible.

The investigation of obtained PCD was further elaborated by transient current measurement under chopped light for 5 sec up to 120 sec at 1.23 V vs RHE for the water and sulfite oxidation. It can be observed that the photocurrent is highest at the beginning of the first light illumination and then decreases gradually to some degree. However, this behavior decreased mostly after few cycles. This is because the charge accumulation is maximum at the first illumination of light then electron-holes recombination takes place. These recombinations are most evident in $BiVO_4$ and least for Na:$BiVO_4$ & Li:$BiVO_4$.

To understand the enhanced overall water splitting performance of alkali metals doped BiVO4 photoanode, light absorption behavior on the surface of the photoanode was studied. As given in Figure 16b, the onset of the light absorption for pristine $BiVO_4$ starts from ~510 nm. However, on alkali metals doping, the light absorption onset improved towards a higher wavelength ~520 nm, 530 and 535 nm for K:$BiVO_4$, Na:$BiVO_4$, Li:$BiVO_{4,}$ respectively. Apart from the improved absorption edge due to alkali metal doping, total absorption improved significantly due to a good amount of absorption even before the absorption onset, speculating the formation of interbands[112]. From Figure 16b inset, among all photoanode, the Li:$BiVO_4$ photoanode has the highest absorption (~75%) followed by Na:$BiVO_4$ (73%), K:$BiVO_4$ (69%) and pristine $BiVO_4$ (64%) due to placement of Li, Na and K in the interstitial position of $BiVO_4$ structure that generate sufficient disorder in the atomic arrangement due to electrostatic interaction and oxygen deficiency. As a result, there will be many active sites forming interband states in the bandgap region. The Li doped samples show the lowest band gap (~2.34 eV) compared to pristine BiVO4 samples (~2.44 eV). This reduction in band gap corresponds to higher light absorption than other prepared samples. This validates more active sites generation on the Li doping compared to Na and K doping with the formation of the inter-band state. The improved absorption property of Li, Na and K doping samples was confirmed by diffuse reflectance and transmittance measurement that shows that the diffuse reflectance is minimum for Li doped samples compare to Na and K doped $BiVO_4$ [113]. The Li:$BiVO_4$ showed improved overall light-harvesting capabilities compared to other prepared photoanodes with the film thickness (~520nm) more than hole diffusion length (~100 nm). The ultimate improvement is to enhance charge separation in the bulk of film more than the hole diffusion length.

In order to illustrate charge separation in the bulk and transport to the reactive surface due to alkali metal doping, the bulk charge separation efficiency (ϕ_{sep}), charge transfer efficiency (ϕ_{trans}) and total efficiency ($\phi_{abs} \times \phi_{sep} \times \phi_{trans}$) of photoanodes were calculated. From Figure 16c, the Li doping has increased ϕ_{sep} up to ~100 % from 27 ± 1.4% of pristine $BiVO_4$, whereas Na doping has increased the ϕ_{sep} up to 91 ± 3.8. This shows that Li doping played a significant role in charge separation in bulk. Respective, the overall efficiency ϕ_{abs}

$\times \phi_{sep} \times \phi_{trans}$ for overall water oxidation kinetics is shown in Figure 16d for all photoanodes. The total efficiency is maximum (40 ± 2%) for Li:$BiVO_4$ photoanode.

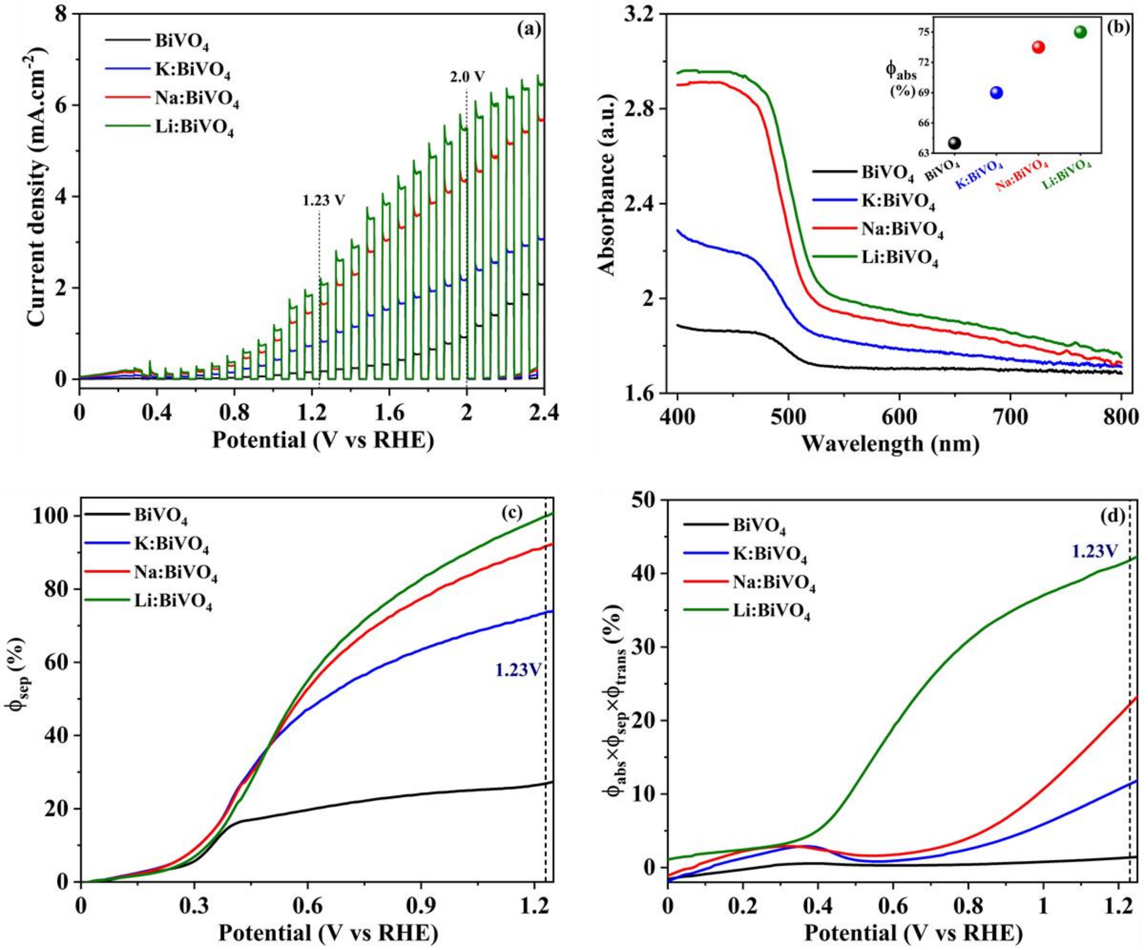

Figure 16 (a) J-V plot for (a) pristine $BiVO_4$, K:$BiVO_4$, Na:$BiVO_4$ and Li:$BiVO_4$ photoanodes. (b) Absorption spectra (inset: absorption efficiency), (c) separation efficiency and (d) total efficiency at 1.23V vs RHE in 0.1 M K_2HPO_4 (pH: 8.0) for pristine $BiVO_4$, K:$BiVO_4$, Na:$BiVO_4$ and Li:$BiVO_4$ photoanodes.

3.4 The incident photon-to-current conversion efficiencies (IPCE)

The incident photon-to-current conversion efficiencies (IPCE) of the photoelectrode are measured at 1.23 V vs RHE (Figure 17). Pristine $BiVO_4$ photoanode demonstrated IPCE from $\lambda \leq 510$ nm. However, on doping with Na and K, the IPCE onset extended up to $\lambda \leq 530$ nm and $\lambda \leq 520$ nm. The Li:$BiVO_4$ photoanodes showed the highest IPCE value 45 ± 3.5 % followed by Na:$BiVO_4$ (38±2%), K:$BiVO_4$ (18±1%) and $BiVO_4$ (4.5±0.2%), respectively at 420 nm. Along with IPCE, Integrated photocurrents were calculated (Figure 17: secondary Y-axis) to obtain current integrated close to experimentally obtained PCD (Figure 16a) at 1.23 V vs RHE for all photoanodes. The integrated current density [113] (shown on the secondary Y-axis) corresponding to the IPCE matches well with the experimental PCD value of 2.2 $mA.cm^{-2}$ at 1.23 V vs RHE for Li:$BiVO_4$. The absorbance (Figure 16b) and the IPCE (Figure 17) values demonstrate the extended wavelength range (400 to 550 nm) by the Li:$BiVO_4$ photoanode towards PEC activity.

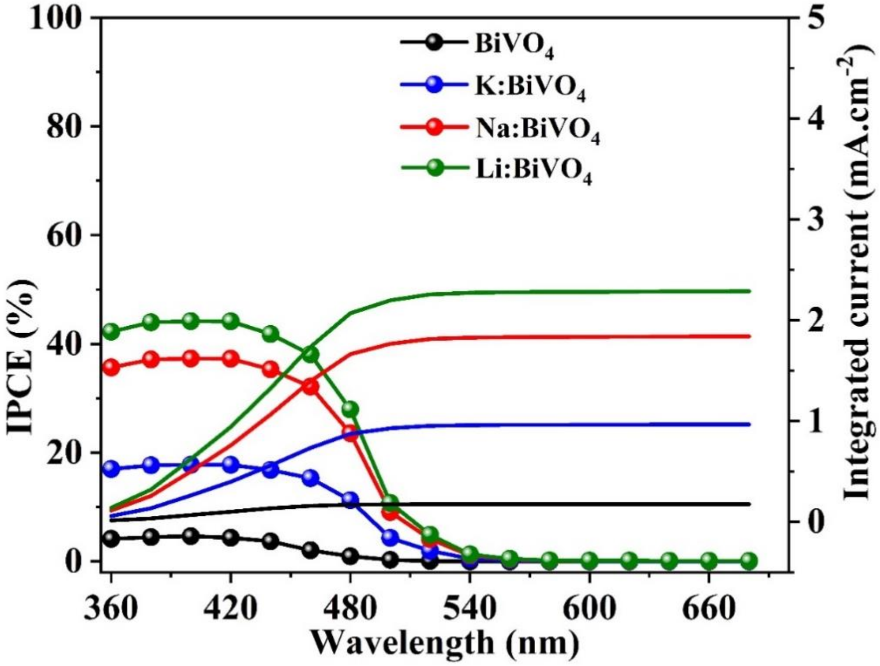

Figure 17 Incident photon-to-current efficiency (IPCE) for BiVO4, K:$BiVO_4$, Na:$BiVO_4$ and Li:$BiVO_4$ photoanodes measured at 1.23 V vs RHE in 0.1 M K2HPO_4 (pH: 8.0) electrolyte under 1 sun illumination. Figure 17: Y-axis demonstrated calculated integrated current.

3.5 XRD and Raman spectroscopy

From the XRD patterns shown in Figure 18, all the peaks were matched with the standard JCPDS #014-0688 and confirmed the clinobisvanite (monoclinic scheelite) structure of $BiVO_4$. Evidently, there were no other impurity phases in the doped samples, validating that 4 wt % doping of alkali metal did not change the crystal structure/space group of the $BiVO_4$ system. However, there were small shift (0.01 – 0.06 °) in the peaks (-121)/ (121) and (040) towards lower 2θ values for the shift relatively higher for the Li and Na doped compared to that with the K:$BiVO_4$ and $BiVO_4$ sample. The shift in the peaks (130), (-121) and (121) was given in Figure 18 to quantify the shift. The lattice parameters a, b and c increased slightly, leading to the unit cell volume expansion (~0.09 or 0.13%) for Li, Na or K doping compared to pristine $BiVO_4$, indicating that the doped atoms occupied in the interstitial position of $BiVO_4$ crystal lattice.

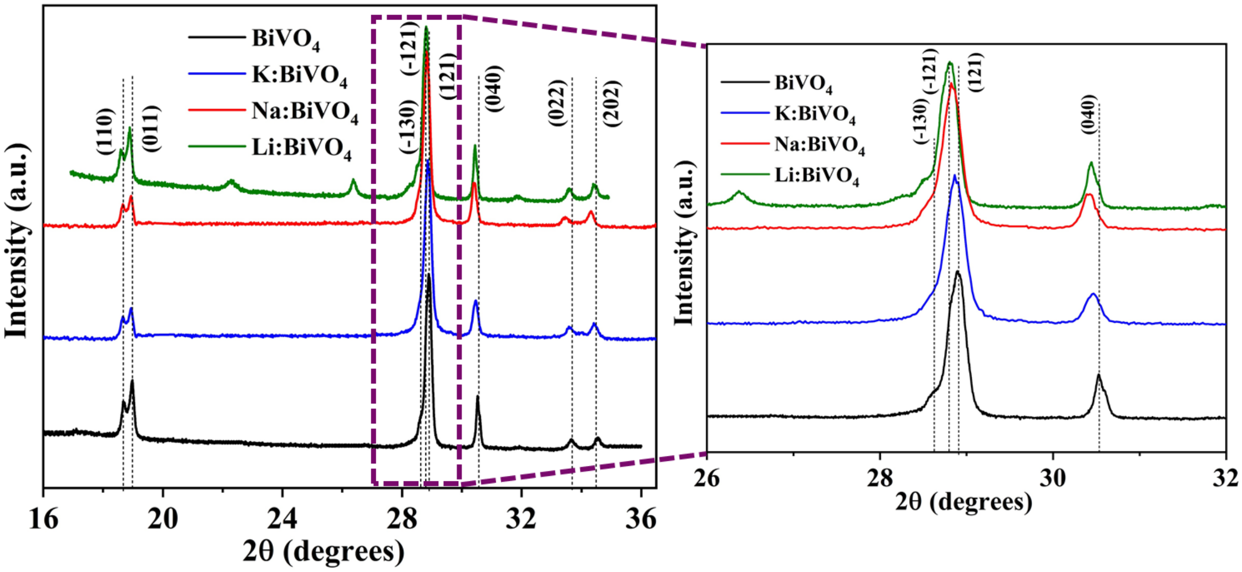

Figure 18 XRD spectrum of pristine BiVO4, K:BiVO$_4$, Na:BiVO4 and Li:BiVO$_4$ films.

Raman analysis (Figure 19) showed a shift in the peak positions of BiVO$_4$ due to the incorporation of alkali metal. The major peaks for pristine BiVO$_4$ sample were observed at 826.46, 365.68 and 332.7 cm$^{-1,}$ corresponding to the δ_s (V-O), δ_s (VO_4^{3-}) and δ_{as} (VO_4^{3-}) stretching mode vibrations, respectively. It was observed that the most intense δ_s(V-O) peak shifted towards higher wavenumber, and it was maximum for the Li:BiVO$_4$ and Na:BiVO$_4$ sample, which confirmed the alkali metal placement in the BiVO$_4$ lattice that distorts the vibrational modes of V-O bond and VO_4^{3-} deformation modes.

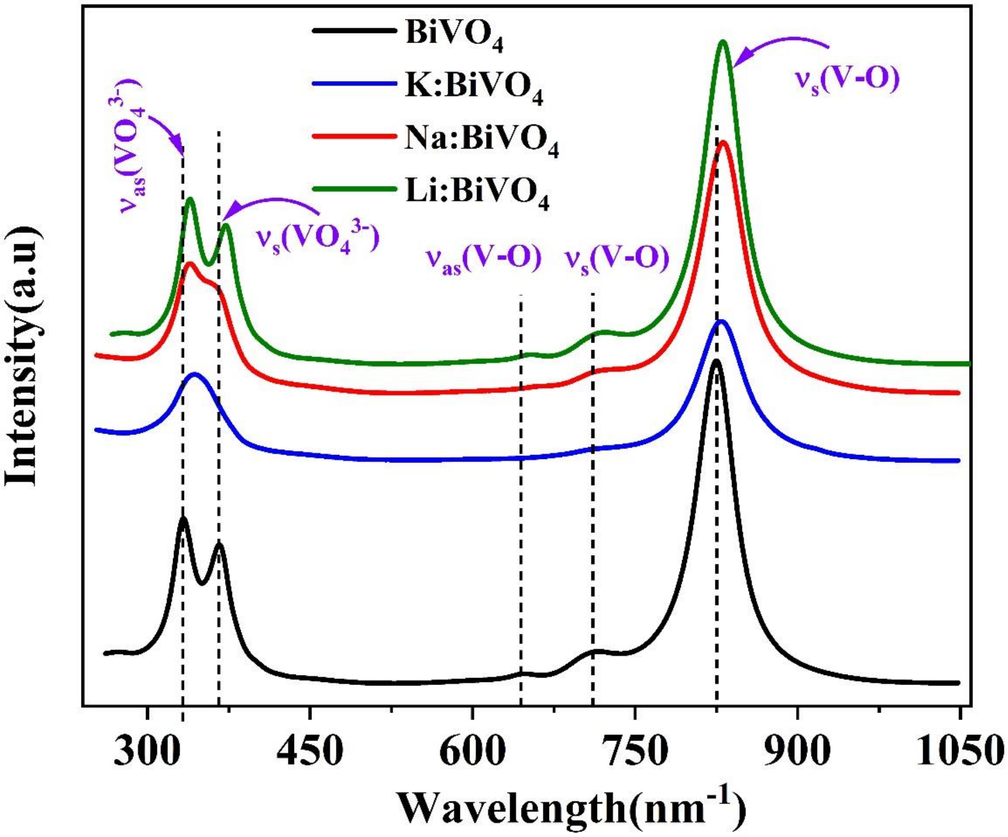

Figure 19 Raman spectrum of pristine $BiVO_4$, K:$BiVO_4$, Na:$BiVO_4$ and Li:$BiVO_4$ films.

3.6 DFT calculations

The first principles of DFT calculations were carried out for the Li and Na doped $BiVO_4$ to validate the experimental results. Figure 20 (i-v) showed the initial placement of one sodium atom in the different interstitial positions in the $BiVO_4$ unit cell, Figure 20 (vi-x) showed the relaxed Na doped $BiVO_4$ structure through the DFT calculations.

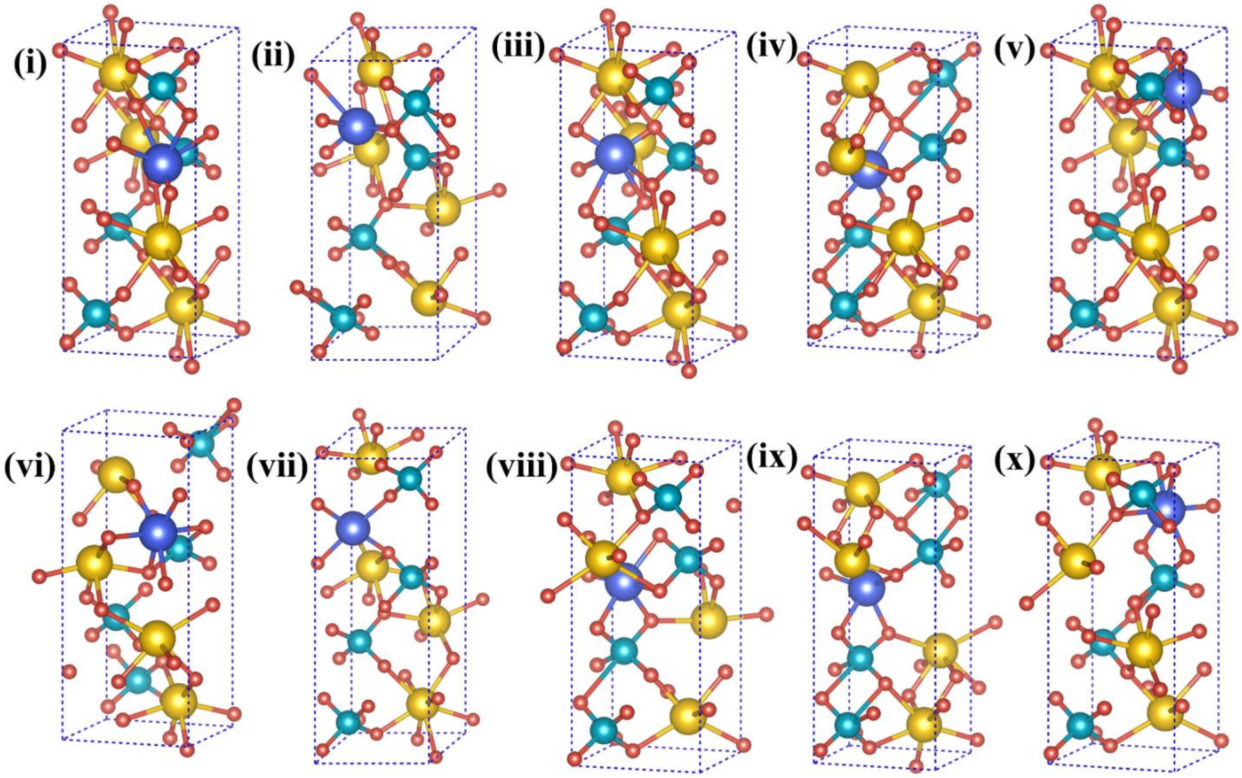

Figure 20 (i-v) various initial placements of sodium atom in $BiVO_4$ lattice, (vi-x) DFT relaxed final structures.

The most energetically favorable configuration for Li and Na placed $BiVO_4$ are shown in Figure 21. It was noticed that 4% Li and Na doping did not affect the space group of the $BiVO_4$ crystal structure.

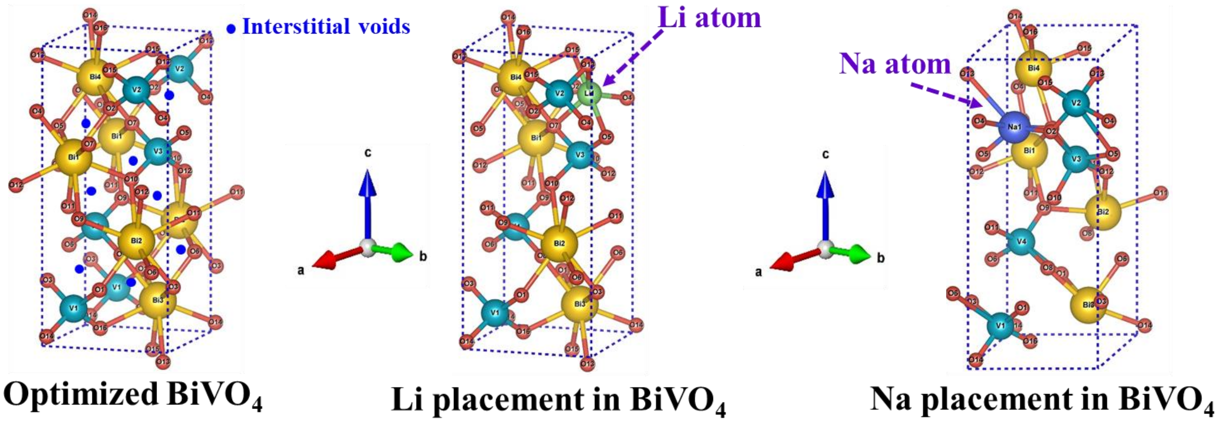

Optimized $BiVO_4$ Li placement in $BiVO_4$ Na placement in $BiVO_4$

Figure 21 Optimized crystal structure of $BiVO_4$ and various interstitial void is also denoted. Optimized crystal structure of Li and Na placed crystal structure.

The simulated band structures in Figure 22a shows the presence of one interband for Li:$BiVO_4$ with reduction of bandgap (2.14 to 2.06 eV) [114,115] for the Li doped compared to the pristine $BiVO_4$. With the Li doping at the interstitial position in $BiVO_4$, both the conduction and valence bands move downward, leading to a reduction in the bandgap by 0.08 eV due to a larger downward shift of the conduction band. Three interbands were observed for Na:$BiVO_4$ in Figure 22b, identified as bands #104 and 105 with the energies at ~ 0.25 eV and band #106 with the energy at ~ 1.8 eV between the valence and conduction bands. These interbands appeared mainly due to atomic distortion generated by Li and Na doping in the interstitial position in the $BiVO_4$ system. It was observed that the electron-occupied interband 104 is dominated by 62.8% p_z orbital mainly located at four oxygen atoms (O5, O7, O10, O12) which are nearby Na to form a Na-O bond (for O5, O7) and V-O and Bi-O bonds (for O10, O12). The electron-occupied interband #105 is mainly contributed by ~95% d_{z2} orbital locating at the V3 atom forming Na-V bond. Finally, the unoccupied interband #106 is dominated by mostly 97% dz2 orbitals at V1 and V2 atoms, forming V-O bonds near the doping Na element. The presence of these interbands results in a slight reduction of band gap by 0.04 eV for Na:BiVO$_4$ (2.19 eV) compared to pristine BiVO$_4$ (2.23 eV) [116,117].

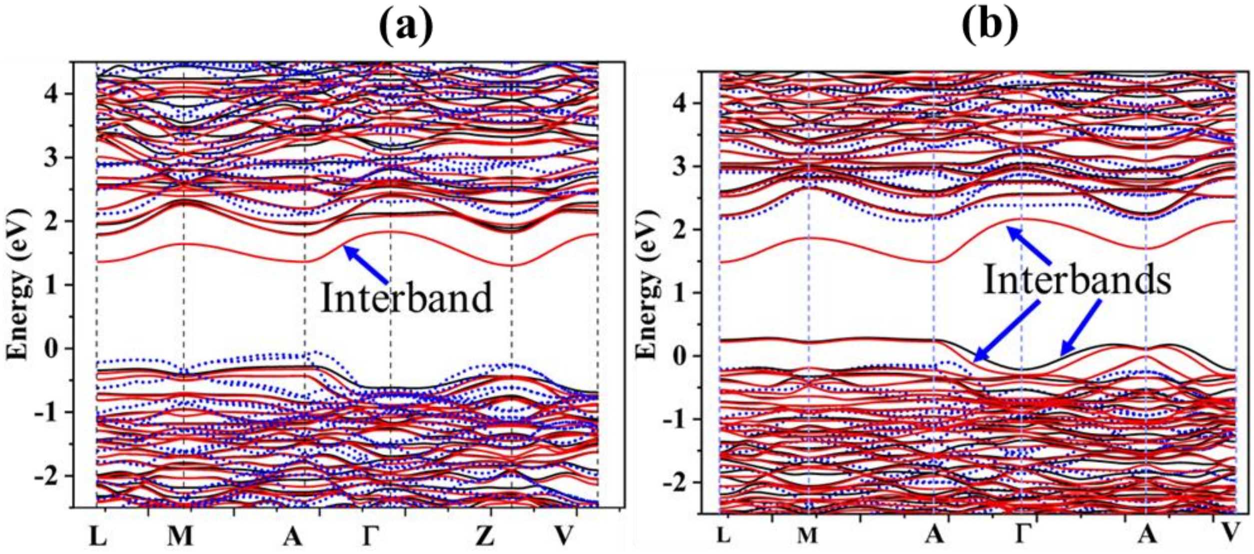

Figure 22 The spin-polarized electronic band structures of the pristine BiVO$_4$ (dots) (a) Li and (b) Na doped BiVO$_4$ with the spin up and down showing in red and black lines, respectively.

In addition, the absorption spectrum (imaginary part of dielectric function) was calculated from DFT. Figure 23a shows the simulated absorption spectrum (imaginary part of dielectric function) for the pristine and Li doped BiVO$_4$. As seen, both the pristine and Li doped BiVO$_4$ exhibited higher absorption > 2 eV. However, the Li:BiVO$_4$ showed an additional absorption peak ~ 1.2 eV, possibly due to a reduction in the band gap. This supports the experimental observation of increased absorption at extended lower energy regions due to Li doping (Figure 16b).

The simulated absorption spectrum for the pristine $BiVO_4$ and $Na:BiVO_4$ demonstrated an absorption onset ~2 eV, as shown in Figure 23b. Additional absorption was found for the $Na:BiVO_4$ in the form of the absorption peak at ~1 eV, which might be due to the multiple interbands formation and a small reduction in the bandgap. Similar enhanced absorption behavior was found through UV-vis measurements, as shown in Figure 16b. The site-projected density of states was evaluated for the pristine $BiVO_4$, $Na:BiVO_4$ and $Li:BiVO_4$. It was observed that oxygen atoms mostly contributed valance bands, and conduction bands were vastly by Bi and V atoms. The results obtained from the theoretical, experimental analysis and various characterizations confirmed that Li or Na doped $BiVO_4$ photoanode showed improved PEC performance due to the presence of multiple interbands, a slight reduction in the bandgap, increase in the electron-hole diffusion length and high charge transfer rate.

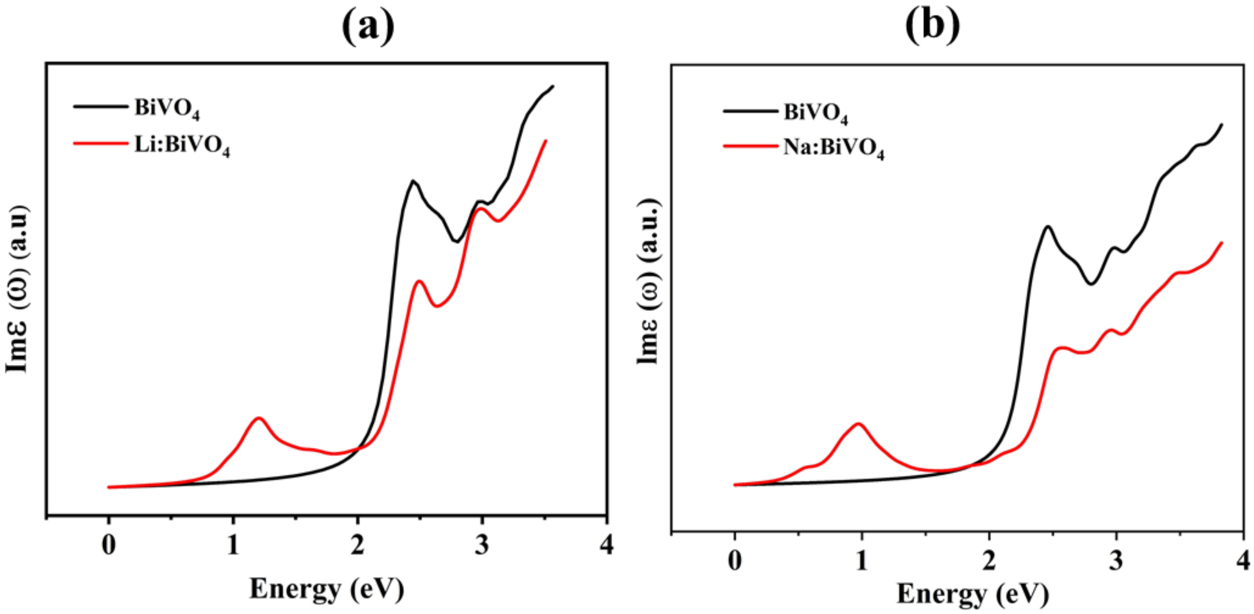

Figure 23 The DFT calculated absorption spectra for the pristine $BiVO_4$ along with (a) Li:$BiVO_4$ and (b) Na:$BiVO_4$.

3.7 XPS analysis

XPS analysis was carried out to determine the oxidation state of individual elements (Bi, V, K, Na and Li) in the pristine and doped $BiVO_4$ samples. The major peaks for Bi $4d_{5/2}$ (443.2 eV), Bi $4d_{3/2}$ (466.9 eV), V $2p_{3/2}$ (517.78 eV) and V $2p_{1/2}$ (525.28 eV) observed confirmed the oxidation state of Bi and V as +3 and +5, respectively in the pristine $BiVO_4$. Doped samples showed a slight decrease in the binding energies of Bi 4d and V 2p due to change in the local coordination environment of Bi^{3+} and V^{5+} ions[118]. It is also possible that the electron sphere around alkali metal in the interstitial void can exert electrostatic repulsive forces, reducing the Bi-O and V-O bond energy and increasing the unit cell volume, which also supported the observation in the XRD analysis (Figure 18). The binding energy corresponding to the individual doped alkali metal (K $2p_{3/2:}$ 294.08, K $2p_{1/2}$: 296.77, Na 1s: 1071.8 eV and Li 1s: 55.6 eV) confirmed the oxidation state +1. Figure 24 a-d showed the high-resolution XPS spectra in the O 1s region for all doped and pristine samples. As shown, the surface lattice oxygen (V-O), surface adsorbed oxygen (-OH) and alkali metal to oxygen interaction bond (M-O) was located at ~ 530.3, ~532 and ~529 eV, respectively. The area ratios of peaks V-O: −OH:M−O in pristine $BiVO_4$ and alkali metal-doped $BiVO_4$ were given in Figure 24 a-d. It was observed that the interaction due to the insertion of Li and Na in the interstitial position of $BiVO_4$ lattice was ~ 3 to 2 times compared to that with K due to the size difference. Further, the alkali metal doping concentration was validated from the peak fitting of each component (Bi, V, O, K, Na and Li).

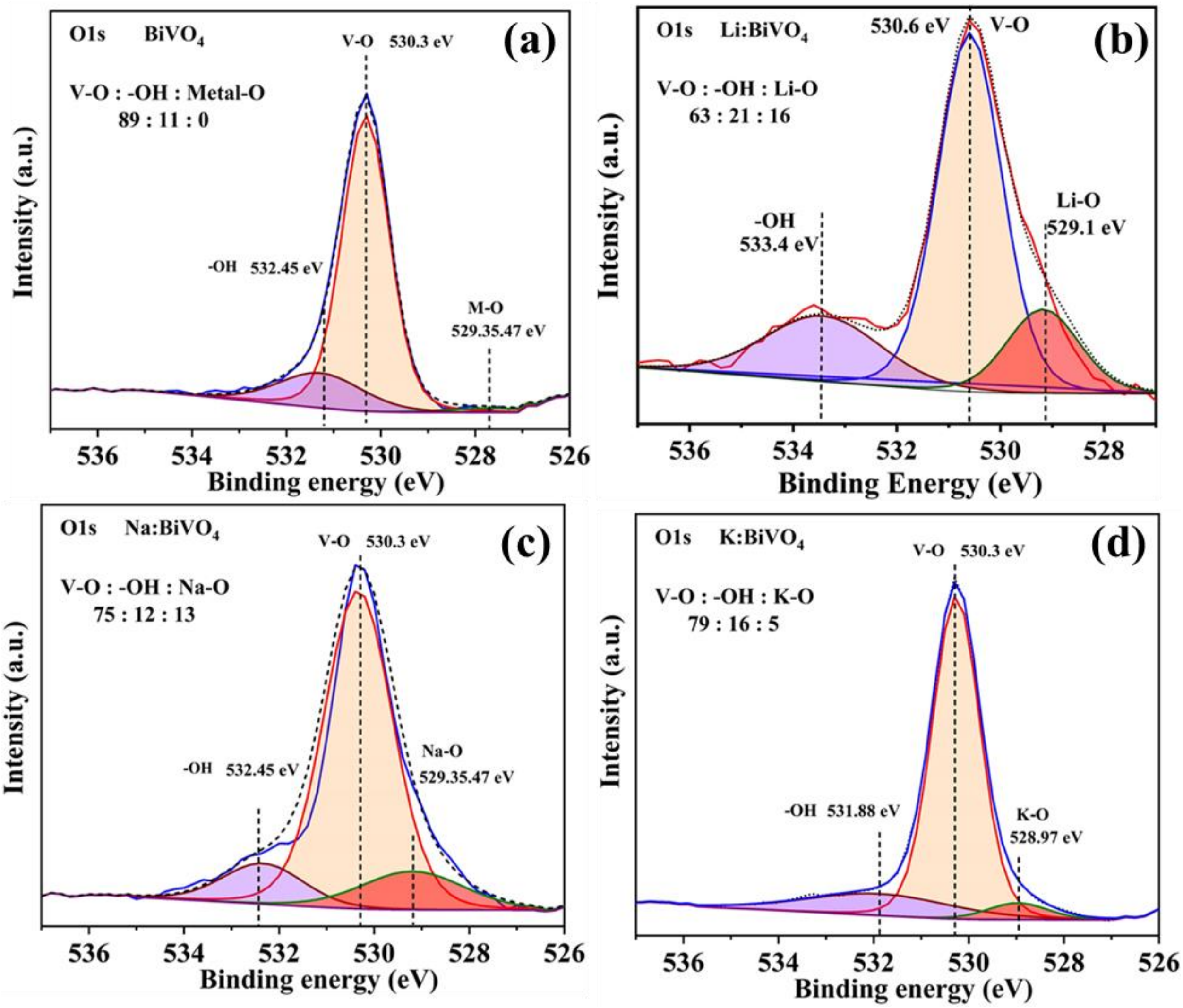

Figure 24 XPS spectra of fitted O1s peaks using Shirley background for (a) pristine BiVO$_4$, (b) Li:BiVO$_4$, (c) Na:BiVO$_4$ and (e) K:BiVO$_4$ films.

3.8 Doppler broadening spectroscopy

Figure 25 shows the *S-E* profile of FTO substrate, pristine and alkali metal-doped BiVO$_4$ samples. The solid lines through the data points explained the fitting of experimental *S-E* profiles using VEPFIT (details are provided in supplementary information). In the case of FTO substrate, *S*-parameter first decreased from surface to positron implantation energy ~ 7.5 keV, attributed to the back diffusion of implanted positrons because the back diffused positron annihilated through a state similar to positronium with a higher *S*-parameter. However, the fraction of back diffused electrons was reduced, leading to a decrease in *S*-parameter with the increase in implantation energy[119]. Beyond ~ 7.5 keV implantation energy, *S*-parameter continuously increased, attributed to the positron implantation to the glass portion of FTO. On the other hand, the *S*-*E* profiles for pristine and alkali metal-doped $BiVO_4$ films were different from the FTO and unique to each other. The observed decreasing trend of *S*-*E* profiles (Figure 28a) in all the films indicates no positronium formation occurred within the bulk of the films, which validated the crystallinity as confirmed by XRD (Figure 18). The changes observed in *S*-*E* profiles on Li, Na and K doping were due to modifications in the open volume defects such as vacancy or vacancy clusters. Interestingly, the *S*-parameter continuously increased when positrons were implanted at higher energies (> 15 keV). The diffusion length of the implanted positrons was given in Figure 28a (inset). For the pristine $BiVO_4$, the positron diffusion length was 9.65±0.92 nm, which was shorter than the bulk diffusion length in crystalline oxides[120]. The shorter diffusion length in $BiVO_4$ films confirmed the presence of negatively charged (cation vacancy) or neutral vacancy defects or vacancy clusters (Bi or V vacancy defects), which act as a potential trap for positrons. On the other hand, K doping demonstrated a decrease in characteristic *S*-parameter and a slight increase in the diffusion length (13.49±1.78 nm), indicating a small reduction in the defects density compared to pristine $BiVO_4$ films. On Na and Li doping, a significant increase (~ 4 times) in diffusion length

(54.19±5.6 and 63.51±6.4 nm) was observed along with a decrease in characteristic *S*-parameter value. It was dictated that Li and Na doping reduced Bi or V based vacancy defects in the film. In order to investigate the type of defects in these films, *S*-*W* correlation plots (Figure 25b) showed that the data points of all the three films follow a single trend indicating that the type of defects was similar in all three samples. However, their number density and chemical surrounding were modified due to the presence of alkali metal. The Bi and V based defects density in the bulk of the film was minimum in the Na:$BiVO_4$ and Li:$BiVO_4$ sample.

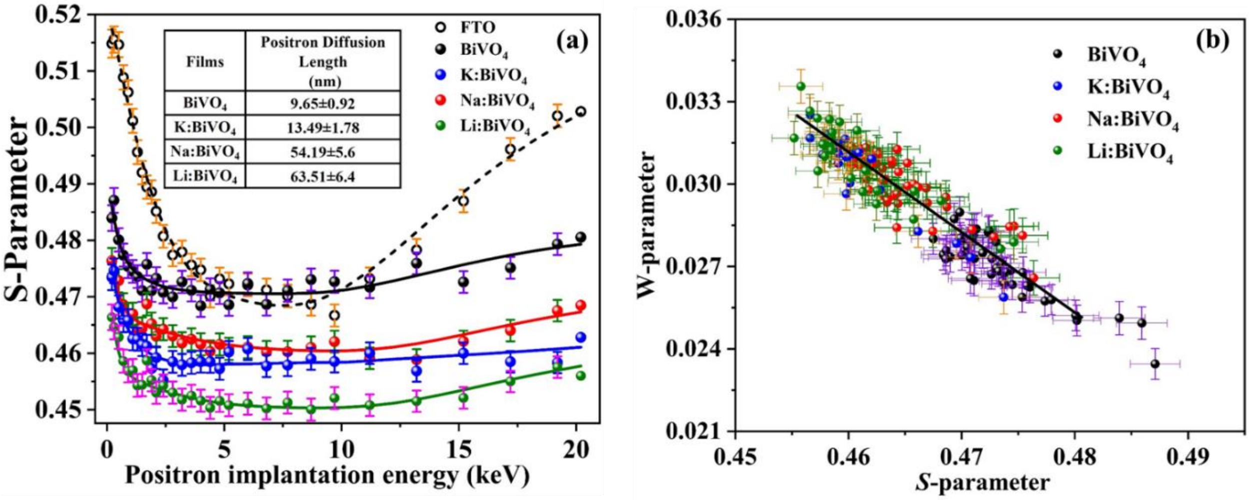

Figure 25 Doppler broadening spectroscopy measurements (a) S−E profiles; and (b) S−W correlation plots for substrate, pristine $BiVO_4$, K:$BiVO_4$, Na:$BiVO_4$ and Li:$BiVO_4$ films.

3.9 Conclusion

The alkali metal-doped $BiVO_4$ thin-film based photoanodes were prepared by ultrasonic spray coating technique and the planner structure with porous grains was confirmed by SEM analysis. The IPCE measurements confirmed the extended light absorption by

Li:$BiVO_4$ and Na:$BiVO_4$ compared to K:$BiVO_4$ and pristine $BiVO_4$. The XRD and Raman results indicated that alkali metal occupied the interstitial position of the $BiVO_4$ lattice structure. The diffusion length of charge particles was measured by implementing a positron at the surface of the thin films and found that the diffusion length of the positron increased by ~ 4 times in Na:$BiVO_4$ and Li:$BiVO_4$ compared to that of the pristine. It was also observed that the Bi and V based defect density was minimum on alkali metal doping in $BiVO_4$. The *ab initio* DFT calculations confirmed that the Li and Na doping in the BiVO4 interstitial site was energetically the most favorable position. It was evident that oxygen atoms formed weak bonds with Li and Na atoms, and an interband and multiple internbands formed between conduction and valence band, leading to a small reduction in the bandgap for Na:$BiVO_4$ and Li:$BiVO_4$.

4. CHAPTER 4 SITE DOPING/CO-DOING IN BIVO$_4$ WITH JUNCTIONS FORMATION

4.1 Introduction

Doping with metals is one of the promising approaches for improving the intrinsic properties of BiVO$_4$[74]. There are several studies on systematic doping of Tungsten (W) (approximately 0-4 wt. %) in the BiVO$_4$ system and correlating its PEC performance with respect to defect generation[75–79]. Pattengale *et al.* [121] has reported doping of 1.8 % W in BiVO$_4$ for improving PEC performance by 8-10 times compared to its undoped counterpart due to the formation of less distorted local structure at Bi's center, which favorably extends the electron lifetime by dramatically altering the nature of the recombination sites. Cho *et al.* [122] reported that incorporating W in BiVO$_4$ induced crystal deformation of its lattice, which leads to a 10 times improvement in water oxidation compared to its undoped counterpart. Shi et al. [77] have investigated the role of surface states (SS) in W-doped BiVO$_4$ photoanodes for PEC water splitting and found the optimum W-doping level of 2 % to suppress SS, which act as electron-hole pair recombination sites, leading to a significant 10-12 times photocurrent increase with respect to the pristine BiVO$_4$ at 1.23 V vs RHE.

4.2 Stoichiometric and non-stoichiometric doping of W in BiVO$_4$

Thus far, in the reported literature, W-doping was gradually increasing out to obtain $BiV_{1-x}W_xO_4$ which increases the number of charge carriers (N) by substituting W at V sites [77,123,124] and, thus, promoting bulk and interfacial charge separation, improving surface morphology, minimizing charge-trapping sites, increasing charge diffusion length, decreasing space charge region width, and suitably modifying Fermi level [78,79,122,124,125]. However, It is necessary to optimize the doping level as well as the composition of $BiVO_4$ to avoid the generation of defect sites such as Bi and O vacancies which can act as recombination sites [126,127]. Krol [128] has shown some issues with substituting W^{6+} for V^{5+} atoms in doped $BiV_{1-x}W_xO_4$ composition. In one scenario, Bi vacancies are formed to compensate extra charge from W6+ and preserve lattice site stoichiometry. This can lead to a decrease in the conductivity of W-doped n-type $BiVO_4$. In another scenario, the lattice site stoichiometry is preserved by the segregation of vanadium out of the $BiVO_4$ in the form of V_2O_5. This avoids the need for highly charged cation vacancies, and the W-dopant is now indeed charge-compensated by the desired free electrons. It should be realized that both these scenarios are unfavorable from an energetic point of view. A highly charged defect must be formed in one case, while in the other case, a second phase must segregate out. This leads to an important general observation for ternary – and more complex – metal oxides; doping these materials by simply dissolving a binary oxide is difficult to achieve in practice. An elegant solution for this can be to co-dope the $BiVO_4$ with excess amounts of W and Bi, so that Bi and W together can balance V charge deficiency. This is a well-known procedure to increase the solubility of binary oxides in ternary oxides in order to incorporate donor- or acceptor-type dopants[80].

To explore the optimum performance of $BiVO_4$, it is essential to perform a systematic study of the influence of stoichiometric and nonstoichiometric doping on the electronic structure and carrier dynamics of $BiVO_4$. The objective of present study was to synthesize stoichiometric and nonstoichiometric composition of W-doped $BiVO_4$ (i.e. $Bi_{1-(x+\delta)}V_{1-x}W_{x+\delta}O_4$; $BiV_{1-x}W_{x+\delta}O_4$ and $BiV_{1-y}W_yO_4$; $x = 0.008$; $y = 0.03$ and $\delta = 0.005$) using facile dip-coating technique and to understand its effect on PEC water oxidation behavior.

The PEC performances of the pristine and W-doped $BiVO_4$ photoanodes evaluated using linear sweep voltammetry under chopped light illumination on the front side of the electrodes without and with hole scavenger in 0.1M K_2HPO_4 electrolyte are given in Figure 26. It is evident from the plot that PEC performance for the stoichiometric composition of Bi, V and W (sample 2; $Bi_{1-(x+\delta)}V_{1-x}W_{x+\delta}O_4$; charge balance: 0) and non-stoichiometric compositions (sample 3; $BiV_{1-y}W_yO_4$; charge balance: 0.03; Bi atom in excess and sample 4; $BiV_{1-x}W_{x+\delta}O_4$; charge balance: 0.038; Bi and W atom in excess) electrodes are better than pristine $BiVO_4$ (sample 1). The PEC performance in increasing order were as follows: samples 1 < 2 < 3 < 4. Further, the non-stoichiometrically doped W in $BiVO_4$ for the co-doping.

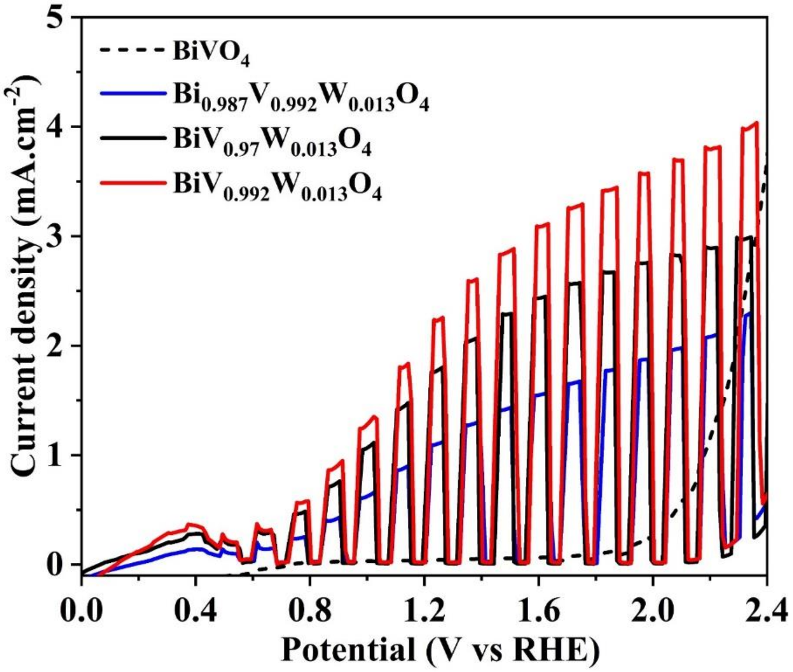

Figure 26 Linear sweep voltammetry for all samples under 1 sun illuminations in K_2HPO_4 electrolyte.

4.3 Rare earth metal doping at Bi site and coding with W in $BiVO_4$

There are several successful cases of doping at the V^{5+} site in $BiVO_4$[129,130]. However, few attempts were made to simultaneously doping at the vanadium and bismuth sites (Bi^{3+}). In an attempt, Jo *et* al. [131] enhanced water splitting performance through dual doping of In^{3+} and Mo^{6+} in $BiVO_4$. The mixed-phase (monoclinic and tetragonal) $BiVO_4$ showed a negative conduction band shift and led to PEC improvement compared to pristine BiVO4, but no significant improvement in light absorption was observed. Xin *et al.* [132] attempted to co-doped W, Ti in $BiVO_4$ and achieved nominal PCD ~1.6 $mA.cm^{-2}$ with hole scavengers due to limited enhancement in hole mobility and charge separation. In another attempt, Zhengbo et al. [133] co-doped Fe, W in $BiVO_4$ and additionally loaded metal-organic framework (MOF) to gain better charge carrier separation and stability of photoanode. The individual Fe and W doping in $BiVO_4$ showed poor PCD, and even dual doping of Fe, W in $BiVO_4$, and MOF loading could not significantly improve the PEC performance (1.6 mA.cm^{-2} at 1.23 V vs RHE). There are not many reports which show the systematic study of co-doping in $BiVO_4$ for PEC application. However, most of them used co-doping, specifically using rare earth metals for photo-catalytically degradation of organic waste by utilizing its only extended light absorption property[134,135]. The rare earth metal co-doping enhances light absorption, but it may lead to decreased charge transport property due to the possibility of charge recombination defect center formation in film and severely affecting PEC performance[104].

In the present study, we have systematically investigated the role of doping/co-doping of W and rare earth metals Er, Yb and Y in $BiVO_4$ with respect to their light absorption, bulk and surface charge separation and transfer properties. The individual element doping with W was chosen in the current study because it is doping significantly enhances the charge transport property[81]. Whereas individual elements Er, Yb and Y were chosen in the current study because of their extended light absorption, leading to high absorption efficiency[82,83]. The charge separation/transfer and light absorption efficiency estimation revealed that W:$BiVO_4$ photoanode showed the best PEC performance due to its higher charge separation/transfer efficiencies. Whereas (Y,W):$BiVO_4$ and (Yb,W):$BiVO_4$ photoanodes showed improved PEC performance than pristine $BiVO_4$ due to extended light absorption characteristics ($\lambda \leq 550$) and overall bandgap reduction on Er^{3+}, Yb^{3+} or Y^{3+} doping.

4.4 Light absorbance and photoelectrochemical measurements

In order to understand such water splitting performance, the light absorption behavior of photoanodes was evaluated. From Figure 27, it was observed that the light absorption onset extended from ~510 to ~550 nm with Yb^{3+} Er^{3+} and Y^{3+} doping in $BiVO_4$ in comparison to pristine $BiVO_4$. This phenomenon was observed even in the case of co-doped (Yb,W):$BiVO_4$, (Li,W):$BiVO_4$ and (Y,W):$BiVO_4$ photoanodes. The observed redshift in the absorption region with Yb^{3+}, Er^{3+} and Y^{3+} doping have been well reported in the literature, and it may occur due to intrinsic electron transition between O and Yb or Y orbitals[83,82]. It was observed that with Er doping in $BiVO_4$, the absorbance range widened from visible to NIR region i.e. wavelength region from 400-614 nm (Figure 27). Absorption for $BiVO_4$ is started from a lower wavelength ~535 nm, even after W doping the absorption didn't improve significantly. However, on the addition of Er, absorption enhanced significantly for Er:$BiVO_4$ and (Er,W):$BiVO_4$ electrode due to additional absorption in ~535 to ~680 nm light spectrum region. In absorption spectra at ~554 and ~675 nm, two minor bands were identified in Er^{3+} doped electrodes. This could be assigned to the transitions from the ground state $^4I_{15/2}$ to excited states $^4H_{11/2}$ (~554 nm) and $^4F_{9/2}$ (~675 nm) of Er^{3+}, respectively[136,137]. At the same time, no substantial change in absorption onset was observed with W^{6+} doping in $BiVO_4$[104]. The estimated absorption efficiency (η_{abs}: Figure 27: inset) from light-harvesting efficiency (LHE)showed that (Y,W):$BiVO_4$, (Er,W):$BiVO_4$ photoanode attained absorption efficiency 77 ± 4 and 74 ± 3% in comparison to 63 ± 3 and 62 ± 3 % (Figure 27 inset) of W doped and pristine $BiVO_4$, respectively. The pristine and W doped $BiVO_4$ samples have shown a similar optical band ~2.52 eV. Yb and Y doped/co-doped BiVO4 samples have shown decreased optical band, i.e. 2.37 and 2.29 eV, respectively, due to redshift in the absorption[83,82]. Corresponding band gap calculation for Er-doped shows that Er:BiVO$_4$ electrode has minimum ~2.37eV bandgap. The absorbance measurement confirmed that Er, Y, Yb doping enhances light absorption efficiency, whereas W doping does not significantly affect the absorption efficiency of BiVO$_4$ photoanode.

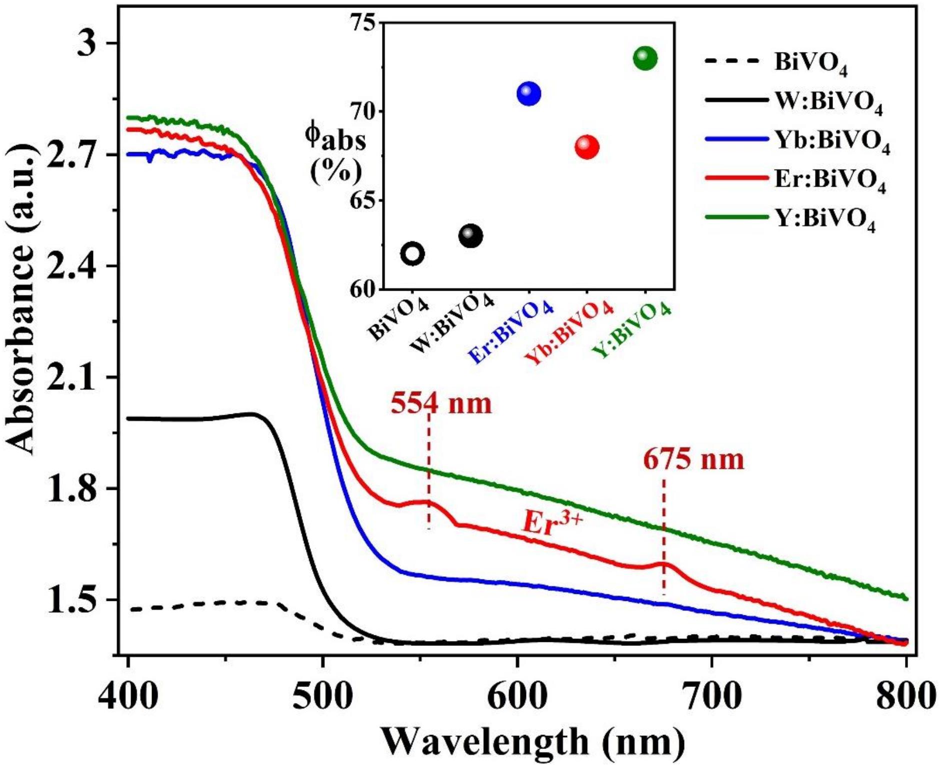

Figure 27 UV-vis absorption spectra for site doping samples

The water-splitting property of Er, Y, Yb, W individual and co-doped BiVO$_4$ photoanodes was evaluated for PEC performance (Figure 28). It was observed from Figure 28 that with individual Er, Yb, Y and W doping in BiVO$_4$, the PCD improved 2, 3, 4 and 23 times corresponding to the pristine BiVO$_4$. The significant increase in PCD of W:BiVO$_4$

compared to Er:$BiVO_4$,Yb:$BiVO_4$ or Y:$BiVO_4$ photoanodes are attributed to better bulk charge pair separation and transfer[138]. Considering better PEC performance of the W:$BiVO_4$ photoanode, $BiVO_4$ was co-doped as (Er,W), (Yb,W) and (Y,W) to enhance the performance of individual Er, Yb and Y doped $BiVO_4$ photoanodes. The (Er,W):$BiVO_4$, (Yb,W):$BiVO_4$ and (Y,W):$BiVO_4$ photoanodes demonstrate obvious increment over Er:$BiVO_4$, Yb:$BiVO_4$ or Y:$BiVO_4$ photoanodes by achieving PCD 1.58± 0.08, 1.29 ± 0.06 and 1.94 ± 0.1 mA.cm^{-2} (Figure 28) respectively, but it could not perform better than W:$BiVO_4$ photoanode (2.2 ± 0.13 mA.cm^{-2}). One possible reason for the lower PEC performance could be because even though there is high charge separation in bulk on W doping, the defect is generated in bulk and at the surface with substitutional doping of Er^{3+}, Yb^{3+}, Y^{3+} at Bi^{3+} sites could act as a recombination center.

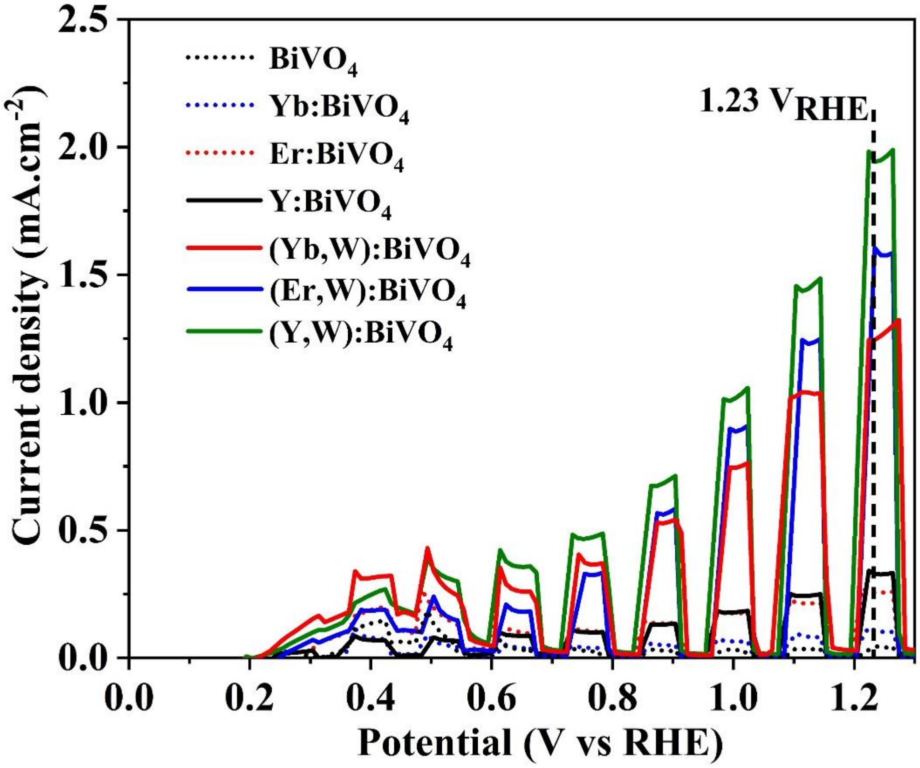

Figure 28 Linear sweep voltammetry for of sites doped and co-doped samples under 1 sun illuminations in K_2HPO_4 electrolyte.

The effect of catalysts aided in the negative shift of the onset potential which was observed in the PCD behavior. This negative shift in the onset potential confirms the conduction band shift, leading to high charge transfer efficiency and minimizing the recombination to increase water splitting performance. The Mott Schottky analysis also confirmed the negative shift in the onset potential. Where, negative shift for Yb:$BiVO_4$, Er:$BiVO_4$ and Y:$BiVO_4$ photoanodes are 98, 118 and 153 mV, respectively, compared to pristine $BiVO_4$. The relative shift in conduction band position was calculated from the Mott-Schottky. As a result, photoanodes are close to the water reduction potential of 0 V vs RHE, making the water-splitting process more facile.

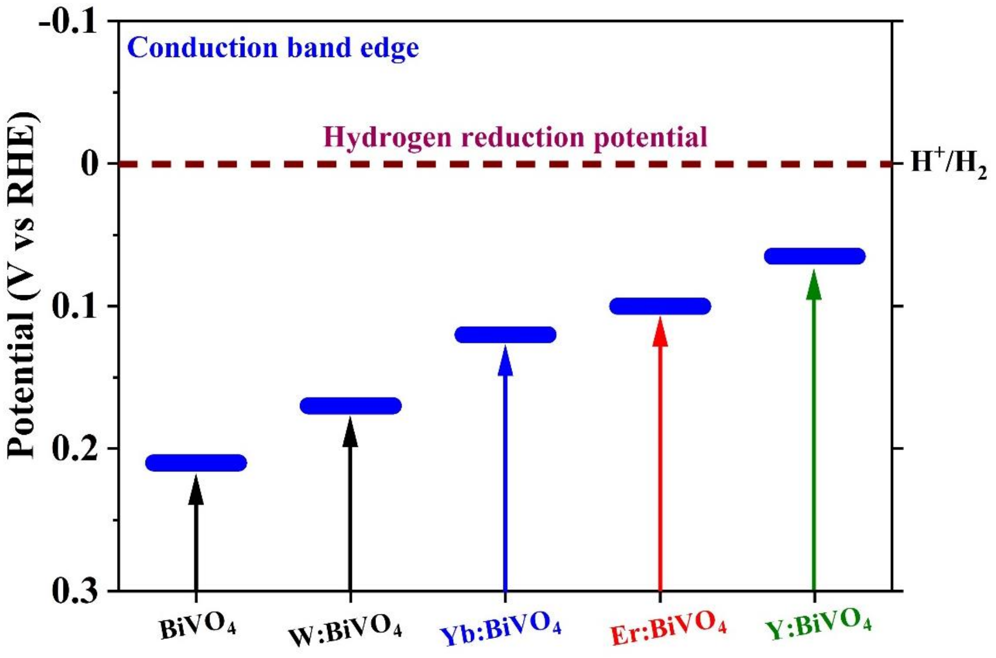

Figure 29 Shift in the conduction band edge of site doped and co-doped samples.

To support above argument on the bulk charge separation and surface transfer efficiencies, corresponding bulk and surface resistance of doped/co-doped photoanodes were investigated using the Electrochemical impedance (EIS) method. As shown in Figure 4a, pristine $BiVO_4$ demonstrates maximum impedance, which elucidates the poor water oxidation kinetics of pristine $BiVO_4$. Whereas $W:BiVO_4$ photoanode demonstrates minimum impedance, indicating that better charge separation with surface transfer leads to better water oxidation kinetics. Randles circuit (Figure B4a) contains multiple elements such as external contact, bulk and surface resistance and capacitance connected with the Helmholtz layer at photoanode and electrolyte interface. The estimated resistance and capacitance of photoanodes are shown in Figure 4b. The film bulk resistance (R_b) gradually decreases with Er, Y or Yb doping and significantly decreases with W doping. The co-doping of Er, Yb or Y with W in $BiVO_4$ increases the bulk resistance concerning $W:BiVO_4$

photoanode. The capacitance in bulk (C_b) was comparatively lower for W:$BiVO_4$ and (Y,W):$BiVO_4$ photoanode, which denotes that charge accumulation is less in the bulk of the film, i.e. getting separated and transported easily. It validates the achieved charge separation efficiency trend in Figure S3c. Additionally, surface charge transfer resistance (R_S) followed following decreasing trend: $BiVO_4$ > Yb:$BiVO_4$ > Er:$BiVO_4$ > Y:$BiVO_4$ > (Yb,W):$BiVO_4$ > (Yb,W):$BiVO_4$ > (Er,W):$BiVO_4$ > (Y,W):$BiVO_4$ > W:$BiVO_4$. The W:$BiVO_4$ photoanode showed minimum surface resistance, and again, co-doping with Er, Yb or Y led to an increase in the surface resistance. The surface capacitance (C_s) is maximum on W doped photoanode, illustrating that charges are accumulated on the film surface and available for the water oxidation process. It validates the achieved charge transfer efficiency trend in Figure B3d than pristine $BiVO_4$.

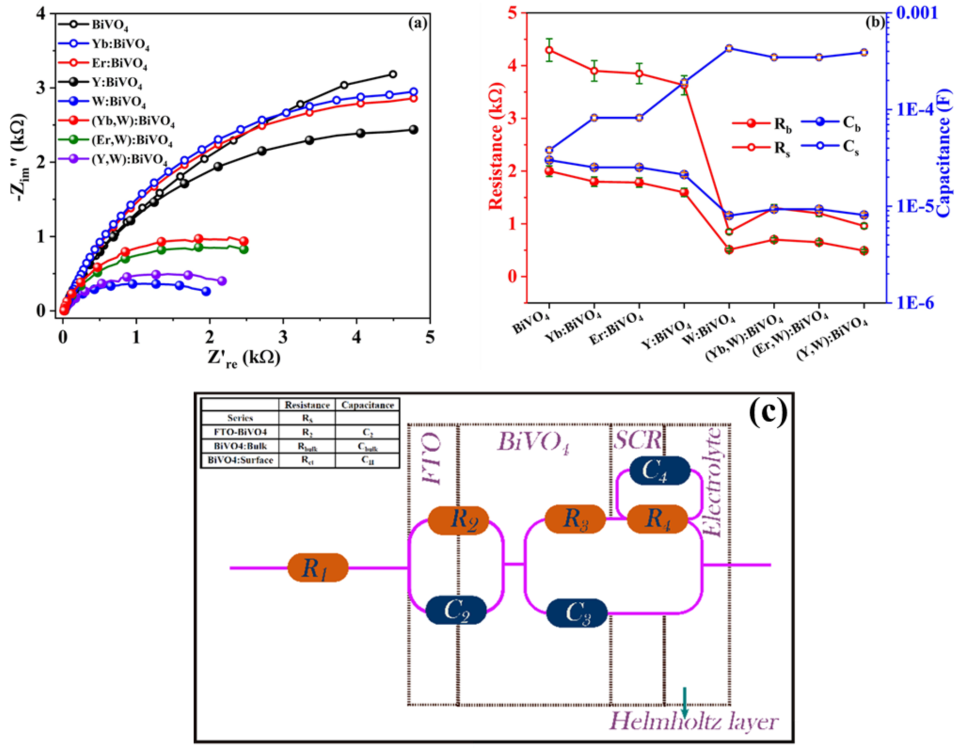

	Resistance	Capacitance
Series	R_s	
FTO-BiVO4	R_2	C_2
BiVO4:Bulk	R_{bulk}	C_{bulk}
BiVO4:Surface	R_{ct}	C_{H}

Figure 30 (a) Electrochemical impedance spectra (EIS) plot of pristine $BiVO_4$, Yb:$BiVO_4$, Er:$BiVO_4$, Y:$BiVO_4$, W:$BiVO_4$, (Yb,W): $BiVO_4$, (Er,W): $BiVO_4$ and (Y,W):$BiVO_4$ photoanodes measured at 1.23 V vs RHE. (b) Resistance and capacitance plot at bulk and surface (R_b, R_s, C_b and C_s). (c) Randle circuit for the resistance and capacitance calculation in bulk and surface.

In order to understand the recombination center or reaction sites at the photoanode surface and electrolyte interface, CV measurement was performed in K_2HPO_4 electrolyte from potential 0.45 to 2.5 V vs RHE in the dark (Figure 3c). The observed cathodic peak at ~1.45 V vs RHE describes the surface reaction given in eq 14[77].

$$\mathrm{VO_2}^{+}\ (surface) + 2H^{+}\ (aq) + e^{-}_{inject} \rightarrow \mathrm{V}O^{2+}\ (surface) + H_2 \qquad (14)$$

Surface reaction VO_2^+/VO^{2+} is irreversible direct that charge transfer from trap sites (termed as a surface state) and detrapping process is slow which lead to accumulation of charges in the trap sites and then increases recombination (eq 15)[104].

$$\mathrm{VO_2}^{+}\ (surface) + 2H^{+}\ (aq)\ \ \overset{(e^{-}_{photo} + h_{trap})_{recombination}}{\longleftrightarrow}\ \ VO^{2+}\ (surface)$$

(15)

Since the peak potential is greater than the water oxidation potential (1.23 V vs RHE), the potential range for this state extends over the water oxidation in the dark. W:$BiVO_4$ photoanodes show a smaller peak intensity than other photoanodes, which depicts the low number of trap site formations, leading to higher PEC performance. The peak intensity (estimated by peak ~1.45 V vs RHE fitting using Matlab software) decreasing sequence is as follows: W:$BiVO_4$ > (Y,W):$BiVO_4$ > (Er,W):$BiVO_4$ > (Yb,W):$BiVO_4$ > Y:$BiVO_4$ > Er:$BiVO_4$ > Yb:$BiVO_4$ > $BiVO_4$.

The observed phenomena is explained by the formation of recombination centers on the electrode surface (surface states) with Er, Y/Yb doping along with W[77]. The SS has been reported to influence charge transfer at the semiconductor electrode/electrolyte interface because they can work as reaction sites and recombination centers on the electrode surface[139]. Doping of Er, Y and Yb enhanced light absorption efficiency (Figure 3b) better than W doped $BiVO_4$ sample. However, there are recombination centers on the BiVO4 photoanode surface (surface states) with Er, Y& Yb doping, and it remains even along with W co-doping. As given in above supporting Figure 3c, the SS has been reported to influence charge transfer at the semiconductor electrode/electrolyte interface because they can work as reaction sites and/or recombination centers on the photoanode surface. The irreversible peak (VO_2^+/VO^{2+} at ~ 1.45 V vs RHE, Figure 3c) intensity values follow the order: (Yb,W):$BiVO_4$ > (Er,W):$BiVO_4$ > (Y,W):$BiVO_4$ > W:$BiVO_4$, indicating formation of large number of recombination sites for the (Yb,W):$BiVO_4$, (Er,W):$BiVO_4$ and (Y,W):$BiVO_4$ photoanodes. This is a direct evidence for the PCD with the following order: (Yb,W):$BiVO_4$ < (Er,W):$BiVO_4$ < (Y,W):$BiVO_4$ < W:$BiVO_4$.

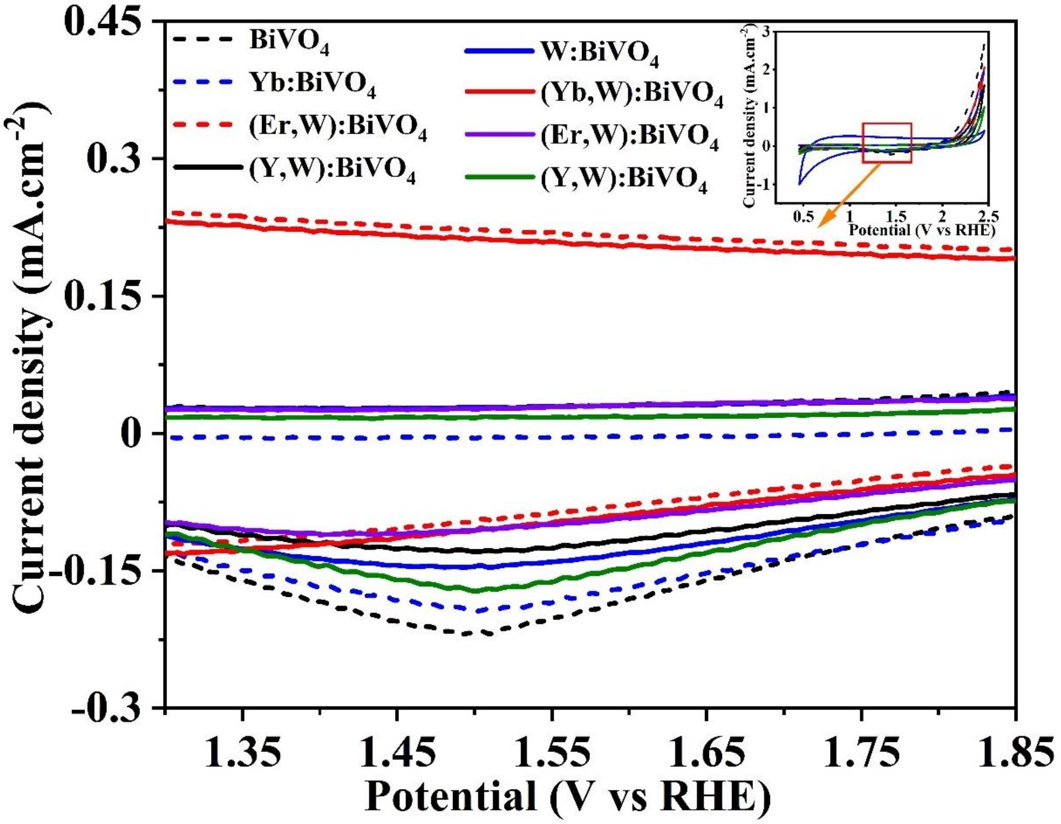

Figure 31 Cyclic voltammetry in dark at 20 mV/sec in 0.1 M K_2HPO_4.

4.5 Type II heterojunction formation along with p-n junction

In $BiVO_4$, type-II heterojunction with WO_3 is most suitable due to the more negative potential of the conduction band and valence band of $BiVO_4$, which mediate for the efficient electron transfer from $BiVO_4$ to FTO film[140,141]. Lee *et al.* [141] have reported the most successful case of type-II heterojunction formation with a conformal coating of one-dimensional WO_3 nanorod and $BiVO_4$ by pulse electrodeposition and achieved impressive PCD (~ 4.55 mA.cm^{-2}) at 1.23 V vs RHE. Along with the formation of type-II heterojunction with WO_3, Based on the above study, best-performing photoanodes (Er:W):$BiVO_4$, (Yb,W):$BiVO_4$ and (Y,W):$BiVO_4$ was selected for improving their charge transfer kinetics between film and FTO by forming type-II heterojunction (minimizing the formation of any recombination sites) with WO_3. In the FTO/WO_3/$BiVO_4$ heterojunction arrangement, the WO_3 interface layer act as an electron acceptor and participates in electron transportation to the charge collector FTO side. On the other hand, $BiVO_4$ layer act as a hole acceptor and participates in transferring holes from bulk to the film surface.

For WO_3 film formation, 3 mM ammonium tungstate (Sigma-Aldrich, CAS#10031513) was dissolved in 2M HNO_3 (Sigma-Aldrich, CAS#7803556). The precursor solution was sprayed over the FTO substrate (at 50 °C) using an ultrasonic spray coating tool. The film was annealed at 500 °C for 2 h to obtain thin adherent WO_3 film. To prepare WO_3/(Yb,W):$BiVO_4$ (composition $WO_3/Bi_{0.96}Yb_{0.04}V_{0.992}W_{0.013}O_4$), WO_3/(Er,W):$BiVO_4$ (composition $WO_3/Bi_{0.93}Er_{0.03}V_{0.992}W_{0.013}O_4$) and WO_3/(Y,W):$BiVO_4$ thin films (composition $WO_3/Bi_{0.96}Y_{0.04}\ V_{0.992}W_{0.013}O_4$) respective W:$BIVO_4$,(Er,W):$BiVO_4$ and (Y,W):$BiVO_4$ layer coated over WO_3. The fabrication process is shown in Figure 32.

p-n **junction formation**

p-n junction was formed with Fe:NiO (p-type) to further enhance the charge separation and transfer. Fe doped $Ni(OH)_2$ precipitate was prepared by the method reported in the litrature[142]. The Fe doped $Ni(OH)_2$ precipitate (0.01 gm) was dispersed in 10 ml of DI water, and this solution was sprayed over WO_3/(Y,W):$BiVO_4$ film to deposit ~ 6μg of Fe doped $Ni(OH)_2$. The catalyst coated film was annealed for 2 h at 300 °C to obtain a thin layer of Fe:NiO over WO_3/(Y,W):$BiVO_4$, WO_3/(Er,W):$BiVO_4$ film. For cobalt phosphate

(Co-Pi) was deposited using 0.1 M K_2HPO_4 (Sigma-Aldrich, CAS#7758114) and 0.5 mM $Co(NO_3)_2\cdot 6H_2O$ (Sigma-Aldrich, CAS#10026229) in DI water by applying 0.75 V vs SCE for 30 seconds to obtain final configuration of WO_3/(Er,W):$BiVO_4$/Fe:NiO/Co-Pi and WO_3/(Y,W):$BiVO_4$/Fe:NiO/Co-Pi. Figure 32 illustrate the detailed film formation process of WO_3/(Y,W):$BiVO_4$/Fe:NiO photoanode.

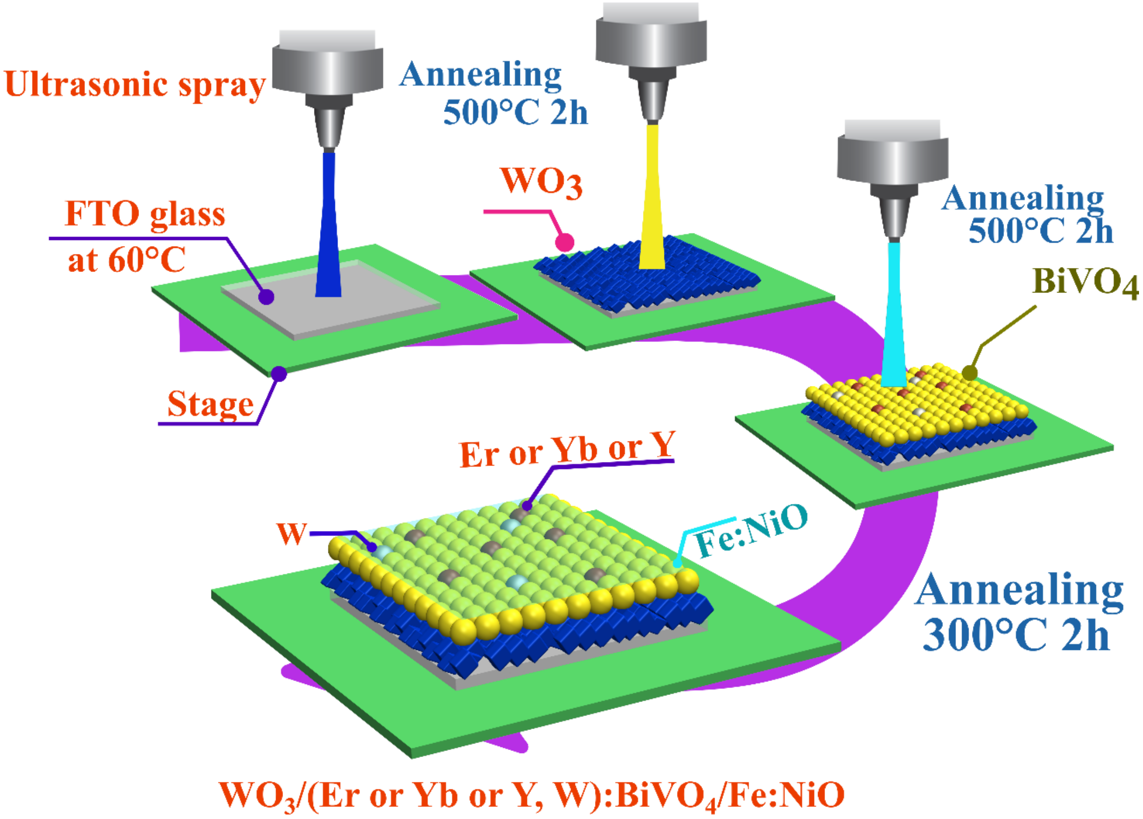

Figure 32 film fabrication process of WO_3/(Y,W):$BiVO_4$/Fe:NiO photoanodes

4.6 photocurrent density measurements

It is evident from Figure 33 that the WO_3/Yb:$BiVO_4$, WO_3/(Er,W):$BiVO_4$ and WO_3/(Y,W):$BiVO_4$ photoanodes showed a noticeable enhancement in water oxidation with maximum PCD 2.48 ± 0.12, 4.12± 0.22 and 4.32 ± 0.22 mA.cm^{-2} at 1.23V vs RHE exceeding the performance in comparison to their counter parts (Yb,W):$BiVO_4$, (Er,W):$BiVO_4$ and (Y,W):$BiVO_4$ photoanodes. This concludes that (Y,W):$BiVO_4$ and (Er,W):$BiVO_4$ have shown better water splitting performance compared to W:$BiVO_4$ after type-II heterojunction formation with WO_3 and the increment in PCD for (Er,W):$BiVO_4$ and (Y,W):$BiVO_4$ photoanode is much more pronounced at higher bias potential. The additional enhancement in the PCD performance of WO_3/(Y,W):$BiVO_4$ and WO_3/(Y,W):$BiVO_4$ photoanode is due to effectively utilizing individual properties of Er, Y and W in the co-doped sample.

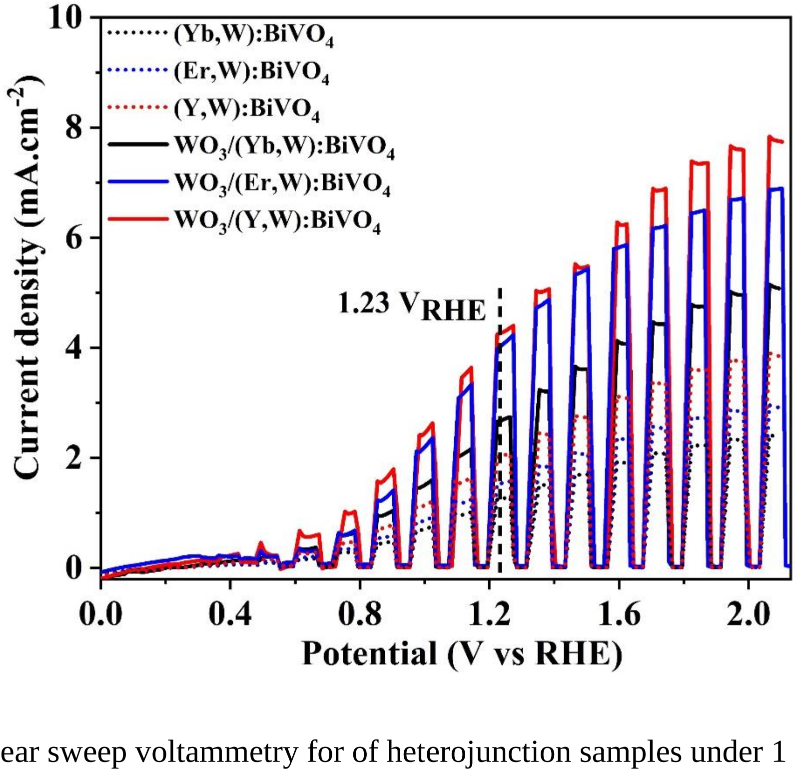

Figure 33 Linear sweep voltammetry for of heterojunction samples under 1 sun illuminations in K_2HPO_4 electrolyte.

It is evident from Figure 34 that the two best performing photoanodes WO_3/Y:$BiVO_4$ WO_3/(Er,W):$BiVO_4$ selected to study the p-n junction. It can be seen that WO_3/(Y,W):$BiVO_4$/Fe:NiO showed a noticeable enhancement in water oxidation with maximum PCD 5.2 ± 0.15 and 5.6± 0.25 $mA.cm^{-2}$ at 1.23V vs RHE exceeding the performance in comparison to their counter parts WO_3/(Y,W):$BiVO_4$ and WO_3/(Er,W):$BiVO_4$ photoanodes. Fe:NiO form p-n junction with the semiconducting $BiVO_4$ modifies bulk properties of the $BiVO_4$ film[143,144]. Fe:NiO (p-type semiconductor) with a light-absorbing range of 350 to 550 nm with an indirect band gap of 2.35 eV, forms p-n junction with $BiVO_4$[143]. Due to the p–n junction formed between the interface of WO_3/(Y,W):$BiVO_4$ and WO_3/(Er,W):$BiVO_4$ and Fe-NiO, an inner electric field is built, enhancing the surface reaction kinetics (transportation of electron-hole pairs), lowering the band bending conditions, and increasing the bulk charge separation. This leads to a reduction in bulk resistance and capacitance values[145].

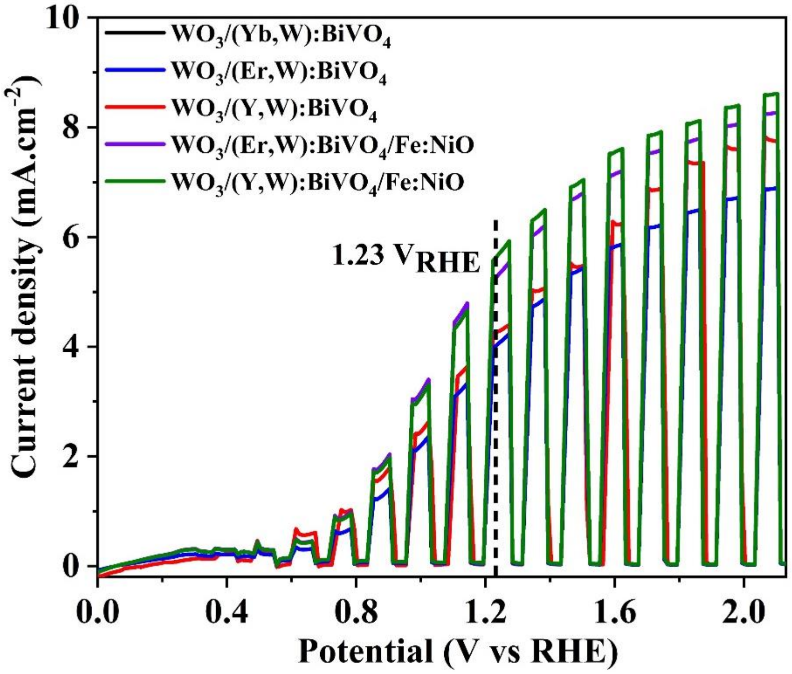

Figure 34 Linear sweep voltammetry for of heterojunction and p-n junction samples under 1 sun illuminations in K_2HPO_4 electrolyte.

4.7 Incident photon-to-current conversion efficiencies (IPCE) and absorbed photon-to-current conversion efficiency (APCE)

To quantify the total photon absorption concerning wavelength that undergoes to the photoactivity, the incident photon-to-current conversion efficiencies (IPCE) of the photoelectrode are measured at 1.23 V vs RHE (Figure 4a). The IPCE of pristine $BiVO_4$ photoanode demonstrates photoactivity from $\lambda \leq 510$. However, after co-doping with Er^{3+}, Y^{3+}, W^{6+}, the IPCE absorption range extended to $\lambda \leq 550$. The WO_3/(Yb,W):$BiVO_4$, WO_3/(Er,W):$BiVO_4$ and WO_3/(Y,W):$BiVO_4$ photoanodes showed maximum IPCE value 45 ± 2.15, 63 ± 2.5 and 73 ± 3 %, respectively. Whereas WO_3/(Er,W):$BiVO_4$ and WO_3/(Y,W):$BiVO_4$ photoanodes with OER catalyst showed remarkably high IPCE (73 and ~98 %). Along with IPCE, integrated photocurrents were calculated (Figure 4a) to validate the obtained current from LSV in Figure 35a for all photoanodes. The integrated photocurrent for various photoanodes showed PCD closed to the respective experimental PCD. The evaluated absorbed photon-to-current conversion efficiency (APCE) (Figure 35b) illustrates the photons absorbed at the film surface, participating in the water-splitting process. The WO_3/(Y,W):$BiVO_4$/Fe:NiO photoanode showed the highest APCE value (~95 % at 420 nm) along with WO_3/(Er,W):$BiVO_4$/Fe:NiO (82 ± 3.5 %). The APCE results confirmed that photoanode with heterojunction (Er,W) & (Y,W) and p-n junction could effectively utilize the absorbed light towards the PEC water splitting process.

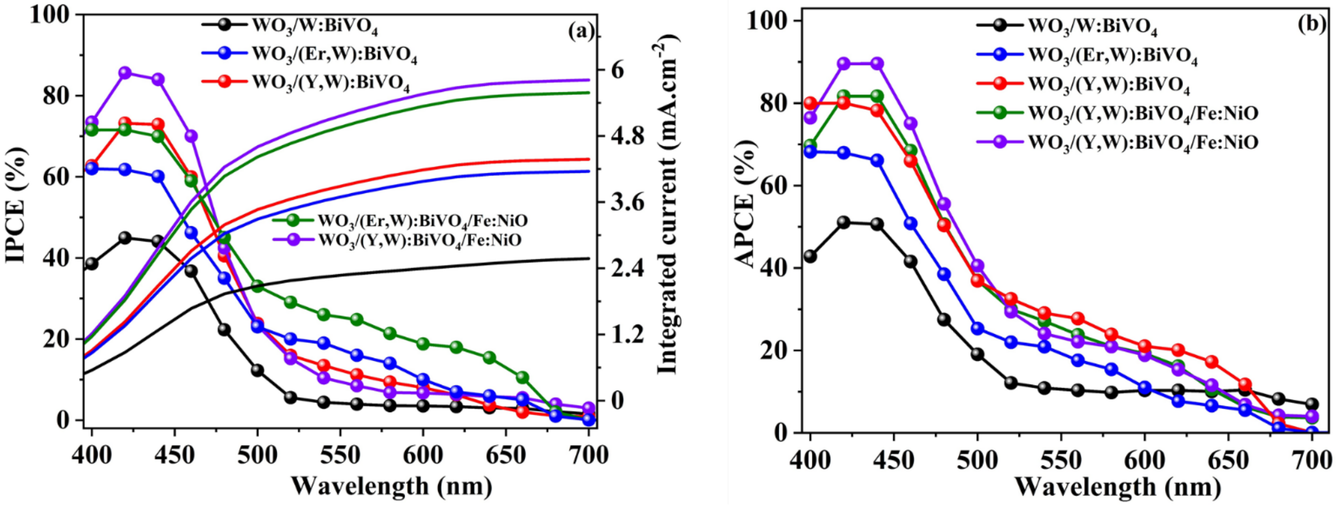

Figure 35 (a) Incident photon-to-current efficiency (IPCE), (b) absorbed photon-to-current efficiency (APCE) of for $WO_3/W:BiVO_4$, $WO_3/(Er,W):BiVO_4$, $WO_3/(Y,W):BiVO_4$, $WO_3/(Er,W):BiVO_4/Fe:NiO$, $WO_3/(Y,W):BiVO_4/Fe:NiO$ photoanodes at 1.23 V vs RHE in 0.1 M K_2HPO_4 electrolyte.

4.8 Band energy diagram for $WO_3/(Y,W):BiVO_4/Fe:NiO/Co-Pi$

Effective charge transfer through WO_3 and $(Y,W):BiVO_4$ heterojunction was crucial for higher PEC performance. Electrons and holes transfer process is illustrated in energy diagram Figure 36. On back-side illumination of photoanode, the first WO_3 layer absorbed mostly high energy photons $\lambda \leq 440$ nm and $(Y,W):BiVO_4$ layer absorbed photons $\lambda \leq 550$ nm. Due to relative energy band configuration, photogenerated holes at WO_3 will transport and be collected at $(Y,W):BiVO_4$ and simultaneously photogenerated electrons will move to WO_3 and then charge collector (FTO layer). This process will separate electrons and holes more efficiently. In addition, there will be systematic band bending at the interface of WO_3 and $(Y,W):BiVO_4$ layers. The band bending plays a crucial role in charge separation i.e. higher band bending can lead to better charge separation. The band bending phenomenon in our experiment was confirmed by the negative shift observed in the onset potential. Due to the band bending, there will be barrier formation (35.34 ± 1.8 ~ 60 ± 0.3 mV) between (Y,W):$BiVO_4$ and WO_3 layers. The electrons with average thermal energy (~k_BT) can easily overcome this barrier during PEC water oxidation process[58]. In order to confirm the improved charge transport due to band bending, open circuit potential (ΔOCP) was measured for all photoanodes[58]. It is reported that under 1 sun illumination, sufficiently high charge carriers are generated and lead to flattening the energy bands. A similar band bending explanation can be given for WO_3/(Er,W):$BiVO_4$/Fe:NiO/Co-Pi. The flattening of the energy band is mostly affected by built-in potential and recombination of charge carriers. The ΔOCP values gradually increase. Since the built-in potential is the same for all photoanodes, the increase in ΔOCP indicate lesser charge recombination in the film. The WO_3/(Y,W):$BiVO_4$/Fe:NiO/Co-Pi photoanode showed the highest drop in the potential that relate to the lowest charge recombination. Space charge width (SCL) or depletion layer was calculated to confirm the conclusion drawn from ΔOCP measurement. It was observed that for the WO_3/(Y,W):$BiVO_4$, WO_3/(Er,W):$BiVO_4$/Fe:NiO/Co-Pi and WO_3/(Y,W):$BiVO_4$/Fe:NiO/Co-Pi photoanodes, the SCL got widen with increasing anodic bias potential which illustrate that maximum minority carriers i.e. holes are transported to the reactive interface for water splitting process.

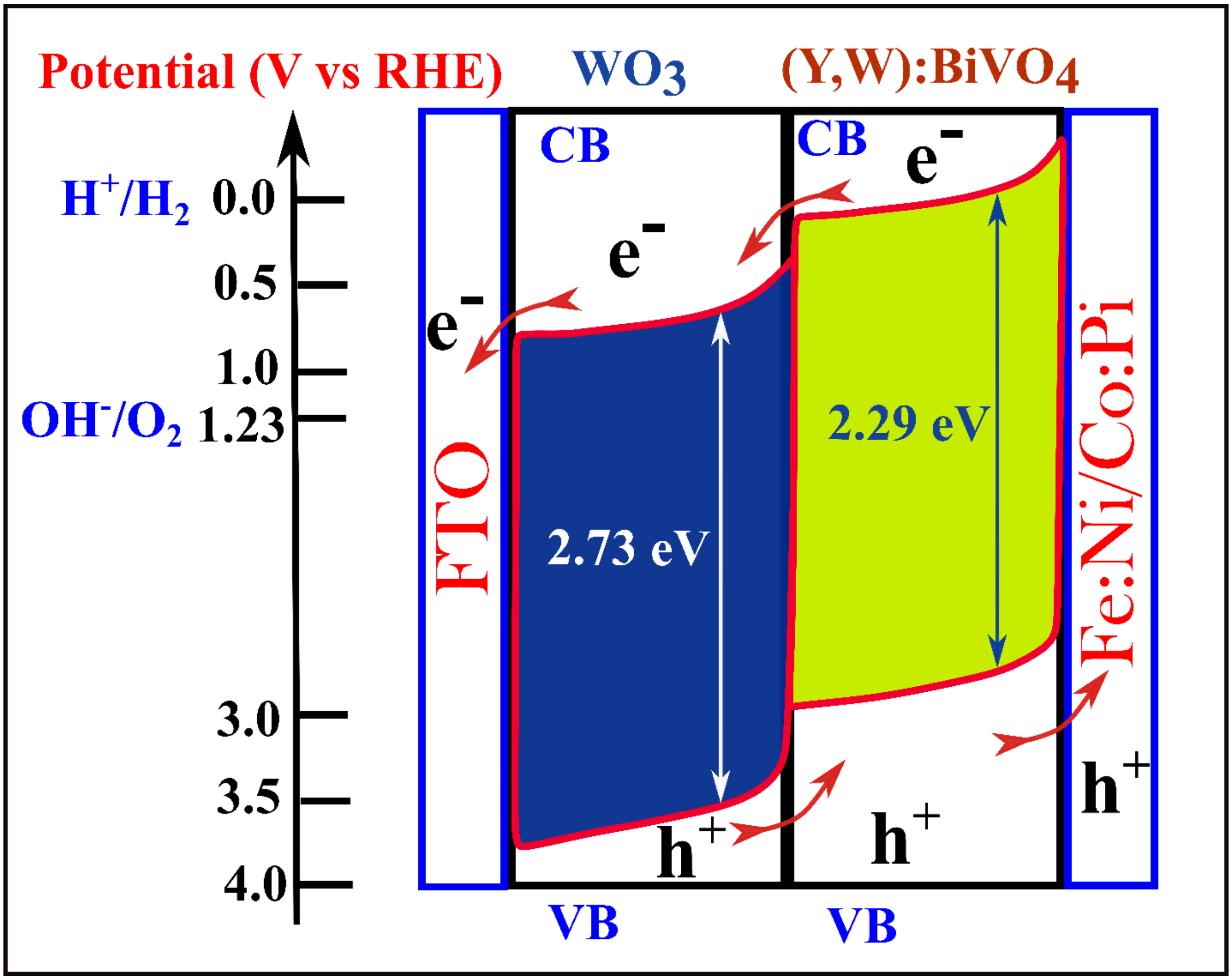

Figure 36 Figure 5. Energy diagram illustrating electron transfer in (a) WO_3/(Y,W):$BiVO_4$/Fe:NiO/Co-Pi.

4.9 Cyclic stability measurements

The cyclic stability measurement (Figure 37) of the WO_3/(Y,W):$BiVO_4$/Fe:NiOi photoanode was conducted for water oxidation at 1.23 V vs RHE by keeping light ON 11 h and OFF for 2 h. It was observed that WO_3/(Y,W):$BiVO_4$/Fe:NiO/Co-Pi photoanode can retain ~95 % of the PCD even after 33 hrs of operation. In present WO_3/(Y,W):$BiVO_4$/Fe:NiO/Co-Pi photoanode, the Fe:NiO and Co-Pi catalyst layer combined effect were used to prevent the photo corrosion. The Fe:NiO and Co-Pi OER catalysts over the electrode is supposed to reverse catalyst dissolution in phosphate buffers through a self-repair process[146] and improve the rate of interfacial charge transfer. Moreover, in the present study, the stability test was carried out in cyclic mode (11 h each cycle), and after each cycle, a fresh electrolyte was used. Using new electrolyte in each cycle provide fresh Ni/Co metal to participate in the self-repair process[147]. This could be the possible reason for the stability of the photoanode even after 33 h of cyclic operation.

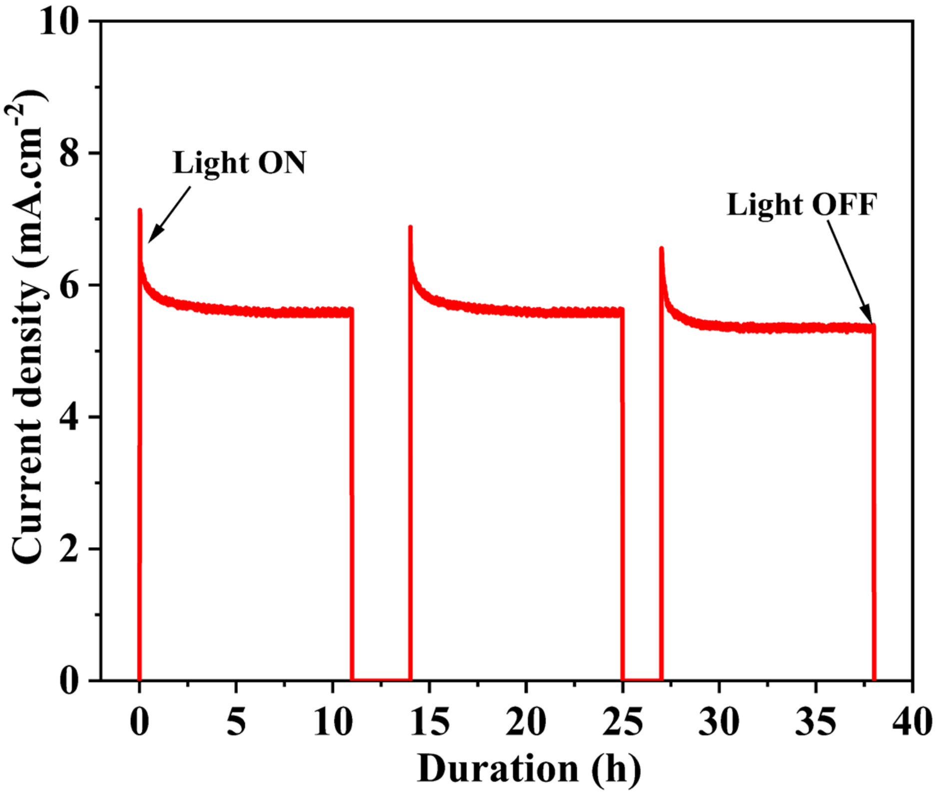

Figure 37 cyclic stability measurement for WO_3/(Y,W):$BiVO_4$/Fe:NiO/Co-Pi photoanode.

4.10 Conclusion

The role of individual element doping W, Er, Y, Yb and co-doping (Y,W), (Er,W) and Yb,W) in $BiVO_4$ with respect to their light absorption, bulk, surface charge separation and transfer properties has been studied in detail. The doping of the rare earth metal ions Y^{3+} Er^{3+} or Yb^{3+} at Bi^{3+} site enhances light absorption ($\lambda \leq 550$) due to reduction in bandgap but leads to decreased charge transport property compared to W^{6+} doped at V^{5+} site photoanode. The detailed investigation of absorption efficiency, photogenerated charge dissipation, transfer and electrochemical impedance showed that even though there is high charge separation in bulk on W doping, the defect is generated especially at the surface with Y^{3+} or Er^{3+} or Yb^{3+} doping at Bi^{3+} site act as a recombination center. By introducing the WO_3 heterojunction for efficient electron transfer between film and FTO interface, the (Y,W):$BiVO_4$ photoanode showed better performance than W:$BiVO_4$ photoanode. The WO_3/(Y,W):$BiVO_4$/Fe:NiO photoanode with type two heterojunction and p-n junction demonstrated near-complete (~95 %) suppression of electrons and holes recombination, efficient charge transfer (~75 %) and improved absorption efficiency (~85 %). Due to the p–n junction formed between the interface of WO_3/(Y,W):$BiVO_4$ and WO_3/(Er,W):$BiVO_4$ and Fe-NiO, an inner electric field is built, enhancing the surface reaction kinetics (transportation of electron-hole pairs), lowering the band bending conditions, and increasing the bulk charge separation. The WO_3/(Y,W):$BiVO_4$/Fe:NiO photoanode showed a PCD of 5.77 ± 0.3 $mA.cm^{-2}$ at 1.23 V and 7.4 ± 0.45 $mA.cm^{-2}$ at 2.0 V (vs RHE) in K_2HPO_4 electrolyte. The electrode has shown remarkably high incident and absorbed photon to current conversion efficiency (~97 %). Thus, rare earth metal Y or Er or Yb doping in $BiVO_4$ enhances light absorption but leads to decreased bulk and surface charge transport property, and this limitation can be overcome by using a suitable electron/hole transfer layer.

CHAPTER 5 DEVELOPMENT OF SULFUR MODIFIED Bi_2O_3 INTERFACIAL LAYER

5.1 Introduction

OER properties of $BiVO_4$ suffer from low charge transfer rates due to excessive surface recombination in the *ps-ns* time scale.[94,148] In parallel, the desirable water oxidation occurs at a slower time scale, typically over the *ms–s* range, due to its four-electron reaction mechanism.[149,7,9] Fast charge separation and transport of photogenerated electron-hole pairs are essential for efficient water oxidation.[8,10] Several strategies have been employed to enhance the charge separation and transfer, such as composition tuning or doping,[84,85] formation of homo- and hetero- junctions,[5,11,12] passivation layer[152] and co-catalyst.[153]

Tungsten (W) and molybdenum (Mo) have been extensively studied as donor-type dopants in $BiVO_4$ to increase charge carrier density and mobility and minimize recombination pathways at solid/solid /solid/ solid/electrolyte interfaces.[36,151] Along with composition tuning, forming heterojunction, in particular, type-II heterojunction formation between WO_3 (bandgap: 2.7 eV, VB: 0.4 eV & CB: 3.1 eV) and $BiVO_4$ (VB: 0.02 eV & CB: 2.4 eV) is efficient due to appropriate band alignment, which promotes spatial charge separation and relatively better charge transfer by providing substantial thermodynamic driving force and interfacial electric field.[6,16]

5.2 Drawbacks of WO_3/$BiVO_4$ heterojunction

As shown from Figure 38, the WO_3/$BiVO_4$ heterojunction suffers from (1) slow charge transfer (sub μs) from $BiVO_4$ to WO_3 due to poor transport properties $BiVO_4$ and simultaneous photoexcited leading to a shorter lifetime of the electron.[155] The interface between The interface of WO_3/$BiVO_4$ contain (2) recombination center and trap sites that causes additional recombination at the heterojunction interface.[8,17] Consequently, (3) new recombination channel activates where electrons from the conduction band recombine with trapped holes in the valence band of $BiVO_4$.[155]

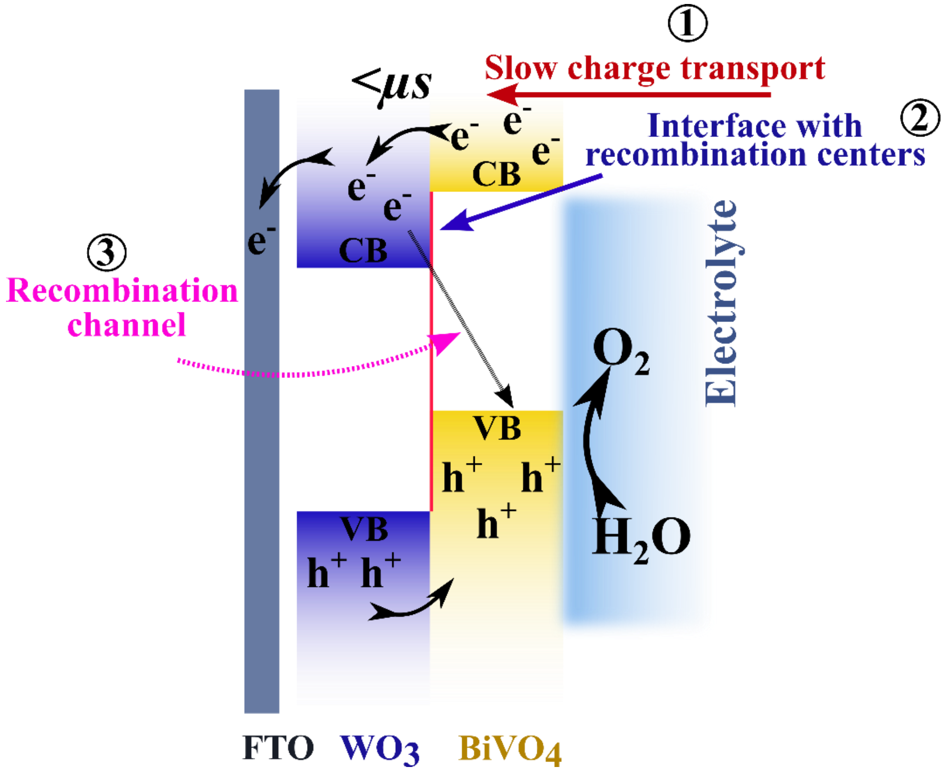

Figure 38 Major drawbacks of $WO_3/BiVO_4$ heterojunction.

5.3 The proposed solution to resolve the limitation of $WO_3/BiVO_4$ heterojunction

Our or other groups in the field have made several efforts to improve interfacial passivation, charge transfer, and reducing recombination sites by additional (interfacial or under/over) layers in $WO_3/BiVO_4$ heterojunction photoanodes. The obtained photocurrent densities at 1.23 V_{RHE} are plotted in Figure 9a. and Table S5. Choi et al.[157] incorporated a mild W doped $BiVO_4$ interfacial layer in the $WO_3/BiVO_4$ heterojunction for unidirectional charge flow. Zhang et al.[158] designed a three-story device to improve the conductivity by placing reduced graphene oxide between WO_3 and $BiVO_4$ layers that acted as a multichannel pathway. A Z-scheme device was designed by Wang et al.[159] by incorporating a W-layer between $BiVO_4$ and WO_3 layers for accessing holes. Beak et al.[160] used porous

SnO_2 underlayer in the WO_3/$BiVO_4$ heterojunction where WO_3/(WO_3+SnO_2) layers formed a mixed composite for better contact and low resistance. Figure 9b and Table S6 compare hydrogen production rates at 1.23 V_{RHE} under simulated AM 1.5G illumination for $BiVO_4$ based heterojunction photoanodes along with the present results on our WO_3/S:Bi_2O_3/(Ga,W):$BiVO_4$/Co-Pi photoanode. Our results are among the highest reported photocurrent densities and hydrogen production rates.

In order to overcome the mentioned challenges, an interfacial layer (Bi_2O_3) was placed synergistically between the WO_3/$BiVO_4$ heterojunction, as detected in Figure 39. Additionally, Bi2O3 has a staggered structure. This layer was supposed to facilitate (1) enhance the charge transfer rate after simultaneous photoexcited, leading to longer lifetime and rapid electron and hole transfer (> sub μs) of the electron. Simultaneous, (2) Bi_2O_3 provide a much better crystal match between WO_3/Bi_2O_3 and Bi_2O_3/$BiVO_4$ and rapid charge transfer rate leading to minimize interfacial recombination. Consequently, (3) interfacial layer (Bi_2O_3) acts as an electron blocking layer, reducing interfacial recombination and deactivating or minimizing the new recombination channels.

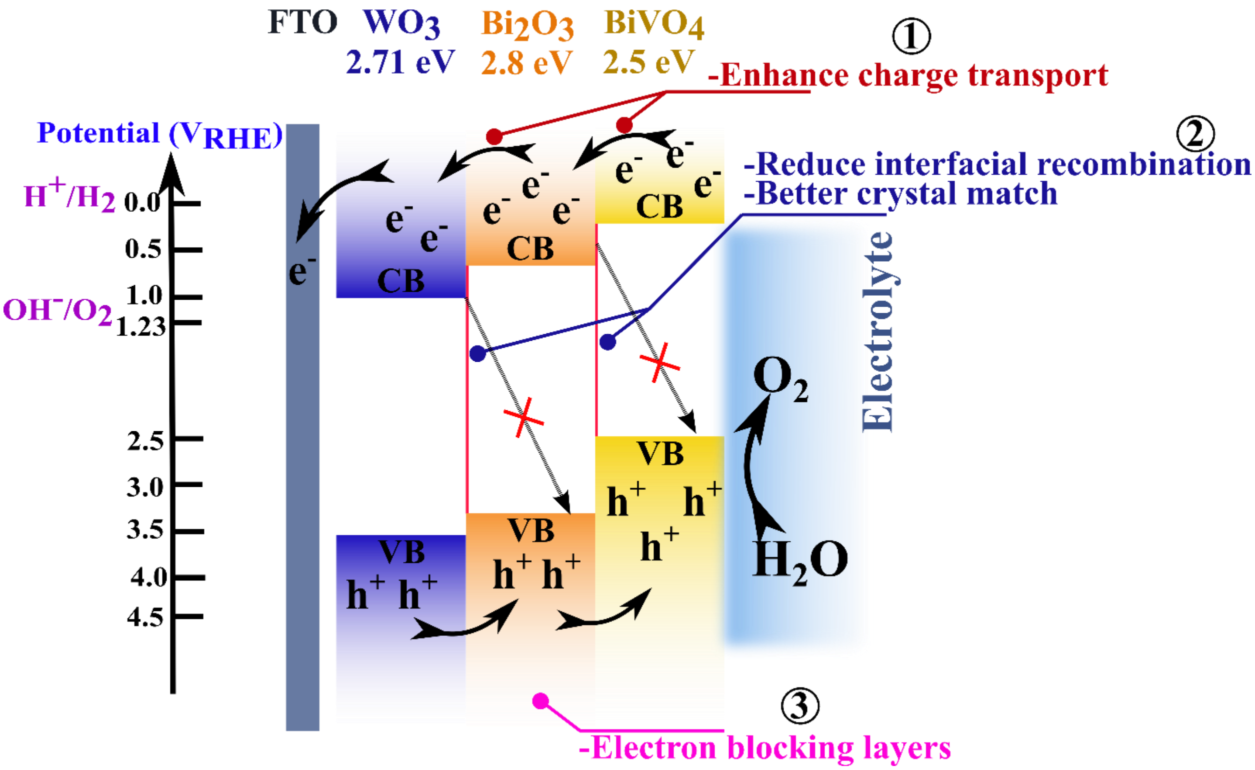

Figure 39 Proposed solution to resolve the limitation of $WO_3/BiVO_4$ heterojunction.

In the present study, a multifaceted approach was implemented for addressing the interfacial charge recombination in $WO_3/BiVO_4$ heterojunction where (i) $BiVO_4$ was co-doped and (ii) an interfacial layer was implemented to improve the effective charge separation and transfer. Initially, $BiVO_4$ was co-doped with Ga^{3+} and W^{6+} at the Bi^{3+} and V^{5+} sites, respectively, to enhance light absorption, the concentration of photogenerated charge carriers, and improve bulk charge separation. A uniquely prepared sulfur (S) modified Bi_2O_3 ($S:Bi_2O_3$) layer was implemented so that S diffused to adjacent underlayer (WO_3) and overlayer ($(Ga,W):BiVO_4$), which helped in increasing additional reactive sites for charge transport. Energy-dispersive X-ray analysis (EDAX), X-ray photoelectron spectroscopy (XPS) and time-of-flight secondary ion mass spectrometry (TOF-SIMS) depth profiling determined the qualitative and uniform distribution of sulfur in all layers. The PCD increased from 2.8±0.12 to 4.0±0.2 mA.cm^{-2} for WO_3/(Ga,W):$BiVO_4$ and WO_3/S:Bi_2O_3/(Ga,W):$BiVO_4$, respectively. Additionally, the photocurrent improved to 5.1±0.25 mA.cm^{-2} after adding cobalt phosphate (Co-Pi) to yield a hydrogen collection rate of 67.3 μmol.h^{-1}cm^{-2} for WO_3/S:Bi_2O_3/(Ga,W):$BiVO_4$/Co-Pi photoanode at 1.23 V_{RHE} in K_2HPO_4 (KPi) under simulated AM 1.5G illumination. Time-resolved photoluminescence (TRPL) and in *operando* femto- and nano-second transient absorption spectroscopy (fs- and ns- TA) results are consistent with more holes rapidly directed to the reactive surface initially and fast electron transfer from (Ga,W):$BiVO_4$ to S:Bi_2O_3 in *ps-ns* and from S:Bi_2O_3 to WO_3 in *ns-μs* time scale. From the detailed analysis, we show that the insertion of a S:Bi_2O_3 interfacial layer resulted in the best charge separation and transfer kinetics, as well as reduced interfacial recombination sites of all architectures tested. The achieved results are among the highest reported photocurrent densities and hydrogen production rates in the literature.

5.4 Experimental

The $BiVO_4$ based thin films were fabricated on 1×1 cm^2 fluorine-doped tin oxide (FTO) glass substrate (Aldrich Chemistry: 2.3 mm thick, ~7 Ω/sq surface resistivity) using ultrasonic spray coating (Sono-Tek Corporation, USA). A precursor solution of $BiVO_4$ was prepared by dissolving 3mM $Bi(NO_3)_3{\cdot}5H_2O$ (Alfa-Aesar, CAS#10035060) and 3mM NH_4VO_3 (Sigma-Aldrich, CAS#7803556) in 2M HNO_3 (Sigma-Aldrich, CAS#7803556). The precursor solution was sprayed at a 0.1 ml/min flow rate for 4 cycles over a FTO substrate held at 70°C, then annealed for 10 min at 500°C in the furnace (Thermo Scientific

Thermolyne, model: F48028). The annealed film was sprayed with an additional 4 cycles for optimized film thickness and then annealed at 500°C for 2 h. Ga doping was performed by dissolving 3mM $Ga(NO_3)_3.xH_2O$ (Sigma-Aldrich, CAS#69365726) in the $BiVO_4$ precursor solution to get varied $Bi_{1-x}Ga_xVO_4$ compositions (where x = 0.01 - 0.06 and x = 0.04 was found to be optimal) (Figure S1a). W doping was carried out non-stoichiometricaly[36] by mixing 3mM $(NH_4)_{10}H_2(W_2O_7)_6$ (Sigma-Aldrich, CAS#11140775) in the $BiVO_4$ precursor solution to acquire $BiV_{0.992}W_{0.013}O_4$ (termed W:$BiVO_4$). The simultaneous co-doping of Ga and W in $BiVO_4$ was executed by taking the required amount of gallium nitrate and ammonium tungstate in $BiVO_4$ precursor solution to obtain $Bi_{0.96}Ga_{0.04}V_{0.992}W_{0.013}O_4$ (termed (Ga,W):$BiVO_4$).

WO_3 films were fabricated by dissolving 3mM $(NH_4)_{10}H_2(W_2O_7)_6$ (Sigma-Aldrich, CAS#10031513) in 2M HNO_3 (Sigma-Aldrich, CAS#7803556). Using an ultrasonic spray coating tool, the precursor solution was sprayed for 4 cycles over FTO substrate (kept at 40°C) with a 0.1 ml/min flow rate. Next, the film was annealed at 500°C for 2 h in the air to obtain a thin adherent WO_3 film. (Ga,W):$BiVO_4$ was then sprayed over the WO_3 film to form WO_3/(Ga,W):$BiVO_4$.

The precursor solution for Bi_2O_3 was prepared by dissolving 1mM $Bi(NO_3)_3{\cdot}5H_2O$ (Alfa-Aesar, CAS#10035060) in 10 ml acetic acid (Sigma-Aldrich, CAS#64197). WO_3/Bi_2O_3 film was fabricated by ultrasonically spraying Bi_2O_3 precursor on WO_3 film (kept at 70°C) for 3 cycles. The WO_3/Bi_2O_3 bilayer was then annealed at 500°C for 2 h in air. (Ga,W):$BiVO_4$ was subsequently sprayed (as discussed) to form WO_3/Bi_2O_3/(Ga,W):$BiVO_4$.

Figure 40 show a schematic of the WO_3/S:Bi_2O_3/(Ga,W):$BiVO_4$/Co-Pi film fabrication process. First, the sprayed Bi_2O_3 film was immersed in 35 ml methanol (Sigma-Aldrich, CAS#67561) and 0.4mM dibenzyl disulfide (Alfa Aser, CAS#150607) for 20 min and then annealed in sulfur vapor using a tube furnace (Thermo Scientific Thermolyne, model: HTF55322C). Next, sulfur vapor was generated by heating 2.5 g of sulfur powder (Alfa Aser, CAS#7704349) at 120°C in the tube furnace's upstream section. Argon (purity: 99.99%) was used as a carrier gas the sulfur vapor downstream where the thin film was placed in the hot zone of the tubular furnace at 445°C in air for 1 h to incorporate S in the Bi_2O_3 (termed S:Bi_2O_3). In the final step, the sulfur-rich film with WO_3 layer was used as a substrate to spray (Ga,W):$BiVO_4$ precursor solution and annealed in air at 500°C for 2 h to obtain WO_3/S:Bi_2O_3/(Ga,W):$BiVO_4$ film.

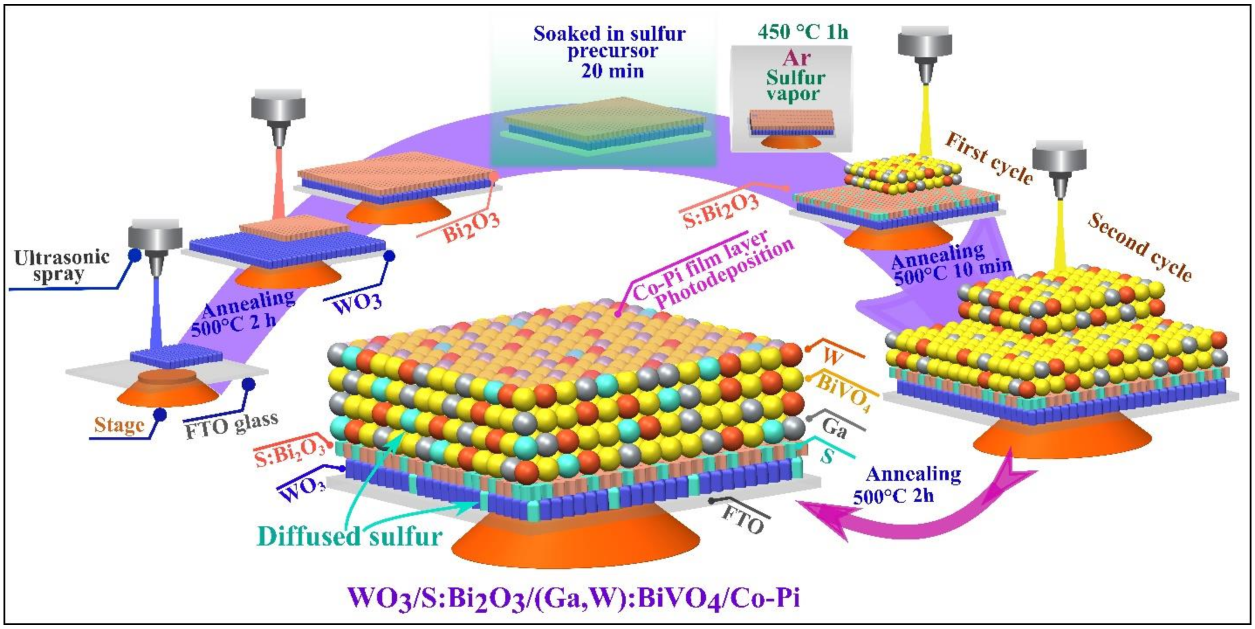

Figure 40 Schematic illustration of the WO_3/S:Bi_2O_3/(Ga,W):$BiVO_4$/Co-Pi film fabrication process.

A co-catalyst Co-Pi was photo-electrodeposited by dissolving 0.1M K_2HPO_4 (Sigma-Aldrich, CAS#7758114) and 0.5mM $Co(NO_3)_2 \cdot 6H_2O$ (Sigma-Aldrich, CAS#10026229) in DI water at 0.71 $V_{Ag/AgCl}$ for 30 s under simulated AM 1.5G illumination to obtain WO_3/S:Bi_2O_3/(Ga,W):$BiVO_4$/Co-Pi.

5.5 Photoelectrochemical and optical measurements

Looking first at films, Figure 41a compare the PEC performance of intrinsic $BiVO_4$ (i-$BiVO_4$), Ga:$BiVO_4$, W:$BiVO_4$ and (Ga,W):$BiVO_4$ under chopped light up to 2.4 V_{RHE}. Ga:$BiVO_4$ exhibited 0.4±0.02 $mA.cm^{-2}$, almost twice that of the i-$BiVO_4$ (0.25±0.01 $mA.cm^{-2}$); this improvement is attributed to increased Fermi-level splitting and therefore decreased carrier recombination, via incorporation of Ga^{3+} at Bi^{3+} sites.[161] Similarly, W:$BiVO_4$ exhibited enhanced PCD (1.02±0.04 $mA.cm^{-2}$) of over four times that of i-$BiVO_4$, which is attributed to increased carrier concentration from W^{6+} donors at V^{5+} sites.[162] Finally, (Ga,W):$BiVO_4$ demonstrated superior (~ 7 times) PEC performance (1.68±0.1 $mA.cm^{-2}$) compared to i-$BiVO_4$, likely due to the combined effects of Ga and W doping.

Next, PEC performance of heterojunctions was evaluated (Figures 41b). Figure 41a, (Ga,W):$BiVO_4$ was selected to form a type-II heterojunction with WO_3. By doing so, WO_3/(Ga,W):$BiVO_4$ photoanode showed 2.8±0.12 $mA.cm^{-2}$ photocurrent, nearly doubled compared to (Ga,W):$BiVO_4$, likely due to improved light absorption at $\lambda \leq 450$ nm, charge transfer kinetics and reduced recombination sites.[163,164] However, the WO_3/$BiVO_4$

interface has a high defect density, which can lead to significant recombination and slow charge transport.[148,156] Therefore, a thin layer of bismuth oxide (Bi_2O_3) was inserted at the WO_3/$BiVO_4$ interface. While Bi_2O_3 has appropriate band alignment to promote charge transfer, the PEC was not significantly enhanced relative to WO_3/(Ga,W):$BiVO_4$ (only 1.2 times higher), likely due to the higher levels of recombination in this layer.[165] Therefore, sulfur (S) was incorporated into the Bi_2O_3 such that, along with passivating the Bi_2O_3 bulk, S also diffused into the adjacent WO_3 and (Ga,W):$BiVO_4$ layers (Figure 41b). Sulfur is expected to enhance water oxidation by generating oxygen vacancies and forming new reaction sites that help charge migration/separation and reduce carrier recombination.[25,26] The optimized WO_3/S:Bi_2O_3/(Ga,W):$BiVO_4$ photoanode demonstrated an excellent photocurrent of 4.0±0.2 mA.cm^{-2} at 1.23 V_{RHE} which was ~1.2 and ~1.5 times higher than the WO_3/Bi_2O_3/(Ga,W):$BiVO_4$ and WO_3/(Ga,W):$BiVO_4$ photoanodes, respectively.

A surface catalyst (Co-Pi) deposited WO_3/S:Bi_2O_3/(Ga,W):$BiVO_4$/Co-Pi photoanode exhibited a remarkably high photocurrent 5.1±0.25 mA.cm^{-2} at 1.23 V_{RHE} in KPi. The Co-Pi layer facilitates hole collection at the photoanode/electrolyte interface to participate in the water oxidation reaction.[85]

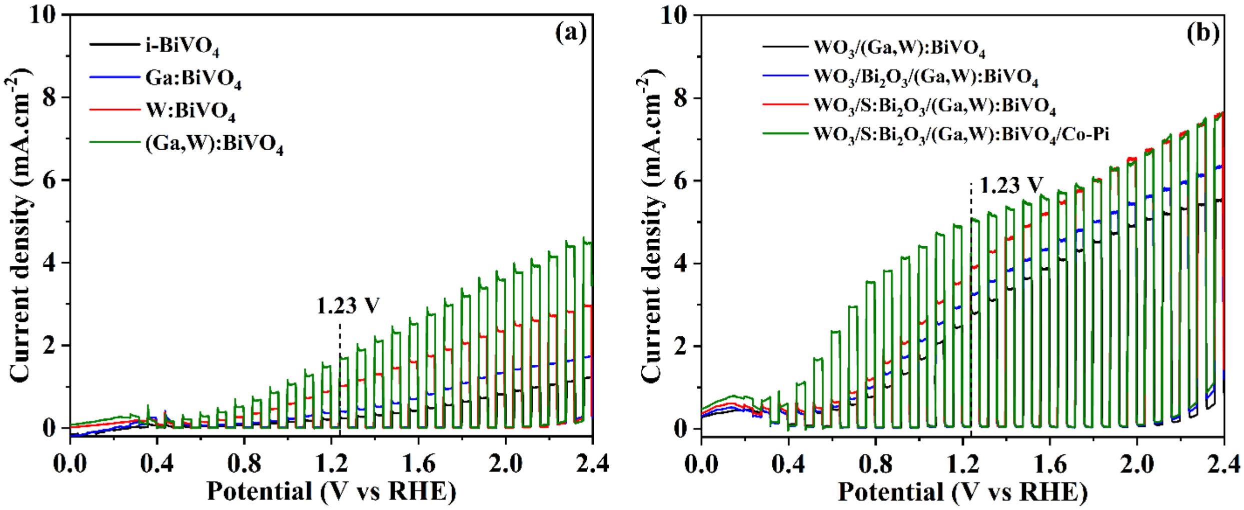

Figure 41 J−V plots under simulated AM 1.5G illumination in KPi for photoanodes (a) Ga, W doped and (Ga,W) co-doped along with i-BiVO$_4$, (b) with WO$_3$ heterojunction and Bi$_2$O$_3$ interface layer without and with sulfur modification.

The spectral response was investigated to understand the impact of doping, co-doping and heterojunction formation. From Figure 42, it was observed that doping BiVO$_4$ with Ga enhanced total light absorption and extended the onset from ~520 to ~535 nm. A similar trend was observed for the co-doped (Ga,W):BiVO$_4$ sample, likely due to the redshift in light absorption caused by Ga doping.[161] There was no substantial change in absorption observed for W doping.[84] Moreover, the light interaction improved by forming a heterojunction with WO$_3$ (i.e, WO$_3$/(Ga,W):BiVO$_4$) where WO$_3$ ($\lambda \leq$ 450 nm) absorbs high energy photons along with modified BiVO$_4$ (300 – 530 nm), which absorb a wide range of photons. S:Bi$_2$O$_3$ ($\lambda \leq$ 430) further improved the light interaction for WO$_3$/S:Bi$_2$O$_3$/(Ga,W):BiVO$_4$ compared to WO$_3$/Bi$_2$O$_3$/(Ga,W):BiVO$_4$ due to the formation of interband on S modification which causes the redshift in the light absorption.[165,166] The respective absorption efficiency (ϕ_{abs}) was calculated by integrating the absorption spectra from 300 to 550 nm for all samples and indicated in Figure 42a and

42a: inset. The measured bandgaps were 2.71 and 2.8 eV for WO_3 and Bi_2O_3, respectively. There was a slight (~0.04 eV) reduction in the optical bandgap for Ga:$BiVO_4$ (2.39 eV) and (Ga,W):$BiVO_4$ (2.38 eV) compared to i-$BiVO_4$ (2.42 eV), which was expected due to the redshift in the absorption edge on Ga doping.

The IPCE determined the quantification of absorbed photons undergoing photoactivity corresponding to wavelength. The measurement for all heterojunction based photoanodes was conducted at 1.23 V_{RHE} (Figure 3b). WO_3/S:Bi_2O_3/(Ga,W):$BiVO_4$ photoanode showed maximum IPCE value 63±3% followed by WO_3/Bi_2O_3/(Ga,W):$BiVO_4$ (52±2%) and WO_3/(Ga,W):$BiVO_4$ (42±1.6%), respectively at 460 nm. The WO_3/S:Bi_2O_3/(Ga,W):$BiVO_4$ photoanode with Co-Pi exhibited the highest IPCE (72±3.2%). The IPCE was integrated over the AM1.5G reference spectrum, and the resulting photocurrent densities for each sample (Figure 42b) agreed with those measured under simulated AM 1.5G illumination at 1.23 V_{RHE} (Figure 41b). Due to measuring uncertainty, the small variation (~ 5%) in the photocurrents measured by LSV and integrated current from IPCE is a general phenomenon.

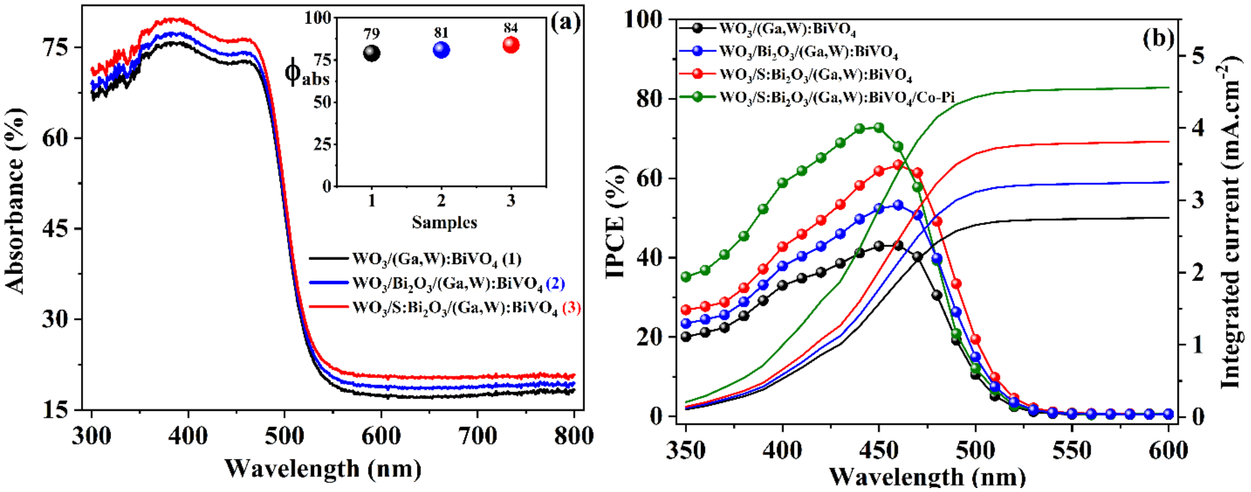

Figure 42 (a) Absorption spectra (inset: absorption efficiency), (b) incident photon-to-current efficiency, measured at 1.23 V_{RHE} in KPi electrolyte for photoanodes with WO_3 heterojunction and Bi_2O_3 interface layer without and with sulfur modification.

5.6 Surface morphology, crystal structure and elemental analysis of thin films

To better understand the PEC performance trends, the physicochemical characterization of intrinsic and doped samples was carried out to evaluate morphology, elemental mapping, crystal structure and oxidation state. The SEM images reveal that i-$BiVO_4$, WO_3 and Bi_2O_3 have a planar structure with uniform nanoporous morphology. Figure 43a shows that after co-doping the i-$BiVO_4$ film with Ga and W, the overall porosity increased substantially without changing the grain size (50 – 200 nm). The inset image illustrates the consistent growth of nano-size grains, leading to better light absorption and more electrochemical active surface area by increasing the contact area between film surface and electrolyte. The cross-section image (Figure 43b) for WO_3/S:Bi_2O_3/(Ga,W):$BiVO_4$ demonstrated the uniformly connected nanoporous grains. The layers thicknesses are 200-300, 200-300 and 500-750 nm for the WO_3, S:Bi_2O_3 and (Ga,W):$BiVO_4$ layers, respectively. It was observed that clear separation of all three layers is difficult as layers amalgamated due to the porous nature of all films. The FTO coating thickness on the glass substrate was ~50 nm. The composition and elemental distribution of as-deposited WO_3/S:Bi_2O_3/(Ga,W):$BiVO_4$ were mapped based on the integrated intensities of peak Bi, V, O,W, Ga and S signals as a function of beam position using FESEM-EDAX mode. Figure 43c-h reveals the uniform distribution of elements Bi, V, O, W, Ga, and S. Consequently, the element spectra in Figure 4i demonstrates the uniform presence of S along with other elements. In Figure 43i inset, Bi and S peaks were deconvoluted to determine the distinct measure of S due to the near overlap of the two peaks. S and Bi peaks were determined at 2.36 and 2.45 keV, respectively. Additionally, the quantification of S was determined to be 2.77 at% from EDAX analysis (Figure 4i: inset).

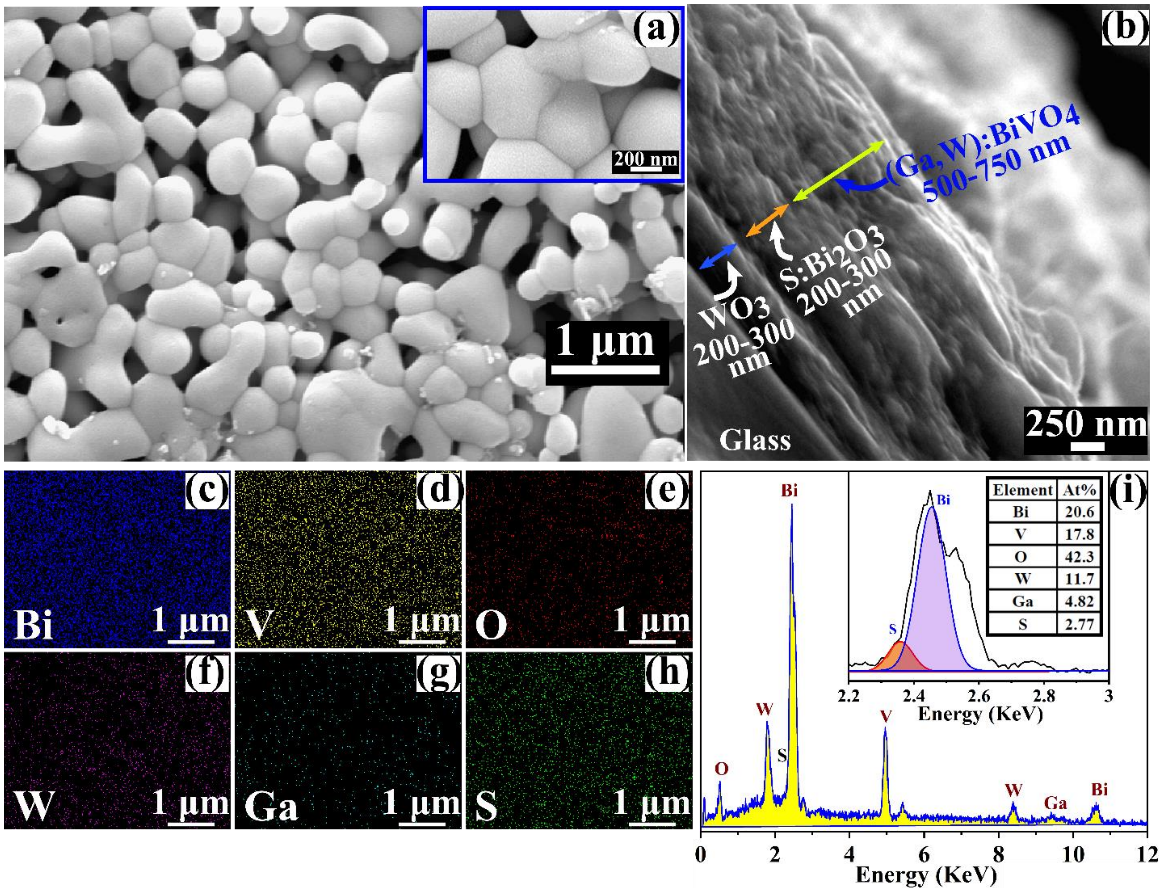

Figure 43 (a) Surface morphology. (b) Cross-section, (c-h) plan view elemental mapping and (i) elemental spectra (inset: deconvolution of Bi and S peaks and at%) of WO3/S:Bi_2O_3/(Ga,W):$BiVO_4$ sample.

The crystal structure was determined using X-ray diffraction (XRD) analysis for intrinsic, doped $BiVO_4$, Bi_2O_3, WO_3 and heterojunction samples without any impurity, complex phases and S peaks.[155] The oxidation state of Bi, V, W, Ga and O in WO_3/S:Bi_2O_3/(Ga,W):$BiVO_4$ sample was determined using surface XPS. However, subsequently employed XPS depth profiling could not identify S in any layers due to the low concentration of S and detection limit of XPS. In order to determine the oxidation states of sulfur, two distinct samples were prepared (Figure 44a): an intermediate S treated WO_3/Bi_2O_3 and WO_3/S:Bi_2O_3/(Ga,W):$BiVO_4$ with high S content (total S treatment to WO_3/Bi_2O_3 layer was 4 hrs, 4 times than actual sample). From the S 2s spectrum in Figure 44b, the oxidation state of S was attributed to -2 in the form of Bi_2S_3 (224.8 eV) and Bi_2O_3 (230.6 and 233.8 eV) peaks for S treated WO_3/Bi_2O_3 sample.[109] Similarly, WO_3/S:Bi_2O_3/(Ga,W):$BiVO_4$ sample with high S content validated -2 states (Bi_2S_3 (223.4 eV) and Bi_2O_3 (233.3 eV)). However, it is possible that peaks at 233.8 eV and 233.3 eV could also have sulfates or highly oxidized sulfur species (SO_x).[109] Additionally, depth profiling was performed in Figure 44c for WO_3/S:Bi_2O_3/(Ga,W):$BiVO_4$ with high S content sample to determine the atomic concentration of Bi 4f, V 2p, O 1s, W 4f, Ga 2p and S 2s with depth. It was observed that the S distribution was uniform throughout the film depth except slightly higher at the film surface. The atomic concentration of S was approximately 12 at% uniformly distributed in the sample with high S content. It may be estimated that sulfur could be approximately 3 at% uniformly distributed in the actual sample considering S diffusion rates as sulfur treatment was 4 times in high S content sample. The atomic concentration of Bi 4f, V 2p, O 1s, W 4f and Ga 2p was distributed as per the filmstack structure. The V 2p and Ga 2p was noticed to have minor diffusion in the adjacent layers, which was possible due to the porous nature of the film.

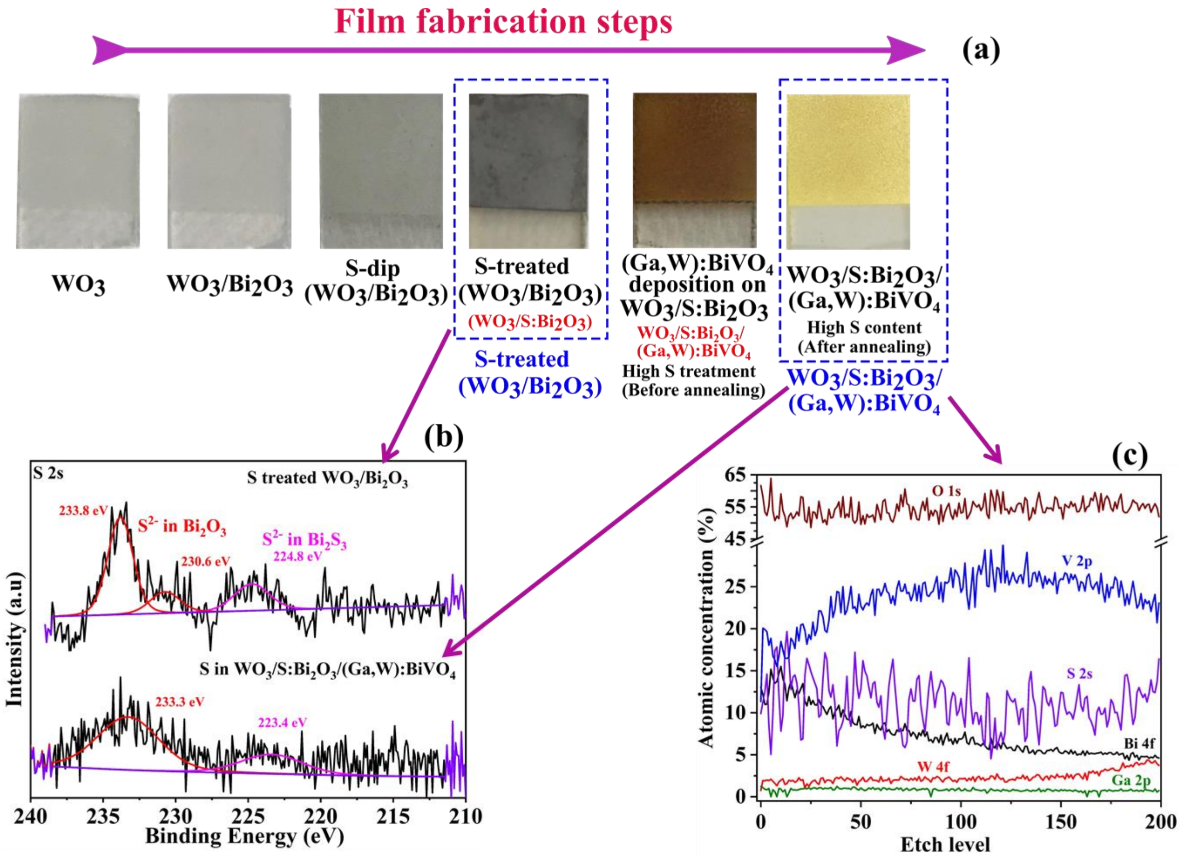

Figure 44 (a) Prepared sample for the XPS surface and depth profiling. (b) S 2s XPS spectra of S treated WO_3/Bi_2O_3 and with high S concentrated $WO_3/S:Bi_2O_3/(Ga,W):BiVO_4$ film. (c) XPS depth profiling spectra for atomic concentration (%) of Bi 4f, V 2p, O 1s, W 4f, Ga 2p and S 2s as a function of etch level for $WO_3/S:Bi_2O_3/(Ga,W):BiVO_4$ film with high S content.

In order to understand the nature of the sulfur diffusion process in the actual film from Bi_2O_3 interfacial layer to the WO_3 and $(Ga,W):BiVO_4$ adjacent layers, TOF-SIMS depth profiling was employed for the $WO_3/S:Bi_2O_3/(Ga,W):BiVO_4$ sample in three distinct annealing conditions after $(Ga,W):BiVO_4$ precursor deposition on sulfur treated WO_3/Bi_2O_3 film. The prepared samples, as shown in Figure 45a, were control (without annealing), short annealing (5 min) and complete annealing (final sample). Secondary ion signals were selected, which were of high intensity and represented major components of the various layers in the filmstack. These species were: Bi^-, VO^-, WO_2^-, GaO^- and S^- to represent Bi, V, W, Ga and S elements, respectively. The layers interface was not measured due to high surface roughness, and it was also observed that clear distinction of each layer was difficult (Figure 43b and 43a) due to their porous nature. The control sample showed that sulfur was contained to the Bi_2O_3 layer only, as observed by the pronounced sulfur peak in the Bi_2O_3 layer in Figure 45b. Contrarily, Figure 45c demonstrated that even on short annealing of 5 min at 500°C, significant migration of sulfur has occurred as the sulfur distribution migrated significantly into the (Ga,W):$BiVO_4$ and WO_3 layers, also noted by the significant broadening of the sulfur trace. Subsequently, in Figure 45d, a completely annealed sample (2 h time at 500°C) showed that the sulfur distribution was uniform throughout the film thickness, which was also corroborated by EDAX analysis (Figure 43c-i) and XPS depth profiling (Figure 44b). However, the sulfur content was higher on the (Ga,W):$BiVO_4$ surface, possibly due to the small deposition of sulfur during migration from Bi_2O_3 layer similar behavior was observed from XPS depth profiling (Figure 44c). It was assumed that sulfur was passivated in all grain boundaries and surfaces/interfaces/defects throughout all layers, rather than being a bulk alloy element. Along with sulfur, a less extreme amount of diffusion was observed for the components Bi, V, W and Ga in the film thickness (Figure 45b-d) may be due to the highly porous nature of the film (Figure 43a) similar behavior was observed from XPS depth profiling. The distribution of the substrate elements (F^-, Sn^- and Si^-) was also observed.

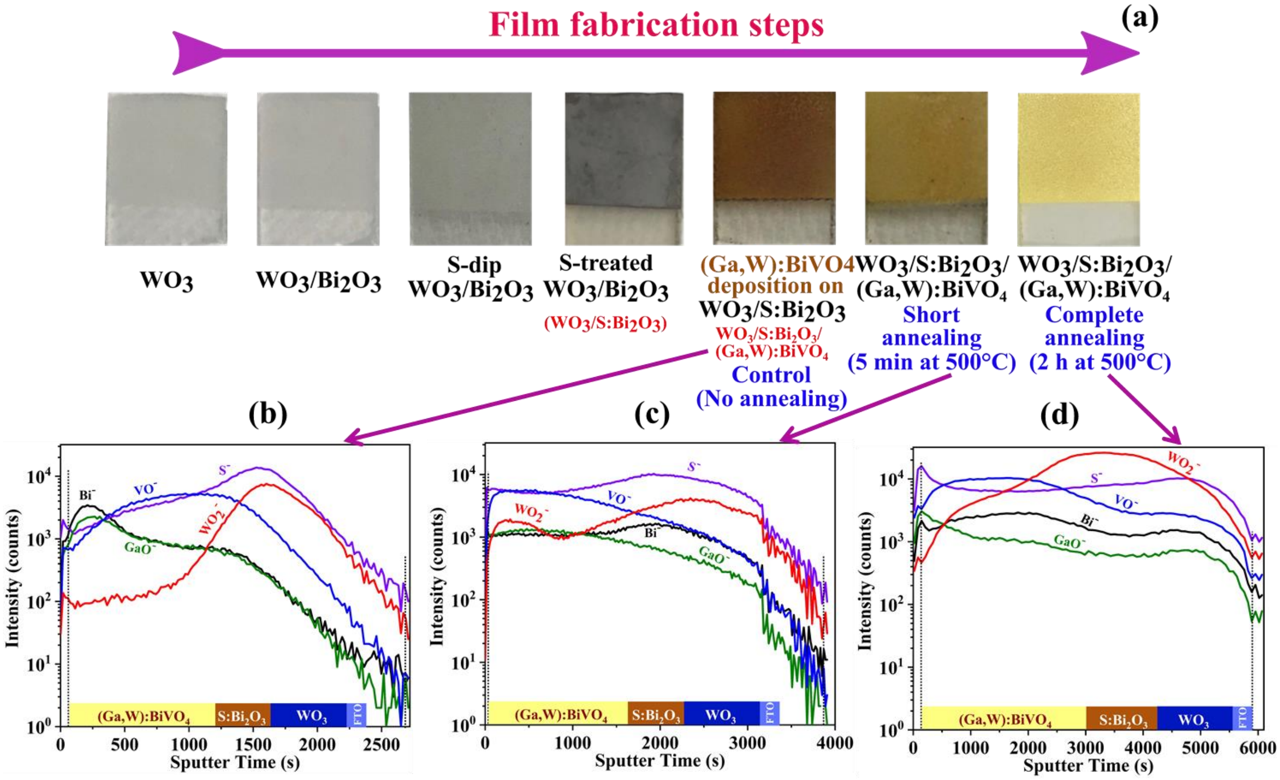

Figure 45 (a) Prepared sample for TOF-SIMS in three distinct environments control (no annealing), short annealing (5 min at 500°C) and complete annealing (2h at 500°C). Negative polarity TOF-SIMS depth profiles of $WO_3/S:Bi_2O_3/(Ga,W):BiVO_4$ sample for three distinct environments (a) control (no annealing), (b) short annealing (5 min at 500°C) and (c) complete annealing (2h at 500°C) for Bi-, VO-, WO2-, GaO and S^- species.

5.7 Electrochemical impedance analysis

Figure 46a shows the impedance patterns of photoanodes with WO_3 heterojunction and Bi_2O_3 interface layer without and with sulfur modification. $WO_3/(Ga,W):BiVO_4$ photoanode shows lower impedance than $WO_3/Bi_2O_3/(Ga,W):BiVO_4$ at the low-frequency region. Interestingly, $WO_3/S:Bi_2O_3/(Ga,W):BiVO_4$ photoanode demonstrated even lower real impedance at a lower frequency than $WO_3/Bi_2O_3/(Ga,W):BiVO_4$. Resistance and capacitance in bulk and at the surface were evaluated as a function of voltage using Randles circuits (Figure 46b & 46c), which consists of resistance related to connections (R_{series}), bulk resistance (R_{bulk}), surface resistance ($R_{surface}$), bulk capacitance (C_{bulk}) and surface capacitance ($C_{surface}$) connected to a Helmholtz layer at the photoanode and electrolyte interface.

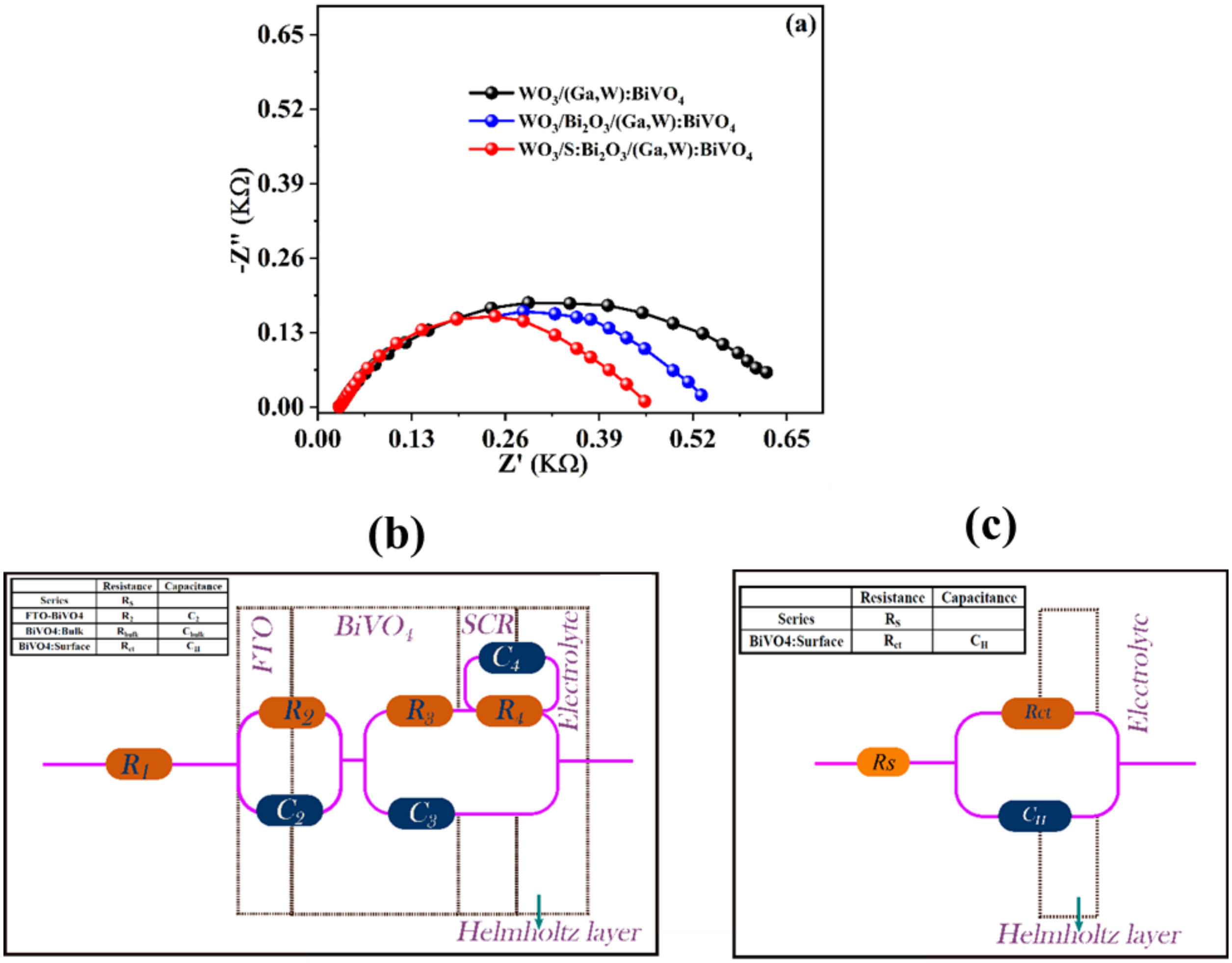

	Resistance	Capacitance
Series	R_s	
FTO-BiVO4	R_2	C_2
BiVO4:Bulk	R_{bulk}	C_{bulk}
BiVO4:Surface	R_{ct}	C_H

	Resistance	Capacitance
Series	R_S	
BiVO4:Surface	R_{ct}	C_H

Figure 46 (a) Nyquist plots measured in KPi at 1.23 VRHE under simulated AM 1.5G illumination. (c) and (d) Randles circuit for calculating $R_{surface}$, R_{bulk}, $C_{surface}$ and C_{bulk}.

Figure 47a shows that R_{bulk} and $R_{surface}$ tend to drop gradually until ~1 V_{RHE} after which, the photocurrent was mainly controlled by photogenerated holes reaching the surface.[168] R_{bulk} followed the order of $WO_3/S:Bi_2O_3/(Ga,W):BiVO_4$ < $WO_3/Bi_2O_3/(Ga,W):BiVO_4$ <

WO_3/(Ga,W):$BiVO_4$. The evaluated capacitance of photoanodes shown in Figure 47b illustrated that C_{bulk} decreases with increasing potential and exhibits less recombination in bulk and facilitated charge transfer. The $C_{surface}$ gradually increased with potential, followed the trend WO_3/S:Bi_2O_3/(Ga,W):$BiVO_4$ > WO_3/Bi_2O_3/(Ga,W):$BiVO_4$ > WO_3/(Ga,W):$BiVO_4$. The interfacial layer with S enhanced the charge transfer rate, facilitated the charge accumulation and transport by reducing the density of surface trapped holes in the bulk and the surface.

Total resistance (R_{tot}), which represent the combination of charge transport (bulk) and interfacial charge transfer (surface), was evaluated using $R_{tot} = (\frac{dI}{dV})^{-1}$ in Figure 47c. A valley was observed at ~1 V_{RHE} for all photoanodes. The cathodic shift of 164.3 and 33.5 mV in the valley implied higher charge extraction and a decrease in the R_{tot} of 39.2 and 12 $\Omega.cm^{-2}$ for WO_3/S:Bi_2O_3/(Ga,W):$BiVO_4$ and WO_3/S:Bi_2O_3/(Ga,W):$BiVO_4$, respectively from WO_3/(Ga,W):$BiVO_4$) indicated the reduced bulk recombination (indicated in Figure 6b).[168,169] Both of these criteria best fit the WO_3/S:Bi_2O_3/(Ga,W):$BiVO_4$ photoanode confirms the higher charge separation and transfer rate. The close relationship was demonstrated by R_{tot} calculated from I-V ($R_{tot} = \left(\frac{dI}{dV}\right)^{-1}$) and impedance measurement (R_{tot}=R_{bulk}+$R_{surface}$) as shown in Figure 6d. This excellent agreement substantiates the photocurrent obtained from experiment.

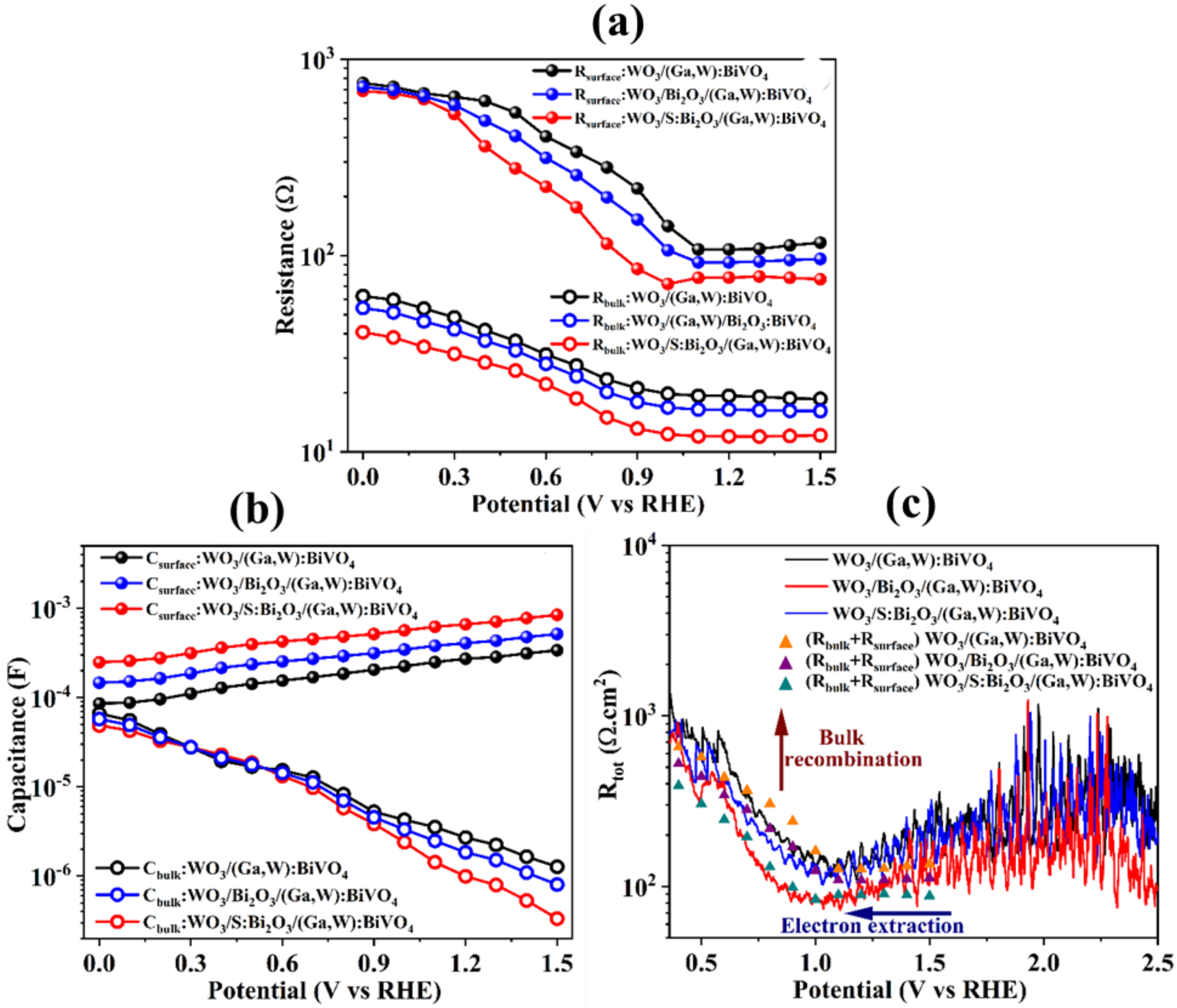

Figure 47 (a) $R_{surface}$ (solid markers) , R_{bulk} (open markers), (b) $C_{surface}$ (solid markers) and C_{bulk} (open markers) determined using Randles circuit (Figure 46 b and c) for photoanodes with WO_3 heterojunction and Bi_2O_3 interface layer without (blue) and with (red) sulfur modification. (c) R_{tot} (line) calculated by $(\frac{dI}{dV})^{-1}$ and compared with R_{tot} (triangles) obtained by impedance (R_{tot}=R_{bulk}+$R_{surface}$) measurement.

5.8 Time-resolved study of charge dynamics

The photogenerated charge carrier dynamics and kinetics were explored by TRPL measurement of the WO_3/(Ga,W):$BiVO_4$ and WO_3/S:Bi_2O_3/(Ga,W):$BiVO_4$ samples.

Figure 48 exhibits the PL intensity decay after excitation the thick (Ga,W):$BiVO_4$ layer and likely produces excited states in this layer by a laser source centered at 405 nm. The PL decay ($I(t)$) was fit with a second-order exponential function $I(t) = A_1 \exp\left(-\frac{t}{\tau_1}\right) + A_2 \exp\left(-\frac{t}{\tau_2}\right)$, where A_1 and A_2 are amplitudes of components with lifetime τ_1 and τ_2, respectively.[170] The average PL lifetime (<τ>) of each sample was calculated using $< \tau > = \frac{A_1\tau_1^2+A_2\tau_2^2}{A_1\tau_1+A_2\tau_2}$ (all calculated parameters are presented in Table 2). The average carrier lifetimes for WO_3/(Ga,W):$BiVO_4$ and WO_3/S:Bi_2O_3/(Ga,W):$BiVO_4$ were 0.477±0.05 and 0.418±0.04 ns, respectively. Interestingly, the two dominant benefits which are expected from S:Bi_2O_3 incorporation (i.e., reduced recombination and fast charge transport) have competing effects on carrier lifetime, where reduced recombination increases lifetime while fast charge transport reduces it. This may be the reason that lifetime was not found to vary significantly between the two samples. The charge transfer rate constant (k_{ct}) can also be calculated as $k_{ct} = \frac{1}{< \tau >}$.[170] The obtained k_{ct} for WO_3/(Ga,W):$BiVO_4$ and WO_3/S:Bi_2O_3/(Ga,W):$BiVO_4$ were 2.095±0.2 $ns^{-1}$and 2.393±0.22 ns^{-1}, respectively, suggesting that the enhanced charge transfer may be slightly more dominant.

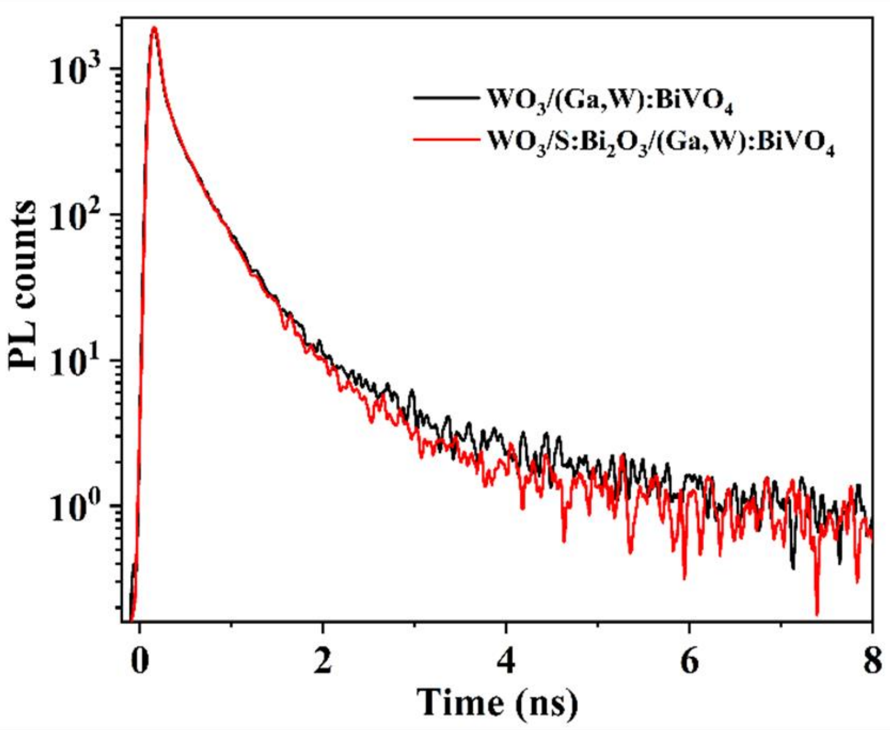

Figure 48 Time-resolved PL emission (excited at λ = 405 nm).

Table 2 Time-resolved PL analysis calculated parameters

Photoanode	A_1	τ_1 (ns)	A_2	τ_2 (ns)	$<\tau>$ (ns)	$K_{et}(ns^{-1})$
WO_3/(Ga,W):$BiVO_4$	646.31±81.42	0.34±0.03	23.88±8.94	1.39±0.24	0.477±0.05	2.095±0.20
WO_3/S:Bi_2O_3/(Ga,W):$BiVO_4$	679.97±90.52	0.31±0.03	37.54±17.41	1.02±0.18	0.418±0.04	2.393±0.22

TA was employed for an in-depth understanding of the charge dynamics behavior across WO_3/(Ga,W):$BiVO_4$ interface without and with the S:Bi_2O_3 interfacial layer by placing the sample in the air and electrolyte (*operando*). First, fs-TA data were collected for in air, pumped at 430 nm and probed in the range 900-1400 nm for WO_3/(Ga,W):$BiVO_4$ and WO_3/S:Bi_2O_3/(Ga,W):$BiVO_4$ samples. It is believed that this infrared probing range tracks the free and trapped photogenerated carriers, while the excitation first strikes the thick (Ga,W):$BiVO_4$ layer and likely predominately produces excited states in this layer. The intensity decay curve plotted in Figure 49a demonstrates faster initial decay on *ps* time scale for the WO_3/(Ga,W):$BiVO_4$ sample compared to WO_3/S:Bi_2O_3/(Ga,W):$BiVO_4$. This fast decay likely corresponds to geminate electron-hole recombination, which is ameliorated with the additional Bi_2O_3 layer, facilitating electron movement away from $BiVO_4$ and suppressing initial recombination. The recorded decay (ΔA) signal was fitted using the exponential decay model $\Delta A = \sum_{i=1}^{n} A_i \exp\left(-\frac{t}{\tau_i}\right)$ Where A_i and τ_i are the amplitude and the lifetime of an exponential decay component, respectively, the calculated fitting parameters are summarized in Table 3, and the values are commensurate with those found in the literature.[150] The fs-TA is the best fit with 3 exponentials in the *ns* regime without an extended component in the microsecond regime due to the absence of electrolyte that stabilizes separated charges. Time constant τ_1, τ_2 and τ_3 can be inferred as loss of excited states due to hole trapping and depletion of the trapped hole due to electron-hole recombination with free and thermalized electrons.[150,171] It is inferred from τ_1 that the initial fast processes leading to carrier loss are reduced in the WO_3/S:Bi_2O_3/(Ga,W):$BiVO_4$ sample, as all decay time constants are slower than for the WO_3/(Ga,W):$BiVO_4$ sample. The subsequent remaining carriers are left to undergo slower interfacial recombination on a *ns* timescale without electrolyte. We note that unlike TRPL, which only measures radiative electron-hole recombination, and thus separation leads to reduced lifetime, the absorptive TA signal represents carrier population, and as such, a persistent signal also indicates carrier motion to avoid recombination.

Next, the ns-TA measurement was conducted with samples submerged in the electrolyte to evaluate hole transfer kinetics at the semiconductor/electrolyte interface. The measurement was conducted at open circuit potential, pumped at 430 nm and probed in the range 900-1400 nm in KPi electrolyte. It was predicted that an electron trap state partially occupied at open circuit potential could exhibit optical transition behavior to a localized trap state.[149] The band bending at the photoanode/electrolyte interface can prolong the photogenerated holes lifetime (μs) and accumulation.[149] This was confirmed by measuring open circuit potential (~0.5 and ~0.55 V_{RHE}) in the dark and flat-band potential (0.092 and 0.041 V_{RHE} (SI section 4)) exhibited significant band bending for WO_3/(Ga,W):$BiVO_4$ and WO_3/S:Bi_2O_3/(Ga,W):$BiVO_4$ photoanodes. From the fs-TA data described above, it is known that a larger number of holes survived the initial electron-hole recombination due to rapid charge separation/transport and subsequent transport to the reactive film surface for the water oxidation reaction.[149,154] Subsequently, from the normalized ns-TA data tracking secondary decays in Figure 49b, it was observed that WO_3/S:Bi_2O_3/(Ga,W):$BiVO_4$ exhibited slightly faster *ns* decay than WO_3/(Ga,W):$BiVO_4$ but otherwise had nearly identical kinetics. The recorded decay signal was fitted using the exponential decay model. The calculated fitting parameters are summarized in Table 4. The ns-TA best fit with 4 exponentials due to the presence of long-lived carriers. The shortest time scale (τ_1) for WO_3/S:Bi_2O_3/(Ga,W):$BiVO_4$ might represent carrier loss due to the initial, more rapid sweeping to the surface as facilitated by the additional layer. The electron extraction (K_{TA}) rate was higher for WO_3/S:Bi_2O_3/(Ga,W):$BiVO_4$ photoanode that denoted the enhanced electron mobility after placing S:Bi_2O_3 layer and impact of S diffusion to adjacent layers.

Correspondingly, the recombination between trapped holes and free electrons (τ_2) on the > 30 ns timescale was similar in WO_3/S:Bi_2O_3/(Ga,W):$BiVO_4$ (36 ns) compared to WO_3/(Ga,W):$BiVO_4$ (43 ns). The recombination of the trapped hole with thermalized electrons (τ_3) was occurring in μs range (1.1 to 1.3 μs) and expected that it would not significantly impact the overall water splitting process.[154] By the time the μs timescale is reached, the leftover carriers surviving recombination have been swept far away from the internal interface, where the composition is distinct between the samples, to the semiconductor/electrolyte interface where composition and thus kinetics become similar. This study provides evidence that the number of long-lived photogenerated charge carriers is improved after adding interfacial layer S:Bi_2O_3. In addition, we conclude that WO_3/S:Bi_2O_3/(Ga,W):$BiVO_4$ decays faster in the < 10 ns regime compared with WO_3/Ga,W):$BiVO_4$, suggesting improved electron transfer rate and accumulation of holes at the (Ga,W):$BiVO_4$ surface for water oxidation kinetics.

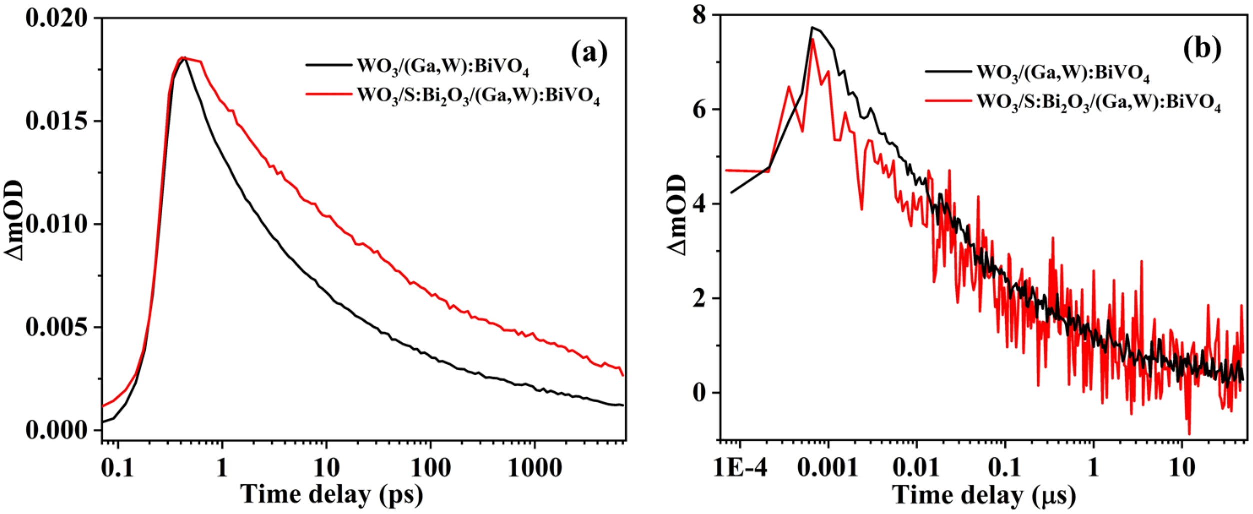

Figure 49 TA spectra collected, pumped at 430 nm probed in the range 900-1400 nm (a) in the air for fs-TA and (b) in KPi electrolyte for ns-TA at an open circuit potential for WO_3/(Ga,W):$BiVO_4$ and WO_3/S:Bi_2O_3/(Ga,W):$BiVO_4$ photoanodes.

Table 3 fs-TA analysis calculated parameters of dry film

	WO_3/(Ga,W):$BiVO_4$		WO_3/S:Bi_2O_3/(Ga,W):$BiVO_4$	
	A	τ (ps)	A	τ (ps)
τ_1	1.06E-02	1.164	1.95E-03	1.947
τ_2	5.50E-03	31.15	1.45E-03	60.45
τ_3	2.96E-03	4640	1.35E-03	8233

Table 4 ns-TA analysis calculated parameters in operando.

	WO_3/(Ga,W):$BiVO_4$			WO_3/S:Bi_2O_3/(Ga,W):$BiVO_4$		
	A	τ (ns)	K_{TA} (ns^{-1})	A	τ (ns)	K_{TA} (ns^{-1})
τ_1	0.43	2.5	0.4	0.35	1.1	0.909
τ_2	0.38	43	0.023	0.37	36	0.0278
τ_3	0.21	1300	0.0008	0.21	1100	0.0009
τ_4	0.07	>100000	<0.00001	0.07	>100000	<0.00001

5.9 Energy band diagram

The primary electrons and holes separation and transfer pathways occurring among three oxides were shown in the band diagram (Figure 50). The CB edge was determined using flat-band potential, considering the negligible difference between the flat-band and bottom of the CB edge.[172] It was assumed that the small amount of S would not significantly change the VBs and CBs position of Bi_2O_3, WO_3 and (Ga,W):$BiVO_4$ layers. Being the main absorber, $BiVO_4$ will absorb low energy photons ($\lambda \leq 530$), while WO_3 ($\lambda \leq 450$) and S:Bi_2O_3 ($\lambda \leq 430$) will absorb high energy photons. Due to the stepped alignment and the appropriate VBs and CBs configurations, electrons can readily transport from the CBs of

$BiVO_4$ into WO_3 via the S:Bi_2O_3 interfacial layer and the current collector.[85,149] Simultaneously, photogenerated holes at WO_3 will transport to and be collected at (Ga,W):$BiVO_4$ through the interfacial S:Bi_2O_3 layer.

The time scales for charge separation and transport from TRPL, fs- and ns-TA analysis indicate that more holes are directed to the reactive surface on the *ps-ns* range in (Ga,W):$BiVO_4$. Subsequently, photogenerated electrons will transfer from S:Bi_2O_3 into WO_3 on a *ns-μs* time scale. Recombination of photoexcited free electrons in (Ga,W):$BiVO_4$ is reduced by being transferred into the CB of WO_3 via the S:Bi_2O_3 layer. Once in the WO_3, the electrons have a longer lifetime.[148] In this process S:Bi_2O_3 play a key role in facilitating rapid charge transfer initially to WO_3 to improve the photoactivity of WO_3/S:Bi_2O_3/(Ga,W):$BiVO_4$ photoanode. Furthermore, the backflow of charge carriers within the photoanode is reduced by the CBs and VBs energy barriers present among the WO_3, S:Bi_2O_3 and (Ga,W):$BiVO_4$ layers that suppress holes and electron backflow.[33,34,35]

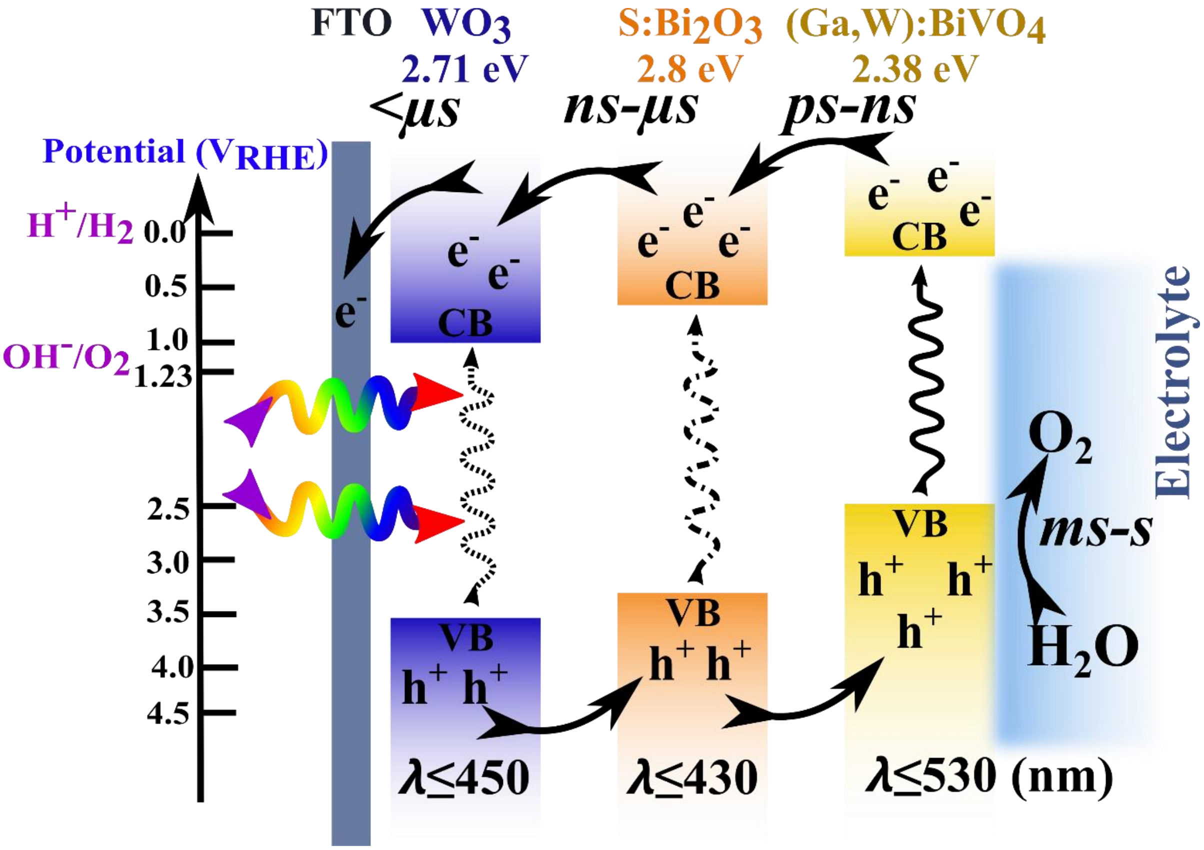

Figure 50 Schematic of band alignment for WO_3/S:Bi_2O_3/(Ga,W):$BiVO_4$ heterojunction illustrating photoactivated charge generation, transfer process and related time scale.

5.10 Electrochemical stability and hydrogen measurement

As observed from Figure 51a, the photocurrent of all photoanodes decreases initially due to dominating photocorrosion of (Ga,W):$BiVO_4$ from the loss of V^{5+} ions in the form of V_2O_5. However, the photocurrent further ameliorates when V_2O_5 dissolution gets saturated[176] as it can be observed for WO_3/(Ga,W):$BiVO_4$ photoanode, which could retain ~60% of the initial photocurrent. Further, the effect of interfacial layer Bi_2O_3 and S:Bi_2O_3

get more pronounced in ameliorating the charge dynamics and photocatalytic performance for WO_3/Bi_2O_3/(Ga,W):$BiVO_4$ and WO_3/S:Bi_2O_3/(Ga,W):$BiVO_4$ photoanodes by retaining ~80 and ~85 % of the initial photocurrent. Consequently, adding a protective layer Co-Pi demonstrate self-healing nature and WO_3/S:Bi_2O_3/(Ga,W):$BiVO_4$/Co-Pi photoanode performance improve by retaining 90% of the photocurrent density compared to ~85% for WO_3/S:Bi_2O_3/(Ga,W):$BiVO_4$ photoanode after 10 h.[85] The repeatability of photoanodes after stability measurement demonstrated no significant change in the photocurrent onset and PCD at 1.23 V_{RHE}. The amount of H_2 and O_2 gases generated was measured to verify the faradaic efficiency of each water splitting half-reaction. The measurement was performed for the WO_3/S:Bi_2O_3/(Ga,W):$BiVO_4$/Co-Pi photoanode at 1.23 V_{RHE} under simulated AM 1.5G illumination in KPi electrolyte. Figure 51b shows the H_2 and O_2 gas generation rate (67.3 and 33.6 μmol.$h^{-1}cm^{-2}$, respectively) along with the theoretical production rate and the corresponding faradaic efficiency (secondary Y-axis in Figure 51b) values (91.5 and 88%, respectively) The slightly lower values of faradaic efficiency are attributed to inhibition of proton reduction, diffusion of H_2 gases, and potential back reactions at counter electrode from dissolved O_2.[22,23]

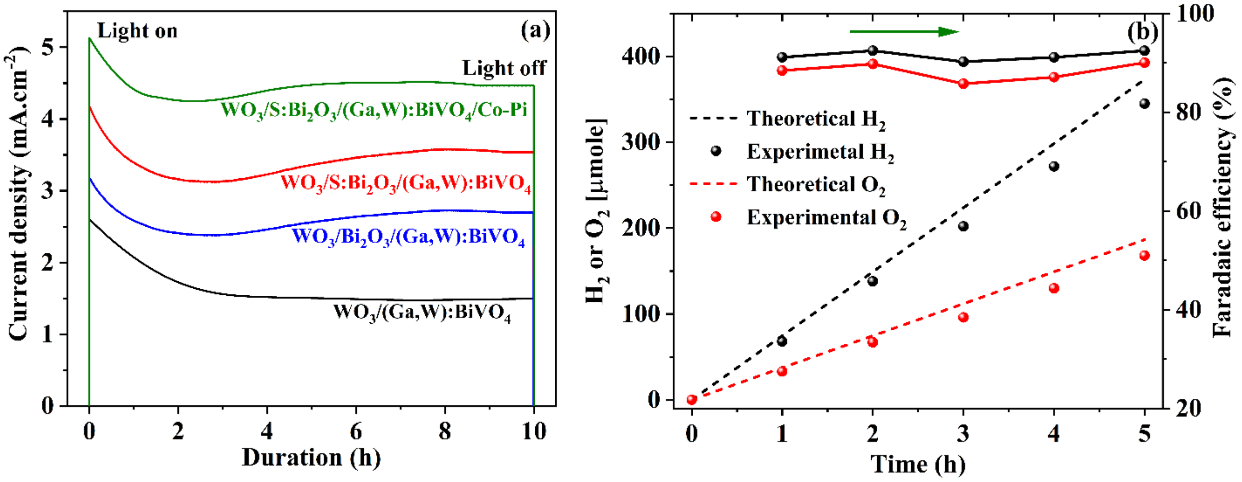

Figure 51 (a) Photoelectrochemical stability measurements of photoanodes with WO_3 heterojunction and Bi_2O_3 interface layer without and with sulfur modification. (b) Evolution of H_2 and O_2 gases for $WO_3/S:Bi_2O_3/(Ga,W):BiVO_4/Co$-Pi photoanode. *The measurements were conducted at 1.23* V_{RHE} *in KPi electrolyte under simulated AM 1.5G illumination.*

5.11 Conclusion

The performance of photoanodes containing a $WO_3/BiVO_4$ heterojunction is limited, in part, by charge separation, transfer and recombination across the heterojunction interface. To mitigate these losses, sulfur modified Bi_2O_3 interfacial layer was introduced between WO_3 and $BiVO_4$ layers. The $BiVO_4$ layer was optimized with co-doping at Bi^{3+} and V^{5+} sites by Ga^{3+} and W^{6+}, respectively, to improve the light absorption and photogenerated charge carrier extraction. The $S:Bi_2O_3$ layer between WO_3 and $(Ga,W):BiVO_4$ and Co-Pi co-catalyst led to achieving 5.1±0.25 mA.cm^{-2} and 67.3 µmol.h^{-1}cm^{-2} photocurrent density and hydrogen collection rate for $WO_3/S:Bi_2O_3/(Ga,W):BiVO_4/Co$-Pi photoanode. EDAX, XPS and TOF-SIMS depth profiling corroborated the uniform diffusion of S in all layers, whereas EIS and TRPL confirmed the enhanced interfacial charge transfer kinetics. Subsequently, *operando* fs- and ns-TA analysis concluded that more long-lived photogenerated charge carriers remain after adding S:Bi_2O_3 interfacial layer, providing more holes directed to the reactive surface due to effective charge separation/transfer and improved the overall photoanode performance. As a result, the photocurrent density and hydrogen production rates are among the highest reported for interlayer enhanced WO_3/$BiVO_4$ heterojunction photoanodes.

CHAPTER 6 SUMMARY AND OUTLOOK

Non-renewable hydrogen production methods can serve as a temporary supply for the hydrogen economy, various renewable strategies are being developed to enable hydrogen production, which is predictable to be comprehended as soon as possible before permanent damage is done onto the environment by a fossil fuel-based system. It is estimated that the low cost, environmentally friendly photocatalytic water splitting is a contemporary approach for hydrogen production. It will play a vital role in hydrogen production and contribute much to the coming hydrogen economy. Overall, hydrogen generation through solar pathways is an ideal and long-term approach for producing green energy, but the involved process is complex and requires a highly efficient system to achieve decent solar to hydrogen efficiency.

The photoelectrochemical method is a promising solar pathway for hydrogen production. The scheelite monoclinic structure of $BiVO_4$ was selected as one of the most suitable photoanode materials for the photoelectrochemical water splitting producing green H_2 due to its crystal and electronic structures. However, being a limited light absorber, $BiVO_4$ faces various challenges such as positive CB position, substantial electron-hole recombination, and the poorly catalytic properties towards O_2 evolution. To address these challenges, various methods such as synthesis/fabrication methods, doping with metal and non-metal, heterojunction formation with metal oxide and OER surface catalysts have been discussed in detail. Additional improvements include reducing excessive recombination at the surface by generating efficient physical charge separation by compositional tuning, coupling with efficient semiconductor material for heterojunction formation and efficient oxygen evolution catalyst for transferring almost 100% holes to the reactant surface. Increasing light absorption without simultaneously generating trap sites is another challenge that needs to be addressed. Notably, factors such as electronic properties, chemical composition, structure, crystallinity, surface states and morphology of catalysts need to be carefully considered to tune and determine their photocatalytic activity for drastically improving hydrogen production efficiency in practical applications. This dissertation discussed the four major approaches to enhance the charge dynamics.

Thin films were prepared by ultrasonic spray coating and atmospheric pressure chemical vapor deposition (ALCVD). First, the alkali metal was placed in the crystal structure of $BiVO_4$ and extended light absorption for Li:$BiVO_4$ and Na:$BiVO_4$ compared to K:$BiVO_4$ and pristine $BiVO_4$. The XRD and Raman results indicated that alkali metal occupied the interstitial position of the $BiVO_4$ lattice structure. The diffusion length of charge particles was measured by implementing a positron at the surface of the thin films and found that the diffusion length of the positron increased by ~ 4 times in Na:$BiVO_4$ and Li:$BiVO_4$ compared to that of the pristine. It was also observed that the Bi and V based defect density was minimum on alkali metal placement in the $BiVO_4$ crystal structure. The *ab initio* DFT calculations confirmed that the Li and Na doping in the $BiVO_4$ interstitial site was energetically the most favorable position. It was evident that oxygen atoms formed weak bonds with Li and Na atoms, and multiple internbands formed between conduction and valence band, leading to more interactions and a small reduction in the bandgap in improving charge dynamics Na:$BiVO_4$ and Li:$BiVO_4$.

Second, the doping of the rare earth metal ions Y^{3+} Er^{3+} or Yb^{3+} at Bi^{3+} and W^{6+} doped at V^{5+} site to enhances light absorption ($\lambda \leq 550$) due to reduction in bandgap and increased charge transport property compared to intrinsic $BiVO_4$ photoanode. The third approach introduced junction formation to enhance the light harnessing in the wide spectrum. Type II heterojunction with WO_3 and *p-n* junction form with Fe:NiO for efficient electron transfer and enhancing charge dynamics. The WO_3/(Y,W):$BiVO_4$/Fe:NiO photoanode with type two heterojunction and the *p-n* junction with Fe:NiO demonstrated near-complete (~95 %) suppression of electrons and holes recombination, efficient charge transfer (~75 %) and improved absorption efficiency (~85 %). Due to the *p–n* junction formed between the interface of WO_3/(Y,W):$BiVO_4$ or WO_3/(Er,W):$BiVO_4$ with Fe-NiO, an inner electric field is built, enhancing the surface reaction kinetics (transportation of electron-hole pairs), lowering the band bending conditions, and increasing the bulk charge separation. Thus, rare earth metal Y or Er or Yb doing along with W in $BiVO_4$ enhances light absorption but leads to decreased bulk and surface charge transport property and this limitation can be overcome by using a suitable electron/hole transfer layer.

Finally, it was detected that the performance of photoanodes containing a WO_3/$BiVO_4$ heterojunction is limited, in part, by charge separation, transfer and recombination across the heterojunction interface. To mitigate these losses, sulfur modified Bi_2O_3 interfacial layer was introduced between WO_3 and $BiVO_4$ layers. The $BiVO_4$ layer was optimized with dual co-doping to improve the light absorption and photogenerated charge carrier extraction. The S:Bi_2O_3 layer between WO_3 and (Ga,W):$BiVO_4$ and Co-Pi co-catalyst led to achieving 5.1±0.25 $mA.cm^{-2}$ and 67.3 $\mu mol.h^{-1}cm^{-2}$ photocurrent density and hydrogen collection rate for WO_3/S:Bi_2O_3/(Ga,W):$BiVO_4$/Co-Pi photoanode. EDAX, XPS and TOF-

SIMS depth profiling corroborated the uniform diffusion of S in all layers, whereas EIS and TRPL confirmed the enhanced interfacial charge transfer kinetics. Subsequently, *operando* fs- and ns-TA analysis concluded that more long-lived photogenerated charge carriers remain after adding S:Bi_2O_3 interfacial layer, providing more holes directed to the reactive surface due to effective charge separation/transfer and improved the overall photoanode performance. The photocurrent density and hydrogen production rates are the highest reported for interlayer enhanced WO_3/$BiVO_4$ heterojunction photoanodes.

Unquestionably, the charge kinetics of photocatalysts is a complex phenomenon as it involves multiple steps and mechanisms. While the existing mechanisms are proposed primarily based on the theories and the experimental data derived from several state-of-the-art characterization techniques, an in-depth understanding of charge kinetics is often constrained by the limitations of the characterization techniques and real-life experimental conditions. State-of-the-art characterization techniques with high spatial, temporal and spectral resolutions are essential for *in situ* and direct observations of charge kinetics concerning the morphological, compositional, electronic changes and charge dynamics of a photocatalyst. Subsequently, given the multidisciplinary field, integrating materials science, electrochemistry, physical chemistry and surface science, the collaboration between researchers across multiple disciplines is required to understand the system for developing a new and effective photocatalytic process. Till now, the highest reproducible STH energy conversion efficiency value achieved using the particulate photocatalytic system is far lower than values obtained with photovoltaic-electrolysis systems and photoelectrochemical devices.[72,72,182] Considering the simple construction of industrial-scale solar hydrogen production facilities based on particulate photocatalytic overall water splitting systems, an STH energy conversion efficiency of ~ 5 – 8 % will be a decent starting point for practical applications. Therefore, improving the efficiency of present-day narrow bandgap photocatalysts and developing novel nanostructured active materials capable of harnessing red or near-infrared light are still the prime challenges. Based on the research discussed in this thesis and photocurrent summarized in the Table 5, all the implemented methods are well characterized and validated. However, the developed sulfur modified interfacial layer is the most suitable and recommended strategy to improve the photocatalytic efficiency of $BiVO_4$. The comprehensive refinement of photocatalyst materials to accentuate surface properties and fine-tuning reaction conditions is also necessary.[72,183] Moreover, ongoing investigations regarding restricted systems will be required. In general, attempts inspired from a wide range of scientific areas will be highly desired to allow future innovations in the advancement of overall water splitting efficiency to recognize the ‘‘Holy Grail’’ of artificial photosynthesis soon as possible.[155,177]

Table 5 Photoanodes and respective photocurrent at 1.23 V_{RHE} under 1 sun illumination.

Strategy	Photoanodes	Photocurrent at 1.23V_{RHE} ($mA.cm^{-2}$)
Alkali metal doping	$BiVO_4$	0.2 ± 0.01
	$K:BiVO_4$	0.7 ± 0.02
	$Na:BiVO_4$	1.75 ± 0.09
	$Li:BiVO_4$	2.2 ± 0.1
W doping at V^{5+}site	$Bi_{0.987}V_{0.992}W_{0.013}O_4$	1.2 ± 0.08
	$BiV_{0.97}W_{0.013}O_4$	1.9 ± 0.1
	$BiV_{0.992}W_{0.013}O_4$	2.4 ± 0.12
Rare earth metal doping at Bi^{3+}site	$Yb:BiVO_4$	0.3 ± 0.02
	$Ga:BiVO_4$	0.25 ± 0.01

	Er:$BiVO_4$	0.4 ± 0.02
	Y:$BiVO_4$	0.6 ± 0.02
Dual doping at Bi^{3+} and V^{5+} sites	(Yb,W):$BiVO_4$	1.9 ± 0.1
	(Ga,W):$BiVO_4$	1.8 ± 0.1
	(Er,W):$BiVO_4$	2.3 ± 0.12
	(Y,b):$BiVO_4$	2.6 ± 0.12
Heterojunction formation with WO_3	WO_3/(Yb,W):$BiVO_4$	4.5 ± 0.2
	WO_3/(Er,W):$BiVO_4$	4.3 ± 0.2
	WO_3/(Y,b):$BiVO_4$	2.6 ± 0.12
p-*n* junction formation	WO_3/(Er,W):$BiVO_4$/Fe:NiO	5.6 ± 0.2
	WO_3/(Y,b):$BiVO_4$/Fe:NiO	5.8 ± 0.3
Interfacial layer S:Bi_2O_3	WO_3/(Ga,W):$BiVO_4$	2.4 ± 0.12
	WO_3/Bi_2O_3/(Ga,W):$BiVO_4$	3.2 ± 0.2
	WO_3/S:Bi_2O_3/(Ga,W):$BiVO_4$	4.2 ± 0.2

REFERENCES

(1) Abdi, F. F. Towards Highly Efficient Bias-Free Solar Water Splitting. Ph.D. Thesis, Delft University of Technology, Delft, The Netherlands, 2013

(2) U.S. EIA. Annual Energy Outlook 2019 with Projections to 2050. *Annu. Energy Outlook 2019 with Proj. to 2050* **2019**, *44*, 1–64.

(3) Esterly, S. 2013 Renewable Energy Data Book (Book), NREL (National Renewable Energy Laboratory). **2013**.

(4) Feldman, D.; Margolis, R. Q4 2018 / Q1 2019 Solar Industry Update. **2018**, No. May.

(5) Tuller, H. L. *Electronic Materials : Science & Technology*.

(6) Pinnangudi, B.; Kuykendal, M.; Bhadra, S. *Smart Grid Energy Storage*; Elsevier Ltd, 2017.

(7) Abdi, H.; Mohammadi-ivatloo, B.; Javadi, S.; Khodaei, A. R.; Dehnavi, E. *Energy Storage Systems*; Elsevier Inc., 2017.

(8) Tuller, H. L. Solar to Fuels Conversion Technologies: A Perspective. *Mater. Renew. Sustain. Energy* **2017**, *6*, 1–16.

(9) de Miranda, P. E. V. *Hydrogen Energy: Sustainable and Perennial*; 2019.

(10) Zhang, P.; Wang, T.; Gong, J. Current Mechanistic Understanding of Surface Reactions over Water-Splitting Photocatalysts. *Chem* **2018**, *4*, 223–245.

(11) Ager, J. W.; Shaner, M. R.; Walczak, K. A.; Sharp, I. D.; Ardo, S. Experimental Demonstrations of Spontaneous, Solar-Driven Photoelectrochemical Water Splitting. *Energy Environ. Sci.* **2015**, *8*, 2811–2824.

(12) Osterloh, F. E. Inorganic Materials as Catalysts for Photochemical Splitting of Water. *Chem. Mater.* **2008**, *20*, 35–54.

(13) Kim, J. H.; Hansora, D.; Sharma, P.; Jang, J. W.; Lee, J. S. Toward Practical Solar Hydrogen Production-an Artificial Photosynthetic Leaf-to-Farm Challenge. *Chem. Soc. Rev.* **2019**, *48*, 1908–1971.

(14) Walter, M. G.; Warren, E. L.; McKone, J. R.; Boettcher, S. W.; Mi, Q.; Santori, E. A.; Lewis, N. S. Solar Water Splitting Cells. *Chem. Rev.* **2010**, *110*, 6446–6473.

(15) Woodhouse, M.; Parkinson, B. A. Combinatorial Approaches for the Identification and Optimization of Oxide Semiconductors for Efficient Solar Photoelectrolysis. *Chem. Soc. Rev.* **2009**, *38*, 197–210.

(16) Gr, M. PECreview. *Nature* **2001**, *414*, 338–344.

(17) Li, X.; Yu, J.; Low, J.; Fang, Y.; Xiao, J.; Chen, X. Engineering Heterogeneous

Semiconductors for Solar Water Splitting. *J. Mater. Chem. A* **2015**, *3*, 2485–2534.

(18) Part 1 Fundamental Aspects of Photocatalysis. 1–28.

(19) Al-Hilli, S.; Willander, M. The PH Response and Sensing Mechanism of N-Type ZnO/Electrolyte Interfaces. *Sensors* **2009**, *9*, 7445–7480.

(20) Bolts, J. M.; Wrighton, M. S. Correlation of Photocurrent-Voltage Curves with Flat-Band Potential for Stable Photoelectrodes for the Photoelectrolysis of Water. *J. Phys. Chem.* **1976**, *80*, 2641–2645.

(21) Yong, X.; Schoonen, M. A. A. The Absolute Energy Positions of Conduction and Valence Bands of Selected Semiconducting Minerals. *Am. Mineral.* **2000**, *85*, 543–556.

(22) Guijarro, N.; Prévot, M. S.; Sivula, K. Surface Modification of Semiconductor Photoelectrodes. *Phys. Chem. Chem. Phys.* **2015**, *17*, 15655–15674.

(23) Nozik, A. J. PHOTOELECTROCHEMISTR Y : CONVERSION. **1978**, 189–222.

(24) Smith, W. A.; Sharp, I. D.; Strandwitz, N. C.; Bisquert, J. Interfacial Band-Edge Energetics for Solar Fuels Production. *Energy Environ. Sci.* **2015**, *8*, 2851–2862.

(25) Nozik, A. J.; Memming, R. Physical Chemistry of Semiconductor-Liquid Interfaces. *J. Phys. Chem.* **1996**, *100*, 13061–13078.

(26) Walter, M. G.; Warren, E. L.; McKone, J. R.; Boettcher, S. W.; Mi, Q.; Santori, E. A.; Lewis, N. S. Solar Water Splitting Cells. *Chem. Rev.* **2010**, *110*, 6446–6473.

(27) Heller, A. Conversion of Sunlight into Electrical Power and Photoassisted Electrolysis of Water in Photoelectrochemical Cells. *Acc. Chem. Res.* **1981**, *14*, 154–162.

(28) Fountaine, K. T.; Lewerenz, H. J.; Atwater, H. A. Efficiency Limits for Photoelectrochemical Water-Splitting. *Nat. Commun.* **2016**, *7*, 1–9.

(29) Fang, W.; Shangguan, W. A Review on Bismuth-Based Composite Oxides for Photocatalytic Hydrogen Generation. *Int. J. Hydrogen Energy* **2019**, *44*, 895–912.

(30) Martinez Suarez, C.; Hernández, S.; Russo, N. BiVO4 as Photocatalyst for Solar Fuels Production through Water Splitting: A Short Review. *Appl. Catal. A Gen.* **2015**, *504*, 158–170.

(31) Tee, S. Y.; Win, K. Y.; Teo, W. S.; Koh, L. D.; Liu, S.; Teng, C. P.; Han, M. Y. Recent Progress in Energy-Driven Water Splitting. *Adv. Sci.* **2017**, *4*.

(32) Rahimi, N.; Pax, R. A.; Gray, E. M. A. Review of Functional Titanium Oxides. I: TiO2 and Its Modifications. *Prog. Solid State Chem.* **2016**, *44*, 86–105.

(33) Prasad, U.; Prakash, J.; Kannan, A. M. Effects of Yttrium, Ytterbium with Tungsten Co-Doping on the Light Absorption and Charge Transport Properties of Bismuth Vanadate Photoanodes to Achieve Superior Photoelectrochemical Water Splitting.

Sustain. Energy Fuels **2020**, *4*, 1496–1506.

(34) Sharma, P.; Jang, J. W.; Lee, J. S. Key Strategies to Advance the Photoelectrochemical Water Splitting Performance of α-Fe2O3 Photoanode. *ChemCatChem* **2019**, *11*, 157–179.

(35) Kegel, J.; Povey, I. M.; Pemble, M. E. Zinc Oxide for Solar Water Splitting: A Brief Review of the Material's Challenges and Associated Opportunities. *Nano Energy* **2018**, *54*, 409–428.

(36) Prasad, U.; Prakash, J.; Azeredo, B.; Kannan, A. Stoichiometric and Non-Stoichiometric Tungsten Doping Effect in Bismuth Vanadate Based Photoactive Material for Photoelectrochemical Water Splitting. *Electrochim. Acta* **2019**, *299*, 262–272.

(37) Bagal, I. V.; Chodankar, N. R.; Hassan, M. A.; Waseem, A.; Johar, M. A.; Kim, D. H.; Ryu, S. W. Cu2O as an Emerging Photocathode for Solar Water Splitting - A Status Review. *Int. J. Hydrogen Energy* **2019**, *44*, 21351–21378.

(38) Valenti, M.; Dolat, D.; Biskos, G.; Schmidt-Ott, A.; Smith, W. A. Enhancement of the Photoelectrochemical Performance of CuWO4 Thin Films for Solar Water Splitting by Plasmonic Nanoparticle Functionalization. *J. Phys. Chem. C* **2015**, *119*, 2096–2104.

(39) Díez-García, M. I.; Gómez, R. Investigating Water Splitting with CaFe2O4 Photocathodes by Electrochemical Impedance Spectroscopy. *ACS Appl. Mater. Interfaces* **2016**, *8*, 21387–21397.

(40) Kim, J. H.; Jang, Y. J.; Choi, S. H.; Lee, B. J.; Kim, J. H.; Park, Y. Bin; Nam, C. M.; Kim, H. G.; Lee, J. S. A Multitude of Modifications Strategy of ZnFe2O4 Nanorod Photoanodes for Enhanced Photoelectrochemical Water Splitting Activity. *J. Mater. Chem. A* **2018**, *6*, 12693–12700.

(41) Li, J.; Griep, M.; Choi, Y.; Chu, D. Photoelectrochemical Overall Water Splitting with Textured CuBi2O4 as a Photocathode. *Chem. Commun.* **2018**, *54*, 3331–3334.

(42) Sivula, K.; Van De Krol, R. Semiconducting Materials for Photoelectrochemical Energy Conversion. *Nat. Rev. Mater.* **2016**, *1*.

(43) Cheng, X.; Ding, J.; Wu, Y.; Liu, H.; Dawson, G. The Photocathodic Properties of a Fe2O3 Wrapped CuFeO2 Layer on ITO Glass for Water Splitting. *Chem. Phys.* **2018**, *513*, 241–245.

(44) Leach, A. D. P.; Macdonald, J. E. Optoelectronic Properties of CuInS2 Nanocrystals and Their Origin. *J. Phys. Chem. Lett.* **2016**, *7*, 572–583.

(45) Bown, J. J.; Page, A. J. Vacancy Diffusion Barriers in TaON and Ta3N5 Water-Splitting Photocatalysts. *J. Mater. Chem. A* **2019**, *7*, 13029–13035.

(46) Murthy, D. H. K.; Matsuzaki, H.; Wang, Z.; Suzuki, Y.; Hisatomi, T.; Seki, K.; Inoue, Y.; Domen, K.; Furube, A. Origin of the Overall Water Splitting Activity of

Ta3N5 Revealed by Ultrafast Transient Absorption Spectroscopy. *Chem. Sci.* **2019**, *10*, 5353–5362.

(47) Seo, J.; Nakabayashi, M.; Hisatomi, T.; Shibata, N.; Minegishi, T.; Domen, K. Solar-Driven Water Splitting over a BaTaO2N Photoanode Enhanced by Annealing in Argon. *ACS Appl. Energy Mater.* **2019**, *2*, 5777–5784.

(48) Hisatomi, T.; Katayama, C.; Moriya, Y.; Minegishi, T.; Katayama, M.; Nishiyama, H.; Yamada, T.; Domen, K. Photocatalytic Oxygen Evolution Using BaNbO2N Modified with Cobalt Oxide under Photoexcitation up to 740 Nm. *Energy Environ. Sci.* **2013**, *6*, 3595–3599.

(49) Rajeshwar, K.; Bhattacharya, R. N. ELECTRODEPOSITION OF CdTe THIN FILMS. *Electrochem. Soc. Ext. Abstr.* **1984**, *84–2*, 616.

(50) Yu, S.; Fan, X. B.; Wang, X.; Li, J.; Zhang, Q.; Xia, A.; Wei, S.; Wu, L. Z.; Zhou, Y.; Patzke, G. R. Efficient Photocatalytic Hydrogen Evolution with Ligand Engineered All-Inorganic InP and InP/ZnS Colloidal Quantum Dots. *Nat. Commun.* **2018**, *9*, 1–10.

(51) Garner, L. E.; Steirer, K. X.; Young, J. L.; Anderson, N. C.; Miller, E. M.; Tinkham, J. S.; Deutsch, T. G.; Sellinger, A.; Turner, J. A.; Neale, N. R. Covalent Surface Modification of Gallium Arsenide Photocathodes for Water Splitting in Highly Acidic Electrolyte. *ChemSusChem* **2017**, *10*, 767–773.

(52) Ebaid, M.; Min, J. W.; Zhao, C.; Ng, T. K.; Idriss, H.; Ooi, B. S. Water Splitting to Hydrogen over Epitaxially Grown InGaN Nanowires on a Metallic Titanium/Silicon Template: Reduced Interfacial Transfer Resistance and Improved Stability to Hydrogen. *J. Mater. Chem. A* **2018**, *6*, 6922–6930.

(53) Jiang, C.; Moniz, S. J. A.; Wang, A.; Zhang, T.; Tang, J. Photoelectrochemical Devices for Solar Water Splitting-Materials and Challenges. *Chem. Soc. Rev.* **2017**, *46*, 4645–4660.

(54) Van Dorp, D. H.; Hijnen, N.; Vece, M. Di; Kelly, J. J. Sic: A Photocathode for Water Splitting and Hydrogen Storage. *Angew. Chemie - Int. Ed.* **2009**, *48*, 6085–6088.

(55) Lin, Y.; Battaglia, C.; Boccard, M.; Hettick, M.; Yu, Z.; Ballif, C.; Ager, J. W.; Javey, A. Amorphous Si Thin Film Based Photocathodes with High Photovoltage for Efficient Hydrogen Production. *Nano Lett.* **2013**, *13*, 5615–5618.

(56) Kudo, A.; Ueda, K.; Kato, H.; Mikami, I. Photocatalytic O2 Evolution under Visible Light Irradiation on BiVO4 in Aqueous AgNO3 Solution. *Catal. Letters* **1998**, *53*, 229–230.

(57) Prakash, J.; Prasad, U.; Alexander, R.; Bahadur, J.; Dasgupta, K.; Kannan, A. N. M. Photoelectrochemical Solar Water Splitting: The Role of the Carbon Nanomaterials in Bismuth Vanadate Composite Photoanodes toward Efficient Charge Separation and Transport. *Langmuir* **2019**, *35*, 14492–14504.

(58) Abdi, F. F.; Han, L.; Smets, A. H. M.; Zeman, M.; Dam, B.; Van De Krol, R. Efficient Solar Water Splitting by Enhanced Charge Separation in a Bismuth Vanadate-Silicon Tandem Photoelectrode. *Nat. Commun.* **2013**, *4*, 1–7.

(59) Ullah, H.; Tahir, A. A.; Mallick, T. K. Structural and Electronic Properties of Oxygen Defective and Se-Doped p-Type BiVO4(001) Thin Film for the Applications of Photocatalysis. *Appl. Catal. B Environ.* **2018**, *224*, 895–903.

(60) Seabold, J. A.; Choi, K. S. Efficient and Stable Photo-Oxidation of Water by a Bismuth Vanadate Photoanode Coupled with an Iron Oxyhydroxide Oxygen Evolution Catalyst. *J. Am. Chem. Soc.* **2012**, *134*, 2186–2192.

(61) Prasad, U.; Prakash, J.; Gupta, S. K.; Zuniga, J.; Mao, Y.; Azeredo, B.; Kannan, A. N. M. Enhanced Photoelectrochemical Water Splitting with Er- and W-Codoped Bismuth Vanadate with WO3 Heterojunction-Based Two-Dimensional Photoelectrode. *ACS Appl. Mater. Interfaces* **2019**, *11*, 19029–19039.

(62) Bhat, S. S. M.; Jang, H. W. Recent Advances in Bismuth-Based Nanomaterials for Photoelectrochemical Water Splitting. *ChemSusChem* **2017**, *10*, 3001–3018.

(63) Prasad, U.; Prakash, J.; Azeredo, B.; Kannan, A. Light Absorption Management by Systematic Ytterbium Doping in Monoclinic BiVO4 for Enhancement in Photoelectrochemical Water Oxidation. In *ABSTRACTS OF PAPERS OF THE AMERICAN CHEMICAL SOCIETY*; AMER CHEMICAL SOC 1155 16TH ST, NW, WASHINGTON, DC 20036 USA, 2019; Vol. 257.

(64) Prakash, J.; Prasad, U.; Azeredo, B.; Kannan, A. Does Doping/Co-Doping of Rare Earth Metal in BiVO4 System Lead to Enhanced Photoelectrochemical Water Oxidation: Electrochemical Investigation. In *ABSTRACTS OF PAPERS OF THE AMERICAN CHEMICAL SOCIETY*; AMER CHEMICAL SOC 1155 16TH ST, NW, WASHINGTON, DC 20036 USA, 2019; Vol. 258.

(65) Huang, Z. F.; Pan, L.; Zou, J. J.; Zhang, X.; Wang, L. Nanostructured Bismuth Vanadate-Based Materials for Solar-Energy-Driven Water Oxidation: A Review on Recent Progress. *Nanoscale* **2014**, *6*, 14044–14063.

(66) Prasad, U.; Prakash, J.; Azeredo, B.; Kannan, A. Electrochemical Investigation of the Effect of Graphitic Carbon Nitride Addition in BiVO4 to Improve Photoelectrochemical Water Oxidation Performance. In *ABSTRACTS OF PAPERS OF THE AMERICAN CHEMICAL SOCIETY*; AMER CHEMICAL SOC 1155 16TH ST, NW, WASHINGTON, DC 20036 USA, 2019; Vol. 258.

(67) Qurashi, M. M.; Barnes, W. H. A Preliminary Structure for Pucherite, BiVO4. *Am. Mineral.* **1952**, *37*, 423–426.

(68) Zhou, D.; Pang, L. X.; Wang, D. W.; Reaney, I. M. BiVO4 Based High: K Microwave Dielectric Materials: A Review. *J. Mater. Chem. C* **2018**, *6*, 9290–9313.

(69) Li, G.; Bai, Y.; Zhang, W. F. Difference in Valence Band Top of BiVO 4 with Different Crystal Structure. *Mater. Chem. Phys.* **2012**, *136*, 930–934.

(70) Qurashi, M. M.; Barnes, W. H. A Preliminary Structure for Pucherite, BiVO4. *Am. Mineral.* **1952**, *37*, 423–426.

(71) Tokunaga, S.; Kato, H.; Kudo, A. Selective Preparation of Monoclinic and Tetragonal BiVO4 with Scheelite Structure and Their Photocatalytic Properties. *Chem. Mater.* **2001**, *13*, 4624–4628.

(72) Park, Y.; McDonald, K. J.; Choi, K. S. Progress in Bismuth Vanadate Photoanodes for Use in Solar Water Oxidation. *Chem. Soc. Rev.* **2013**, *42*, 2321–2337.

(73) Kudo, A.; Omori, K.; Kato, H. A Novel Aqueous Process for Preparation of Crystal Form-Controlled and Highly Crystalline BiVO4 Powder from Layered Vanadates at Room Temperature and Its Photocatalytic and Photophysical Properties. *J. Am. Chem. Soc.* **1999**, *121*, 11459–11467.

(74) Meng, X.; Zhang, Z. Bismuth-Based Photocatalytic Semiconductors: Introduction, Challenges and Possible Approaches. *J. Mol. Catal. A Chem.* **2016**, *423*, 533–549.

(75) Zhong, D. K.; Choi, S.; Gamelin, D. R. Near-Complete Suppression of Surface Recombination in Solar Photoelectrolysis by "Co-Pi" Catalyst-Modified W:BiVO4. *J. Am. Chem. Soc.* **2011**, *133*, 18370–18377.

(76) Abdi, F. F.; Han, L.; Smets, A. H. M.; Zeman, M.; Dam, B.; Van De Krol, R. Efficient Solar Water Splitting by Enhanced Charge Separation in a Bismuth Vanadate-Silicon Tandem Photoelectrode. *Nat. Commun.* **2013**, *4*, 1–7.

(77) Shi, Q.; Murcia-López, S.; Tang, P.; Flox, C.; Morante, J. R.; Bian, Z.; Wang, H.; Andreu, T. Role of Tungsten Doping on the Surface States in BiVO4Photoanodes for Water Oxidation: Tuning the Electron Trapping Process. *ACS Catal.* **2018**, *8*, 3331–3342.

(78) Abdi, F. F.; Firet, N.; vandeKrol, R. Efficient BiVO4 Thin Film Photoanodes Modified with Cobalt Phosphate Catalyst and W-Doping. *ChemCatChem* **2013**, *5*, 490–496.

(79) Xia, L.; Bai, J.; Li, J.; Zeng, Q.; Li, X.; Zhou, B. A Highly Efficient BiVO4/WO3/W Heterojunction Photoanode for Visible-Light Responsive Dual Photoelectrode Photocatalytic Fuel Cell. *Appl. Catal. B Environ.* **2016**, *183*, 224–230.

(80) Lind, A. G.; Aldridge, H. L.; Hatem, C.; Law, M. E.; Jones, K. S. Review—Dopant Selection Considerations and Equilibrium Thermal Processing Limits for n $^{+}$ -In $_{0.}$ 53Ga $_{0.47}$ As. *ECS J. Solid State Sci. Technol.* **2016**, *5*, Q125–Q131.

(81) Jovic, V.; Rettie, A. J. E.; Singh, V. R.; Zhou, J.; Lamoureux, B.; Mullins, C. B.; Bluhm, H.; Smith, K. E. Localization and Transport in Tungsten Doped Bismuth Vanadate Single Crystals †. **2016**, *1*, 31958–31965.

(82) Pal, M.; Pal, U.; Silva Gonzalez, R.; Sanchez Mora, E.; Santiago, P. Synthesis and Photocatalytic Activity of Yb Doped TiO_2 Nanoparticles under Visible Light. *J. Nano Res.* **2009**, *5*, 193–200.

(83) Kaur, N.; Sharma, S. K.; Kim, D. Y.; Singh, N. Highly Transparent and Lower Resistivity of Yttrium Doped ZnO Thin Films Grown on Quartz Glass by Sol–Gel Method. *Phys. B Condens. Matter* **2016**, *500*, 179–185.

(84) Prasad, U.; Prakash, J.; Kannan, A. M. Effects of Yttrium, Ytterbium with Tungsten Co-Doping on the Light Absorption and Charge Transport Properties of Bismuth Vanadate Photoanodes to Achieve Superior Photoelectrochemical Water Splitting. *Sustain. Energy Fuels* **2020**, *4*, 1496–1506.

(85) Prasad, U.; Prakash, J.; Shi, X.; Sharma, S. K.; Peng, X.; Kannan, A. M. Role of Alkali Metal in $BiVO_4$ Crystal Structure for Enhancing Charge Separation and Diffusion Length for Photoelectrochemical Water Splitting. *ACS Appl. Mater. Interfaces* **2020**, 12, 52808–55281.

(86) Young, J. L.; Steiner, M. A.; Döscher, H.; France, R. M.; Turner, J. A.; Deutsch, T. G. Direct Solar-to-Hydrogen Conversion via Inverted Metamorphic Multi-Junction Semiconductor Architectures. *Nat. Energy* **2017**, *2*, 1–8.

(87) Chen, Z.; Dinh, H. N.; Miller, E. *Photoelectrochemical Water Splitting*; 2013.

(88) Prakash, J.; Prasad, U.; Shi, X.; Peng, X.; Azeredo, B.; Kannan, A. M. Photoelectrochemical Water Splitting Using Lithium Doped Bismuth Vanadate Photoanode with Near-Complete Bulk Charge Separation. *J. Power Sources* **2020**, *448*, 227418

(89) Eichhorn, J.; Kastl, C.; Cooper, J. K.; Ziegler, D.; Schwartzberg, A. M.; Sharp, I. D.; Toma, F. M. Nanoscale Imaging of Charge Carrier Transport in Water Splitting Photoanodes. *Nat. Commun.* **2018**, *9*, 4–11.

(90) Dey, K. K.; Gahlawat, S.; Ingole, P. P. BiVO4 Optimized to Nano-Worm Morphology for Enhanced Activity towards Photoelectrochemical Water Splitting. *J. Mater. Chem. A* **2019**, *7*, 21207–21221.

(91) Kim, T. W.; Ping, Y.; Galli, G. A.; Choi, K. S. Simultaneous Enhancements in Photon Absorption and Charge Transport of Bismuth Vanadate Photoanodes for Solar Water Splitting. *Nat. Commun.* **2015**, *6*, 1–10.

(92) Lamers, M.; Li, W.; Favaro, M.; Starr, D. E.; Friedrich, D.; Lardhi, S.; Cavallo, L.; Harb, M.; Van De Krol, R.; Wong, L. H.; et al. Enhanced Carrier Transport and Bandgap Reduction in Sulfur-Modified BiVO 4 Photoanodes. *Chem. Mater.* **2018**, *30*, 8630–8638.

(93) Miyasato, R.; Fujiwara, M.; Uragami, C.; Sato, H.; Yano, T.; Hashimoto, H. Operando Time-Resolved Diffuse Reflection Spectroscopy: The Origins of Photocatalytic Water-Oxidation Activity of Bismuth Vanadate. *J. Photochem. Photobiol. A Chem.* **2020**, *395*, 20–23.

(94) Ma, Y.; Pendlebury, S. R.; Reynal, A.; Le Formal, F.; Durrant, J. R. Dynamics of Photogenerated Holes in Undoped BiVO4 Photoanodes for Solar Water Oxidation. *Chem. Sci.* **2014**, *5*, 2964–2973.

(95) Butler, K. T.; Dringoli, B. J.; Zhou, L.; Rao, P. M.; Walsh, A.; Titova, L. V. Ultrafast Carrier Dynamics in BiVO4 Thin Film Photoanode Material: Interplay between Free Carriers, Trapped Carriers and Low-Frequency Lattice Vibrations. *J. Mater. Chem. A* **2016**, *4*, 18516–18523.

(96) Hu, J.; Zhao, X.; Chen, W.; Su, H.; Chen, Z. Theoretical Insight into the Mechanism of Photoelectrochemical Oxygen Evolution Reaction on BiVO4 Anode with Oxygen Vacancy. *J. Phys. Chem. C* **2017**, *121*, 18702–18709.

(97) Prakash, J.; Prasad, U.; Shi, X.; Peng, X.; Azeredo, B.; Kannan, A. M. Photoelectrochemical Water Splitting Using Lithium Doped Bismuth Vanadate Photoanode with Near-Complete Bulk Charge Separation. *J. Power Sources* **2020**, *448*, 227418

(98) Gao, L.; Li, F.; Hu, H.; Long, X.; Xu, N.; Hu, Y.; Wei, S.; Wang, C.; Ma, J.; Jin, J. Dual Modification of a BiVO4 Photoanode for Enhanced Photoelectrochemical Performance. *ChemSusChem* **2018**, *11*, 2502–2509.

(99) Bhat, S. S. M.; Suh, J. M.; Choi, S.; Hong, S. P.; Lee, S. A.; Kim, C.; Moon, C. W.; Lee, M. G.; Jang, H. W. Substantially Enhanced Front Illumination Photocurrent in Porous SnO2 Nanorods/Networked BiVO4 Heterojunction Photoanodes. *J. Mater. Chem. A* **2018**, *6*, 14633–14643.

(100) Prakash, J.; Prasad, U.; Alexander, R.; Bahadur, J.; Dasgupta, K.; Kannan, A. N. M. Photoelectrochemical Solar Water Splitting: The Role of the Carbon Nanomaterials in Bismuth Vanadate Composite Photoanodes toward Efficient Charge Separation and Transport. *Langmuir* **2019**, *35*, 14492–14504.

(101) Li, Y.; Liu, Z.; Li, J.; Ruan, M.; Guo, Z. An Effective Strategy of Constructing a Multi-Junction Structure by Integrating a Heterojunction and a Homojunction to Promote the Charge Separation and Transfer Efficiency of WO3. *J. Mater. Chem. A* **2020**, *8*, 6256–6267.

(102) Chen, D.; Liu, Z.; Guo, Z.; Ruan, M.; Yan, W. 3D Branched Ca-Fe2O3/Fe2O3 Decorated with Pt and Co-Pi: Improved Charge-Separation Dynamics and Photoelectrochemical Performance. *ChemSusChem* **2019**, *12*, 3286–3295.

(103) Gao, L.; Long, X.; Wei, S.; Wang, C.; Wang, T.; Li, F.; Hu, Y.; Ma, J.; Jin, J. Facile Growth of AgVO3 Nanoparticles on Mo-Doped BiVO4 Film for Enhanced Photoelectrochemical Water Oxidation. *Chem. Eng. J.* **2019**, *378*.

(104) Prasad, U.; Prakash, J.; Gupta, S. K.; Zuniga, J.; Mao, Y.; Azeredo, B.; Kannan, A. N. M. Enhanced Photoelectrochemical Water Splitting with Er- and W-Codoped Bismuth Vanadate with WO3 Heterojunction-Based Two-Dimensional Photoelectrode. *ACS Appl. Mater. Interfaces* **2019**, *11*, 19029–19039.

(105) Zhong, X.; He, H.; Yang, M.; Ke, G.; Zhao, Z.; Dong, F.; Wang, B.; Chen, Y.; Shi, X.; Zhou, Y. In3+-Doped BiVO4 Photoanodes with Passivated Surface States for Photoelectrochemical Water Oxidation. *J. Mater. Chem. A* **2018**, *6*, 10456–10465.

(106) Wang, M.; Fu, W.; Du, L.; Wei, Y.; Rao, P.; Wei, L.; Zhao, X.; Wang, Y.; Sun, S. Surface Engineering by Doping Manganese into Cobalt Phosphide towards Highly Efficient Bifunctional HER and OER Electrocatalysis. *Appl. Surf. Sci.* **2020**, *515*, 146059.

(107) Richter, C.; Menon, L. Impact of Adsorbed Alkali Ions on Photoelectrochemical Hydrogen Production by Titania Nanotubes. *Energy Environ. Sci.* **2010**, *3*, 427–433.

(108) Grewe, T.; Tuÿsüz, H. Alkali Metals Incorporated Ordered Mesoporous Tantalum Oxide with Enhanced Photocatalytic Activity for Water Splitting. *J. Mater. Chem. A* **2016**, *4*, 3007–3017.

(109) Lamers, M.; Li, W.; Favaro, M.; Starr, D. E.; Friedrich, D.; Lardhi, S.; Cavallo, L.; Harb, M.; Van De Krol, R.; Wong, L. H.; et al. Enhanced Carrier Transport and Bandgap Reduction in Sulfur-Modified BiVO4 Photoanodes. *Chem. Mater.* **2018**, *30*, 8630–8638.

(110) Jang, J. W.; Friedrich, D.; Müller, S.; Lamers, M.; Hempel, H.; Lardhi, S.; Cao, Z.; Harb, M.; Cavallo, L.; Heller, R.; et al. Enhancing Charge Carrier Lifetime in Metal Oxide Photoelectrodes through Mild Hydrogen Treatment. *Adv. Energy Mater.* **2017**, *7*, 1–11.

(111) Irani, R.; Ahmet, I. Y.; Jang, J. W.; Berglund, S. P.; Plate, P.; Höhn, C.; Böttger, R.; Schmitt, S. W.; Dubourdieu, C.; Lardhi, S.; et al. Nature of Nitrogen Incorporation in BiVO4 Photoanodes through Chemical and Physical Methods. *Sol. RRL* **2020**, *4*.

(112) Yao, T.; An, X.; Han, H.; Chen, J. Q.; Li, C. Photoelectrocatalytic Materials for Solar Water Splitting. *Adv. Energy Mater.* **2018**, *8*, 1–36.

(113) Vo, T. G.; Tai, Y.; Chiang, C. Y. Novel Hierarchical Ferric Phosphate/Bismuth Vanadate Nanocactus for Highly Efficient and Stable Solar Water Splitting. *Appl. Catal. B Environ.* **2019**, *243*, 657–666.

(114) Zhao, Z.; Li, Z.; Zou, Z. Electronic Structure and Optical Properties of Monoclinic Clinobisvanite BiVO4. *Phys. Chem. Chem. Phys.* **2011**, *13*, 4746–4753.

(115) Yuan, Y.; Huang, Y.; Ma, F.; Zhang, Z.; Wei, X. Effects of Oxygen Vacancy on the Mechanical, Electronic and Optical Properties of Monoclinic BiVO4. *J. Mater. Sci.* **2017**, *52*, 8546–8555.

(116) Cooper, J. K.; Gul, S.; Toma, F. M.; Chen, L.; Glans, P. A.; Guo, J.; Ager, J. W.; Yano, J.; Sharp, I. D. Electronic Structure of Monoclinic BiVO4. *Chem. Mater.* **2014**, *26*, 5365–5373.

(117) Wiktor, J.; Reshetnyak, I.; Ambrosio, F.; Pasquarello, A. Comprehensive Modeling of the Band Gap and Absorption Spectrum of BiVO4. *Phys. Rev. Mater.* **2017**, *1*, 1–6.

(118) Kim, T. W.; Ping, Y.; Galli, G. A.; Choi, K. S. Simultaneous Enhancements in Photon Absorption and Charge Transport of Bismuth Vanadate Photoanodes for

Solar Water Splitting. *Nat. Commun.* **2015**, *6*, 1–10.

(119) Schultz, P. .; Lynn, K. G. Interaction of Positron Beams. *Rev. Mod. Phys.* **1988**, *60*, 701–779.

(120) To, C. K.; Yang, B.; Beling, C. D.; Fung, S.; Ling, C. C.; Gong, M. Positron Annihilation Study of Defects in Electron-Irradiated Single Crystal Zinc Oxide. *J. Phys. Conf. Ser.* **2011**, *262*, 8–12.

(121) Pattengale, B.; Ludwig, J.; Huang, J. Atomic Insight into the W-Doping Effect on Carrier Dynamics and Photoelectrochemical Properties of BiVO4photoanodes. *J. Phys. Chem. C* **2016**, *120*, 1421–1427.

(122) Cho, S. K.; Park, H. S.; Lee, H. C.; Nam, K. M.; Bard, A. J. Metal Doping of BiVO4 by Composite Electrodeposition with Improved Photoelectrochemical Water Oxidation. *J. Phys. Chem. C* **2013**, *117*, 23048–23056.

(123) Berglund, S. P.; Rettie, A. J. E.; Hoang, S.; Mullins, C. B. Incorporation of Mo and W into Nanostructured BiVO4 Films for Efficient Photoelectrochemical Water Oxidation. *Phys. Chem. Chem. Phys.* **2012**, *14*, 7065.

(124) Ye, H.; Park, H. S.; Bard, A. J. Screening of Electrocatalysts for Photoelectrochemical Water Oxidation on W-Doped BiVO4 Photocatalysts by Scanning Electrochemical Microscopy. *J. Phys. Chem. C* **2011**, *115*, 12464–12470.

(125) Quiñonero, J.; Lana-Villarreal, T.; Gómez, R. Improving the Photoactivity of Bismuth Vanadate Thin Film Photoanodes through Doping and Surface Modification Strategies. *Appl. Catal. B Environ.* **2016**, *194*, 141–149.

(126) Abdi, F. F.; Savenije, T. J.; May, M. M.; Dam, B.; Van De Krol, R. The Origin of Slow Carrier Transport in BiVO4 Thin Film Photoanodes: A Time-Resolved Microwave Conductivity Study. *J. Phys. Chem. Lett.* **2013**, *4*, 2752–2757.

(127) Jo, W. J.; Jang, J.-W.; Kong, K.; Kang, H. J.; Kim, J. Y.; Jun, H.; Parmar, K. P. S.; Lee, J. S. Phosphate Doping into Monoclinic BiVO4 for Enhanced Photoelectrochemical Water Oxidation Activity. *Angew. Chemie Int. Ed.* **2012**, *51*, 3147–3151.

(128) Gratzel Book.Pdf.Crdownload.

(129) Huang, M.; Bian, J.; Xiong, W.; Huang, C.; Zhang, R. Low-Dimensional Mo:BiVO4 Photoanodes for Enhanced Photoelectrochemical Activity. *J. Mater. Chem. A* **2018**, *6*, 3602–3609.

(130) Chakthranont, P.; Hellstern, T. R.; McEnaney, J. M.; Jaramillo, T. F. Design and Fabrication of a Precious Metal-Free Tandem Core–Shell P+n Si/W-Doped BiVO4 Photoanode for Unassisted Water Splitting. *Adv. Energy Mater.* **2017**, *7*, 1–8.

(131) Jo, W. J.; Kang, H. J.; Kong, K.-J.; Lee, Y. S.; Park, H.; Lee, Y.; Buonassisi, T.; Gleason, K. K.; Lee, J. S. Phase Transition-Induced Band Edge Engineering of BiVO 4 to Split Pure Water under Visible Light . *Proc. Natl. Acad. Sci.* **2015**, *112*,

13774–13778.

(132) Zhao, X.; Hu, J.; Wu, B.; Banerjee, A.; Chakraborty, S.; Feng, J.; Zhao, Z.; Chen, S.; Ahuja, R.; Sum, T. C.; et al. Simultaneous Enhancement in Charge Separation and Onset Potential for Water Oxidation in a BiVO 4 Photoanode by W-Ti Codoping. *J. Mater. Chem. A* **2018**, *6*, 16965–16974.

(133) Jiao, Z.; Zheng, J.; Feng, C.; Wang, Z.; Wang, X.; Lu, G.; Bi, Y. Fe/W Co-Doped BiVO 4 Photoanodes with a Metal–Organic Framework Cocatalyst for Improved Photoelectrochemical Stability and Activity. *ChemSusChem* **2016**, *9*, 2824–2831.

(134) Wang, M.; Han, J.; Lv, C.; Zhang, Y.; You, M.; Liu, T.; Li, S.; Zhu, T. Ag, B, and Eu Tri-Modified BiVO 4 Photocatalysts with Enhanced Photocatalytic Performance under Visible-Light Irradiation. *J. Alloys Compd.* **2018**, *753*, 465–474.

(135) Xue, S.; He, H.; Wu, Z.; Yu, C.; Fan, Q.; Peng, G.; Yang, K. An Interesting Eu,F-Codoped BiVO4microsphere with Enhanced Photocatalytic Performance. *J. Alloys Compd.* **2017**, *694*, 989–997.

(136) Obregón, S.; Colón, G. Excellent Photocatalytic Activity of Yb3+, Er3+co-Doped BiVO4photocatalyst. *Appl. Catal. B Environ.* **2014**, *152–153*, 328–334.

(137) Regmi, C.; Kshetri, Y. K.; Ray, S. K.; Pandey, R. P.; Lee, S. W. Utilization of Visible to NIR Light Energy by Yb+3, Er+3 and Tm+3 Doped BiVO4 for the Photocatalytic Degradation of Methylene Blue. *Appl. Surf. Sci.* **2017**, *392*, 61–70.

(138) Prasad, U.; Prakash, J.; Azeredo, B.; Kannan, A. Stoichiometric and Non-Stoichiometric Tungsten Doping Effect in Bismuth Vanadate Based Photoactive Material for Photoelectrochemical Water Splitting. *Electrochim. Acta* **2019**, *299*, 262–272.

(139) Trasa, S.; Petrii, A.; Niki, K. International Union of Pure and Applied Chemistry Real Surface Area Measurements in Electrochemistry. *J. N. Agar (UK J. Koryta (Czechoslovakia Plieth (FRG* **1992**, *321*, 353–376.

(140) Nasir, S. N. F. M.; Ullah, H.; Ebadi, M.; Tahir, A. A.; Sagu, J. S.; Teridi, M. A. M. New Insights into Se/BiVO 4 Heterostructure for Photoelectrochemical Water Splitting: A Combined Experimental and DFT Study. *J. Phys. Chem. C* **2017**, *121*.

(141) Lee, M. G.; Kim, D. H.; Sohn, W.; Moon, C. W.; Park, H.; Lee, S.; Jang, H. W. Conformally Coated BiVO4 Nanodots on Porosity-Controlled WO3 Nanorods as Highly Efficient Type II Heterojunction Photoanodes for Water Oxidation. *Nano Energy* **2016**, *28*, 250–260.

(142) Li, L.; Yang, X.; Lei, Y.; Yu, H.; Yang, Z.; Zheng, Z.; Wang, D. Ultrathin Fe-NiO Nanosheets as Catalytic Charge Reservoirs for a Planar Mo-Doped BiVO 4 Photoanode. *Chem. Sci.* **2018**, *9*, 8860–8870.

(143) Li, L.; Yang, X.; Lei, Y.; Yu, H.; Yang, Z.; Zheng, Z.; Wang, D. Ultrathin Fe-NiO Nanosheets as Catalytic Charge Reservoirs for a Planar Mo-Doped BiVO4

Photoanode. *Chem. Sci.* **2018**, *9*, 8860–8870.

(144) Dias, P.; Andrade, L.; Mendes, A. Hematite-Based Photoelectrode for Solar Water Splitting with Very High Photovoltage. *Nano Energy* **2017**, *38*, 218–231.

(145) Zhang, Q.; Xiao, Y.; Li, Y.; Zhao, K.; Deng, H.; Lou, Y.; Chen, J.; Yu, H.; Cheng, L. Efficient Photocatalytic Overall Water Splitting by Synergistically Enhancing Bulk Charge Separation and Surface Reaction Kinetics in Co3O4–Decorated ZnO@ZnS Core-Shell Structures. *Chem. Eng. J.* **2020**, *393*, 124681.

(146) Lutterman, D. A.; Surendranath, Y.; Nocera, D. G. A Self-Healing Oxygen-Evolving Catalyst. **2009**, 3838–3839.

(147) Surendranath, Y.; Lutterman, D. A.; Liu, Y.; Nocera, D. G. Nucleation, Growth, and Repair of a Cobalt-Based Oxygen Evolving Catalyst. *J. Am. Chem. Soc.* **2012**, *134*, 6326–6336.

(148) Grigioni, I.; Ganzer, L.; V. A. Camargo, F.; Bozzini, B.; Cerullo, G.; Selli, E. In Operando Photoelectrochemical Femtosecond Transient Absorption Spectroscopy of WO3/BiVO4 Heterojunctions. *ACS Energy Lett.* **2019**, *4*, 2213–2219.

(149) Selim, S.; Francàs, L.; García-Tecedor, M.; Corby, S.; Blackman, C.; Gimenez, S.; Durrant, J. R.; Kafizas, A. WO3/BiVO4: Impact of Charge Separation at the Timescale of Water Oxidation. *Chem. Sci.* **2019**, *10*, 2643–2652.

(150) Grigioni, I.; Abdellah, M.; Corti, A.; Dozzi, M. V.; Hammarström, L.; Selli, E. Photoinduced Charge-Transfer Dynamics in WO3/BiVO4 Photoanodes Probed through Midinfrared Transient Absorption Spectroscopy. *J. Am. Chem. Soc.* **2018**, 8–11.

(151) Lee, J. M.; Baek, J. H.; Gill, T. M.; Shi, X.; Lee, S.; Cho, I. S.; Jung, H. S.; Zheng, X. A Zn:BiVO4/Mo:BiVO4 Homojunction as an Efficient Photoanode for Photoelectrochemical Water Splitting. *J. Mater. Chem. A* **2019**, *7*, 9019–9024.

(152) Gao, R. T.; He, D.; Wu, L.; Hu, K.; Liu, X.; Su, Y.; Wang, L. Towards Long-Term Photostability of Nickel Hydroxide/BiVO4 Photoanodes for Oxygen Evolution Catalysts via In Situ Catalyst Tuning. *Angew. Chemie - Int. Ed.* **2020**, *59*, 6213–6218.

(153) Prakash, J.; Prasad, U.; Shi, X.; Peng, X.; Azeredo, B.; Kannan, A. M. Photoelectrochemical Water Splitting Using Lithium Doped Bismuth Vanadate Photoanode with Near-Complete Bulk Charge Separation. *J. Power Sources* **2020**, *448*.

(154) Grigioni, I.; Stamplecoskie, K. G.; Selli, E.; Kamat, P. V. Dynamics of Photogenerated Charge Carriers in WO3/BiVO4 Heterojunction Photoanodes. *J. Phys. Chem. C* **2015**, *119*, 20792–20800.

(155) Prasad, U.; Young, J. L.; Johnson, J. C.; McGott, D. L.; Gu, H.; Garfunkel, E.; Kannan, A. M. Enhancing Interfacial Charge Transfer in a WO3/BiVO4photoanode

Heterojunction through Gallium and Tungsten Co-Doping and a Sulfur Modified Bi2O3interfacial Layer. *J. Mater. Chem. A* **2021**, *9*, 16137–16149.

(156) Su, J.; Guo, L.; Bao, N.; Grimes, C. A. Nanostructured WO3/BiVO4 Heterojunction Films for Efficient Photoelectrochemical Water Splitting. *Nano Lett.* **2011**, *11*, 1928–1933.

(157) Choi, J.; Sudhagar, P.; Kim, J. H.; Kwon, J.; Kim, J.; Terashima, C.; Fujishima, A.; Song, T.; Paik, U. WO3/W:BiVO4/BiVO4 Graded Photoabsorber Electrode for Enhanced Photoelectrocatalytic Solar Light Driven Water Oxidation. *Phys. Chem. Chem. Phys.* **2017**, *19*, 4648–4655.

(158) Zhang, Z.; Chen, B.; Baek, M.; Yong, K. Multichannel Charge Transport of a BiVO4/(RGO/WO3)/W18O49 Three-Storey Anode for Greatly Enhanced Photoelectrochemical Efficiency. *ACS Appl. Mater. Interfaces* **2018**, *10*, 6218–6227.

(159) Wang, R.; Xie, T.; Zhang, T.; Pu, T.; Bu, Y.; Ao, J. P. Fabrication of FTO-BiVO4-W-WO3 Photoanode for Improving Photoelectrochemical Performance: Based on the Z-Scheme Electron Transfer Mechanism. *J. Mater. Chem. A* **2018**, *6*, 12956–12961.

(160) Baek, J. H.; Kim, B. J.; Han, G. S.; Hwang, S. W.; Kim, D. R.; Cho, I. S.; Jung, H. S. BiVO4/WO3/SnO2 Double-Heterojunction Photoanode with Enhanced Charge Separation and Visible-Transparency for Bias-Free Solar Water-Splitting with a Perovskite Solar Cell. *ACS Appl. Mater. Interfaces* **2017**, *9*, 1479–1487.

(161) Xie, J.; Guo, C.; Li, C. M. Ga Doping to Significantly Improve the Performance of All-Electrochemically Fabricated Cu2O-ZnO Nanowire Solar Cells. *Phys. Chem. Chem. Phys.* **2013**, *15*, 15905–15911.

(162) Pal, K.; Parmar, S.; Kang, J.; Bist, A.; Dua, P.; Jang, S. Photocatalytic and Photoelectrochemical Water Oxidation over Metal-Doped Monoclinic BiVO 4 Photoanodes. **2012**, *784*, 1926–1934.

(163) Pihosh, Y.; Turkevych, I.; Mawatari, K.; Asai, T.; Hisatomi, T.; Uemura, J.; Tosa, M.; Shimamura, K.; Kubota, J.; Domen, K.; et al. Nanostructured WO 3 /BiVO 4 Photoanodes for Efficient Photoelectrochemical Water Splitting . *Small* **2014**, *10*, 3692–3699.

(164) Shi, X.; Choi, I. Y.; Zhang, K.; Kwon, J.; Kim, D. Y.; Lee, J. K.; Oh, S. H.; Kim, J. K.; Park, J. H. Efficient Photoelectrochemical Hydrogen Production from Bismuth Vanadate-Decorated Tungsten Trioxide Helix Nanostructures. *Nat. Commun.* **2014**, *5*, 1–8.

(165) Luo, X.; Zhu, G.; Peng, J.; Wei, X.; Hojamberdiev, M.; Jin, L.; Liu, P. Enhanced Photocatalytic Activity of Gd-Doped Porous β-Bi 2 O 3 Photocatalysts under Visible Light Irradiation. *Appl. Surf. Sci.* **2015**, *351*, 260–269.

(166) Wang, R.; Li, D.; Wang, H.; Liu, C.; Xu, L. Preparation, Characterization, and

Performance Analysis of S-Doped Bi2MoO6 Nanosheets. *Nanomaterials* **2019**, *9*.

(167) Han, F.; Li, H.; Fu, L.; Yang, J.; Liu, Z. Synthesis of S-Doped WO3 Nanowires with Enhanced Photocatalytic Performance towards Dye Degradation. *Chem. Phys. Lett.* **2016**, *651*, 183–187.

(168) Klahr, B.; Gimenez, S.; Fabregat-Santiago, F.; Hamann, T.; Bisquert, J. Water Oxidation at Hematite Photoelectrodes: The Role of Surface States. *J. Am. Chem. Soc.* **2012**, *134*, 4294–4302.

(169) Shi, X.; Herraiz-Cardona, I.; Bertoluzzi, L.; Lopez-Varo, P.; Bisquert, J.; Park, J. H.; Gimenez, S. Understanding the Synergistic Effect of WO3-BiVO4 Heterostructures by Impedance Spectroscopy. *Phys. Chem. Chem. Phys.* **2016**, *18*, 9255–9261.

(170) Kim, D.; Zhang, Z.; Yong, K. Synergistic Doping Effects of a ZnO:N/BiVO4:Mo Bunched Nanorod Array Photoanode for Enhancing Charge Transfer and Carrier Density in Photoelectrochemical Systems. *Nanoscale* **2018**, *10*, 20256–20265.

(171) Ravensbergen, J.; Abdi, F. F.; van Santen, J. H.; Frese, R. N.; Dam, B.; van de Krol, R.; Kennis, J. T. M. Unraveling the Carrier Dynamics of BiVO4: A Femtosecond to Microsecond Transient Absorption Study. *J. Phys. Chem. C* **2014**, *118*, 27793–27800.

(172) Resasco, J.; Zhang, H.; Kornienko, N.; Becknell, N.; Lee, H.; Guo, J.; Briseno, A. L.; Yang, P. TiO2/BiVO4 Nanowire Heterostructure Photoanodes Based on Type II Band Alignment. *ACS Cent. Sci.* **2016**, *2*, 80–88.

(173) Saito, R.; Miseki, Y.; Sayama, K. ChemComm Highly Efficient Photoelectrochemical Water Splitting Using a Thin Film. **2012**, 3833–3835.

(174) Kim, M. W.; Joshi, B.; Samuel, E.; Kim, K.; Kim, Y. Il; Kim, T. G.; Swihart, M. T.; Yoon, S. S. Highly Nanotextured β-Bi2O3 Pillars by Electrostatic Spray Deposition as Photoanodes for Solar Water Splitting. *Journal of Alloys and Compounds*. 2018, pp 881–889.

(175) Lee, S.; Song, J.; Jo, Y.-R.; Choi, K. S.; Lee, J.; Seo, S.; Kim, T. L.; Jang, H. W.; Jeon, C.; Kim, B.-J.; et al. In Situ Growth of Nanostructured BiVO4–Bi2O3 Mixed-Phase via Nonequilibrium Deposition Involving Metal Exsolution for Enhanced Photoelectrochemical Water Splitting. *ACS Appl. Mater. Interfaces* **2019**, *11*, 44069–44076.

(176) Lee, D. K.; Choi, K.-S. Enhancing Long-Term Photostability of BiVO4 Photoanodes for Solar Water Splitting by Tuning Electrolyte Composition. *Nat. Energy* **2017**, *3*, 53–60.

(177) Kanth, N.; Xu, W.; Prasad, U.; Ravichandran, D.; Kannan, A. M.; Song, K. Pmma-Tio2 Fibers for the Photocatalytic Degradation of Water Pollutants. *Nanomaterials* **2020**, *10*, 1–8.

(178) Prasad, U.; Kannan, A. N. M. Extended Light Absorption Management by Forming Dual Heterojunction in Monoclinic BiVO4 for Enhanced Photoelectrochemical Water Oxidation. In *ACS Spring 2020 National Meeting & Expo*; 2020.

(179) Prasad, U. Sustainable Energy & Fuels Doping on the Light Absorption and Charge Transport Properties of Bismuth Vanadate Photoanodes to Achieve Superior Photoelectrochemical Water Splitting †. **2020**.

(180) Prasad, U. BiVO $_4$ -Based Photoanodes for Photoelectrochemical Water Splitting; *ACS Symp. Ser.* **2020**, *1364*, 137–167.

(181) Prasad, U. BiVO $_4$ -Based Photoanodes for Photoelectrochemical Water Splitting; *ACS Symp. Ser.* **2020**, *1364*, 137–167.

(182) Jeong, H. W.; Chae, W. S.; Song, B.; Cho, C. H.; Baek, S. H.; Park, Y.; Park, H. Optical Resonance and Charge Transfer Behavior of Patterned WO3 Microdisc Arrays. *Energy Environ. Sci.* **2016**, *9*, 3143–3150.

(183) Ahmad, H.; Kamarudin, S. K.; Minggu, L. J.; Kassim, M. Hydrogen from Photo-Catalytic Water Splitting Process: A Review. *Renew. Sustain. Energy Rev.* **2015**, *43*, 599–610.